An Integrated Fiber-Based Cavity in a Paul Trap

Dissertation

zur Erlangung des akademischen Grades
"Doktor der Naturwissenschaften"
am Fachbereich Physik, Mathematik und Informatik
der Johannes Gutenberg-Universität
in Mainz

vorgelegt von
Andreas Daniel Pfister
geboren in Zweibrücken

JOHANNES GUTENBERG UNIVERSITÄT MAINZ

August 2019

Datum der Disputation: 02.12.2019

In memory of Sally Jean Andrews-Pfister

Zusammenfassung

In dieser Promotionsarbeit wird eine segmentierte, mikrostrukturierte, lineare Paulfalle mit einem eingebauten faserbasierten Resonator entwickelt. Ziel war es, die Verschränkungsverteilung über große Entfernungen zu untersuchen. Zu Beginn wurde ein faserbasierter Resonator entwickelt, der bei einem Spiegelabstand $\leq 250\,\mu\mathrm{m}$ noch immer eine hohe Finesse $F = 16000$ besitzt.

Diese Falle stellt ein an die Faserintegration angepasstes Design dar, welches von einer bestehenden mikrostrukturierten, segmentierten Paulfalle abgeleitet wurde. Der Resonator wird nun durch einem kompakten, monolithischen Halter in die Falle integriert. Durch die Durchkontaktierungen (VIAs) kann diese Falle Wechselspannungen mit einer Schwingungsbreite $\leq 800\,\mathrm{V}$ ausgesetzt werden. Dieses Resonator-Falle-System wurde erfolgreich in Betrieb genommen und charakterisiert. Die Wechselwirkung einzelner Ionen mit dem Resonatorfeld war jedoch nicht nachweisbar, vermutlich aufgrund von Aufladungen der Fasern und Spiegelflächen, die das axiale Fallenfeld stark verändern können. Die dafür benötigte Ladung wurde berechnet.

Zusätzlich wurde der Aufbau auf seine Eignung zur Implementation einer Auswahl an Quantenverschlüsselungsprotokollen untersucht. Mit Hilfe von Annahmen, die experimentell realistisch sind, konnten Raten von mehr als 100 Verschränkungen pro Sekunde berechnet werden, bei einer Zustandstreue (Fidelity) für nichtlokale Bellzustände ≤ 0.95. Aus der Diskussion begrenzender Parameter kann man schließen, dass Verschränkungsraten von $750\,\mathrm{s}^{-1}$ bei diesen Zustandstreuen mit aktueller Technologie erreichbar sind. Diese Raten sind hoch genug, um den Kohärenzverlust von Qubits in Ionenfallen auszugleichen, und ermöglichen die Erzeugung von nichtlokalen Verschränkungen mit hoher Zustandstreue.

Diese Arbeit ist somit ein wichtiger Schritt in Richtung Realisierung von langreichweitiger Verschränkungsverteilung mit Hilfe von Ionenfallen.

Abstract

A segmented micro-structured linear Paul trap with an integrated fiber-based cavity is constructed, with the aim of investigating long-distance entanglement distribution. The fiber-based cavity was fabricated at the beginning of this thesis, in order to build a high-finesse cavity of length $\leq 250\,\mu\mathrm{m}$, and with a finesse of up to $F = 16000$. The cavity is supported on a compact, monolithic holder design.

The trap design has been adapted from a segmented ion trap to allow resonator integration. The chips feature vertical interconnects (VIAs) that allow for application of voltages $\leq 800\,\mathrm{V}$ peak-peak. The resonator-trap-system was successfully operated and characterized. However, we were not able to show the ion interacting with the cavity field, and conjecture stray charges which strongly modify the electric axial trapping potential. The strength of the charges required to create this effect is quantified.

Furthermore, the setup is investigated regarding the feasibility of implementing a selection of quantum key distribution protocols. Experimentally achievable parameter assumptions lead to calculated rates of more than than 100 entanglements per second for non-local Bell state fidelities ≤ 0.95 with the existing platform. Limiting parameters are identified, and it is concluded that entanglement generation rates of $750\,\mathrm{s}^{-1}$ at fidelities of 0.95 are within reach with current technology. These rates exceed the stationary qubit decay rate, and allow the creation of high-fidelity, non-local entanglement.

This work is thus an important step towards realizing long-range entanglement distribution based on ion traps.

Contents

1 Introduction to Long Distance Entanglement Distribution

Quantum entanglement is the quantum mechanical phenomenon of the states of particles being correlated more strongly than classical physics allows, which leads to the impossibility of describing each subgroup's state without taking the other particles into account. More formally, the wavefunction of all the particles cannot be rewritten as a the product of single particle wavefunctions. For a system

$$|\Psi\rangle_S \left(|\Psi_0\rangle, |\Psi_1\rangle, ... |\Psi_n\rangle \right) \tag{1.1}$$

made up of n subsystems, it is entangled if it is impossible to describe the system as a *separable state*, or product state of the constituent wave functions, i.e., a state

$$|\Psi\rangle_S = |\Psi_0\rangle \otimes |\Psi_1\rangle \otimes ... \otimes |\Psi_n\rangle \tag{1.2}$$

cannot be constructed for the system. The first description of an entangled system was the famous *Einstein-Podolsky-Rosen* paradox described in Einstein et al. [Ein35]. Physically interesting in its own right, entanglement is also an important resource in the field of quantum information technology, for quantum computing, quantum metrology [Gio06] and quantum cryptography.

1.1 Quantum Computing

Quantum computing (QC) uses qubits to render tractable certain problems that are difficult in classical computing [Nie00]. A distinct difficulty in realizing a useful universal quantum computer is the trouble of controlling multiple qubits - no matter the hardware platform, qubit numbers much larger than 20 in one experiment are beyond the reach of current technology. Exacting requirements for control can push this number down even further for truly universal QC. Long distance entanglement distribution is a possible solution for this problem of exponentially more difficult local control. Modular QC [Mon14; Huc14] replaces a monolithic experiment trying to control a multitude of qubits in a single trap, or on a single chip, with small computation units comprised of only a few qubits, because the small units can be controlled with comparable ease, but are large enough for certain basic operations. These modules are connected to each other in a quantum communications network, able to create distributed entanglement between each other. This allows the spread of quantum states between the modules, and the transfer of states from one module to another, allowing the QC to scale up in terms of total qubit size while staying universal.

1.2 Quantum Key Distribution

One of the most prominent, and most advanced, applications in quantum technology is quantum cryptography, or *quantum key distribution* (QKD). QKD is the exchange of public encryption keys with the help of quantum mechanics, in order to be able to exchange encrypted messages between parties at different locations (archetypically the sender *Alice* and the receiver *Bob*). The no-cloning theorem of quantum mechanics [Woo82] then enables secure communication protocols by ensuring that any quantum information (i.e., entanglement) shared between Alice and Bob cannot have been measured by an attacker *Eve*. The subject was first developed in the paper by Bennet and Brassard in 1984 [Ben84], which introduced the first scheme for QKD with the so-called BB84 protocol. In this paper, Alice encodes her qubits in two bases that aren't orthogonal to each other, e.g., linearly and circularly polarized photons. Quantum correlations and the collapse of the wavefunction during a measurement are used to inform the participants of attackers in the channel. Another protocol was suggested by Ekert [Eke91], where entangled pairs of particles are created, one sent to (or kept by) Alice, the other sent to Bob. This scheme relies on the random but perfectly correlated result of the measurement of an entangled pair of particles, as well as the destruction of said correlation, guaranteed by the no-cloning theorem, should an attacker be able to insert their own measurement into the sequence. It also highlights the idea at the foundations of this thesis: *Long range entanglement distribution*[1], where particle pairs are separated by a large distance but still entangled [Ben84]. Bennett then quickly expanded on these ideas [Ben92a] and proved their equivalence [Ben92b]. For distances less than 80 km, QKD is commercially available [2] [3] using standard telecom fiber networks, and recent experiments have been able to distribute cryptographic keys over 311 km [Yin16].

---

[1] QKD and long range entanglement distribution will be used interchangeably in this thesis, as all practical QKD protocols are based on long range entangled pairs and their creation in the face of errors

[2] ID Quantique SA, Chemin de la Marbrerie, 3 bis, 1227 Geneva, Switzerland

[3] MagiQ Technologies, Somerville, Massachusetts 02143, USA, https://www.magiqtech.com/

Direct QKD without intermediate steps suffers from two sources of errors that increase exponentially with the communication distance [Bri98]: Loss of transmitted photons, and depolarization of their state. The first error source will increase the number of tries required to successfully transmit an entangled photon exponentially with the transmission distance L. The second error source leads to an exponential reduction of the fidelity F of the transmitted state. Even in the presence of quantum error correction (QEC) schemes [Sho95; Ste96; Ter15], these barriers are too hard to overcome, as QEC generally has exacting requirements on the maximum error allowed, which often demands total state fidelities in the range of 10^{-4} or lower. One option for technically achievable QKD is to rely on free-space optical links instead of fiber-based solutions, which use the low losses in air for optical wavelengths. In that manner, successful links have been established and tested between two of the Canary Islands [Ma12], and between a base station and a satellite in low earth orbit [Val15]. Recently, such as an earth-to-satellite link has been used to distribute a cryptographic key between Xinglong and Nanshan, both in China, and Graz, in Austria, with a key rate of $\approx$ 1kHz between ground and low earth orbit [Lia18]. However, the final rate of key distribution was limited by satellite fly-over times, and the satellite had to function as a classical network node, and thus had to be trusted not to be compromised by Eve.

1.3 Quantum Repeaters

Another possibility of overcoming these hard boundaries was suggested in 1998: Briegel, Dür, Cirac and Zoller [Bri98] showed that partitioning the entire distance L into N nodes, separated by distances $L_0 = L/N$, capable of storing entangled particles, and of performing *entanglement purification* [Ben96; Deu96; Dür03; Dür07; Nic14] between each node, results instead in a polynomial overhead in time, and in a logarithmic overhead in resources. In that manner, such a chain of nodes extends the range of entanglement generation from exponential drop-off with a potentially finite, and short, maximum range to (in principle) arbitrary distances, limited now by the time the basic nodes can be kept in coherence with their distant cousins. This result opened up the way for proposals and experiments to realize such a *quantum repeater* for QKD. The quantum repeater's central tool is the distribution of long range entanglement between two distant endpoints. Proposals for experimental realization include those based on atomic and ionic systems, which utilize quantum optical techniques [Kuz03; Dua10; Rit12; Huc14], as well as those based on solid state quantum devices [Aha16] such as quantum dots [Pre08; Gsc15], and the ones based on color cen-

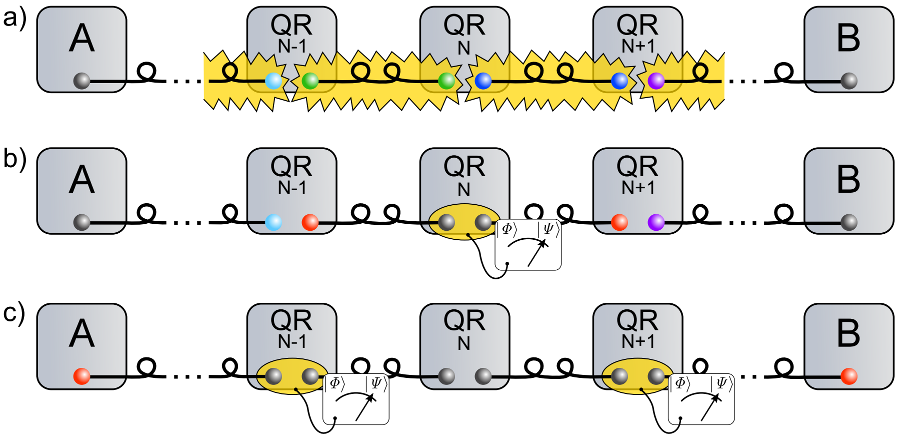

Figure 1.1: Scheme of long distance QKD using quantum repeaters (QR): a) Entanglement (indicated by colors) is generated between stationary qubits of adjacent repeater nodes via optical channels (black lines). b) A local Bell state measurement allows for an entanglement swapping procedure. c) Consecutive entanglement swapping operations ultimately leave the system with Alice (A) and Bob (B) having one entangled Bell pair. Finally, the Eckert protocol [Eke91] allows for a secret QKD between Alice and Bob.

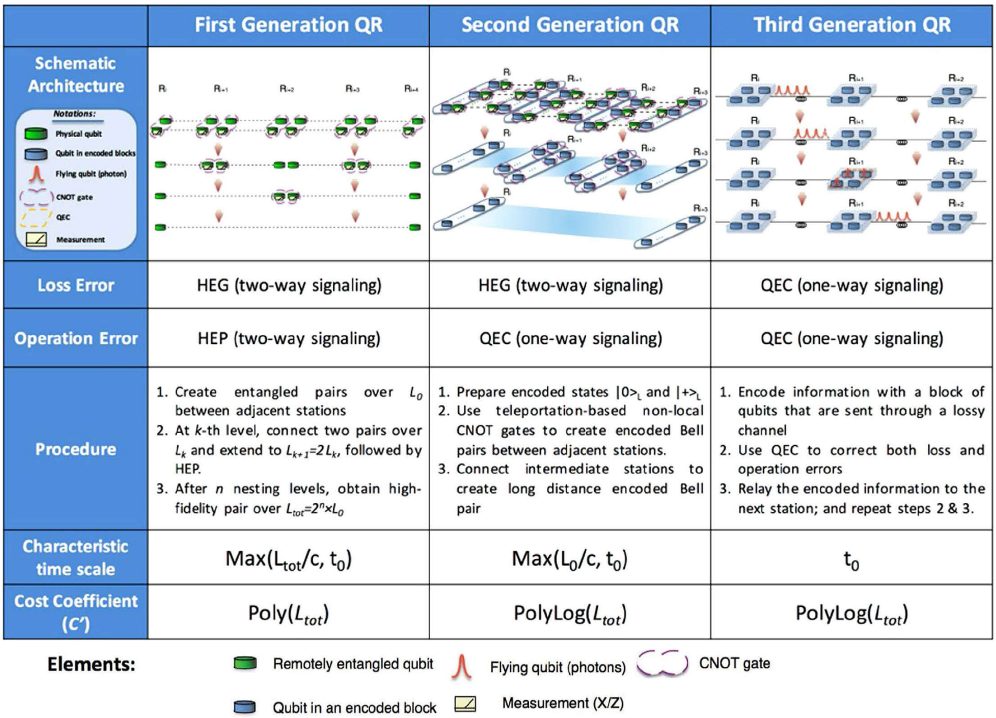

	First Generation QR	Second Generation QR	Third Generation QR
Schematic Architecture			
Loss Error	HEG (two-way signaling)	HEG (two-way signaling)	QEC (one-way signaling)
Operation Error	HEP (two-way signaling)	QEC (one-way signaling)	QEC (one-way signaling)
Procedure	1. Create entangled pairs over L_0 between adjacent stations 2. At k-th level, connect two pairs over L_k and extend to $L_{k+1}=2L_k$, followed by HEP. 3. After n nesting levels, obtain high-fidelity pair over $L_{tot}=2^n \times L_0$	1. Prepare encoded states $\|0>_L$ and $\|+>_L$ 2. Use teleportation-based non-local CNOT gates to create encoded Bell pairs between adjacent stations. 3. Connect intermediate stations to create long distance encoded Bell pair	1. Encode information with a block of qubits that are sent through a lossy channel 2. Use QEC to correct both loss and operation errors 3. Relay the encoded information to the next station; and repeat steps 2 & 3.
Characteristic time scale	$\mathrm{Max}(L_{tot}/c, t_0)$	$\mathrm{Max}(L_0/c, t_0)$	t_0
Cost Coefficient (C')	$\mathrm{Poly}(L_{tot})$	$\mathrm{PolyLog}(L_{tot})$	$\mathrm{PolyLog}(L_{tot})$

Figure 1.2: Division of different repeater architectures into generations, dependent on different methods to combat loss errors and operation errors. HEG and HEP stand for "Heralded Entanglement Generation" and "Heralded Entanglement Purification". L_{tot} is the entire distance of entanglement distribution, while L_0 is the distance between two QR nodes, and t_0 is the time taken for local quantum gates at each node. In addition, the time and number of qubit requirements ("Characteristic time scale" and "Cost Coefficient") for each QR generation is given. Picture taken from Muralidharan et al.[Mur16], used with permission.

ters in crystals, which include contenders like nitrogen-vacancy [Sip12; Ber12] or silicon-vacancy [Sip14] centers in diamonds. Other proposals are based on purely photonic systems [Rau01; Azu15]. However, up to date there has been no demonstration of a fully functional QR.

Quantum repeaters can be subdivided into three generations[Mur16], dependent on the extent of their use of either entanglement purification or quantum error correction. The defining characteristics are how the QR works to suppress the two kinds of errors inherent in each entanglement distribution system: *Loss error* describes the loss of a qubit, e.g., through photon loss in the fiber transmission, or through non-interaction of the photon with the memory qubit due to an imperfect interface. *Operation errors*, also called *gate errors* in other sources, are infidelities of the resulting entangled state in comparison to the target state, described by probabilities of quantum gates (including waiting and measurement) to create unwanted states. Quantum repeaters according to Briegel, Dür, Cirac and Zoller [Bri98] (or BDCZ-repeaters) utilize heralded entanglement generation [Bri98; Moe07; San11] to combat loss errors, and heralded entanglement purification [Deu96; Dür99; Kal17] for operation errors. In the taxonomy of Muralidharan, they are classified as first generation quantum repeaters. Heralded entanglement operations require two-way classical communication to confirm the successful herald detection. Second generation quantum repeaters invoke quantum error correction to correct operation errors, but continue to use heralded entanglement generation for loss errors [Jia09; Zwe14]. Quantum error correction demands faster gates with lower errors than the heralding entanglement operations, but requires only one-way communication of classical information, reducing the amount of classical information that must be sent. Finally, third generation quantum repeaters suppress both kinds of errors, loss and operational, via quantum error correction [Fow10; Mun12]. As opposed to the two other QR generations, no entangled pair need be created between the far distant end nodes of the quantum network. Instead, the entire quantum information is sent to the succeeding node, and errors are immediately corrected with error correction schemes. This means that the coherence time requirements of memory qubits are relaxed in comparison to the other QR generations.

Quantum repeaters of the first and second generation require (1) an efficient interface between a flying, generally photonic, qubit and a long-lived stationary quantum memory, (2) efficient quantum logic operations on the quantum memory, and (3) error correction codes or entanglement purification [Ben96; Cal96; Rei06b; Nig14; Ter15]. Furthermore, practical considerations suggest adding (4) a wavelength-transformer that converts photons to wavelengths near telecom wavelengths around 1.5 µm, where fiber losses are minimal. For third generation quantum repeaters, the requirements are basically identical, though the stationary quantum memory has far lower coherence time requirements, as stated above.

In this thesis, we focus on a trapped ion QR approach: trapped ions have the advantages of high fidelity gate operations and state readout, and a long coherence time. Many of the requirements for (2) are met, and modern ion trap technology allows for scaling up to the modest numbers of qubits required for a

QR. Light-atom interfaces (1) in the quantum regime have been demonstrated by placing ions into high-finesse optical cavities [Mun02; Ste14; Cas15]. Efficient error correction also requires high fidelity gate operations. Examples of error correction and purification (3) on ionic systems can be found in, e.g., [Rei06b; Nig14; Ter15]. Furthermore, single photon conversion to telecom wavelengths (4) has recently been demonstrated [Iku11; Zas12]. However, the scalable combination of (1 - 4) still appears to be very technologically demanding.

1.4 The Ion Trap

The experimental platform investigated and tested in this thesis is a microfabricated, linear Paul trap, an effective tool for trapping and manipulating multiple $^{40}\mathrm{Ca}^+$-ions, which is combined with a fiber-based cavity integrated into the trap setup.

Ion traps have been investigated for quantum computing experiments from 1995 on [Cir95] . A common architecture in use is a one-dimensional ion crystal in a linear Paul trap. Via a common vibrational mode of the crystal, it was possible to entangle a chain of up to 14 ions [Mon11]. The control over the ions with increasing crystal size scales badly, however, as decreasing the distance between individual ions creates cross talk when addressing the ions with a laser, and complicates the differentiation of individual ions during detection. Furthermore, the increase in vibrational modes magnify the difficulty of achieving high-fidelity quantum computing operations. To alleviate this, Kielpinski, Monroe and Wineland proposed a quantum charge-coupled device [Kie02]. This proposal featured many individual Paul traps, given by individually addressable electrode segments, aligned along multiple axes in a two-dimensional shape with multiple junctions, as seen in Figure 1.3. Since the electrodes can be dynamically supplied with a voltage, the ions can be shuttled along the Paul traps. Junctions are used to split off ions from the chain, and enable reordering of the crystals. Dedicated memory and interaction zones can feature trap environments especially suitable to their respective function. This allows scalably creating interactions between any arbitrary subset of ions in the trap.

Instead of the junctions of Kielpinski et al., which complicate the creation of a good trapping field, the ion trapping community has shifted to one-dimensional variants of the proposal, the *segmented linear Paul traps* [Sch06; Rei06a; Hom09]. Ion crystal reordering is achieved either via laser-induced SWAP gates mediated by a vibrational mode of the two-ion-crystal [Rie08], or by physically rotating the two ions [Kau17a]. These SWAP gates can be performed with high fidelity, and low excitation of motional quanta in the relevant nodes.

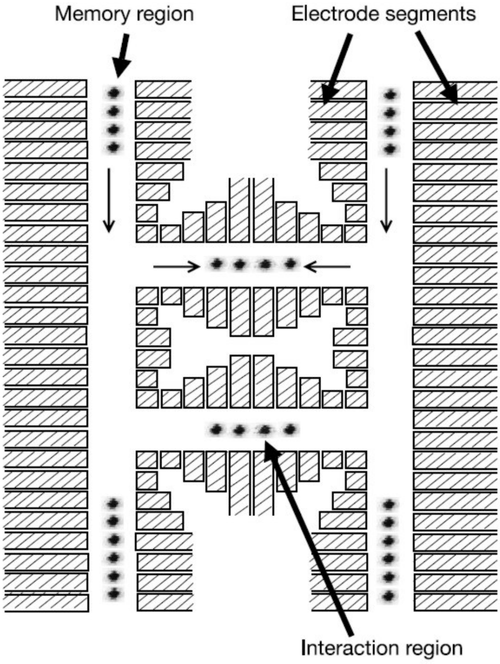

Figure 1.3: Quantum charge-coupled device envisioned by Kielpiski et al. Ions are shuttled along segments from memory regions to an interaction region. The junctions allow ion reordering, so that an arbitrary set of ions can interact with each other. Figure taken from Kielpinski et al. [Kie02], used with permission.

Finally, the microfabrication allows smaller trap dimensions than commonly found in linear ion traps. The trap structure is lasered into an assortment of ceramic wafers, with the conducting elements This results in higher trapping frequencies, which set a lower time limit for all operations done on ions, from gates to transports. The smaller dimension will also allow the integration of the fiber cavities without them protruding beyond the electrodes, while retaining a high finesse cavity with low mode volume.

1.5 Outline of the Thesis

The purpose of this work is to discover the extent to which ionic qubits are a promising platform for long distance entanglement distribution; and further, to ascertain which key rates we can expect in our search.

chapter 2 introduces the $^{40}\mathrm{Ca}^{+}$-ion and the pertinent equations of motion in

Paul traps, as well as the experimental tool set and apparatus we use to control and measure the qubits.

chapter 3 concerns qubit encoding, entangling gates and other tools required to create local and long-distance entanglement.

chapter 4 features an analysis of a choice of entanglement distribution protocols realizable on our setup. The protocols are introduced and rates of transmission and fidelities calculated, taking experimentally realistic settings into account.

chapter 5 describes the process of creating a microfabricated, segmented Paul trap with integrated fiber cavity. The fiber cavity is described with all necessary parameters[4]. In the course of this thesis, three different traps have been built, and the lessons learnt are reflected in this chapter.

chapter 6 then describes the attempt made in this thesis to move the ion into the cavity field, and analyzes possible explanations for the absence of cavity-ion interaction.

Finally, chapter 7 concludes this thesis, with thoughts on how to build on the results of this work.

---

[4] Details to the development and creation of the fiber cavity can be found in the PhD thesis of Marcel Salz, to be published in 2019.

2 Experimental Basics of Calcium Ion Qubits

In this chapter, we will review the experimental basics of calcium ion qubits, especially regarding trapping, transport and state manipulation.

2.1 The Calcium Ion

The stationary qubit realization used in all experiments of this thesis is based on the singly ionized ^{40}Ca atom. As an ionized earth-alkali atom, it has a single valence electron, providing it with a hydrogen-like level scheme, with states described in the (S,P,D) orbital scheme, as shown in Figure 2.1. However, due to imperfect shielding of the nucleus, spin-orbit-coupling in $^{40}\mathrm{Ca}^+$ results in the 4^2S orbital having a lower energy than the 3^2D manifolds. Thus, $^{40}\mathrm{Ca}^+$ exhibits metastable $|D\rangle$ states, unlike the hydrogen atom. These states are relevant to this thesis due to their longevity, for state readout, sideband cooling, and as a qubit implementation (see section 2.3).

The ground state of such an ionized calcium atom is $4^2\mathrm{S}_{1/2}$. The short-lived excited states $4^2\mathrm{P}_{1/2}$ and $4^2\mathrm{P}_{3/2}$ decay via electric dipole transitions of wavelengths 397 nm and 393 nm, respectively. The first of the two is used as Doppler cooling transition, where the short lifetime of 6.9 ns results in a fast and efficient Doppler cycle. Both levels have additional weak decay channels to the two D orbitals, $3^2\mathrm{D}_{3/2}$ and $3^2\mathrm{D}_{5/2}$.

2.2 Linear Paul Traps

The ions are trapped in a *linear Paul trap*, based primarily on the design of Schulz [Sch09], though adaptations described later were necessary for our experiment. Since the Earnshaw theorem shows it is impossible to create a local potential minimum with static electric fields alone [Ear42], ion traps have to either resort to combining electric and magnetic fields, as in the *Penning trap*, or to a combination of dynamic and static electric fields, as first described by Paul et al. [Pau53] and Fischer [Fis59], to trap ions. For an oscillating field of

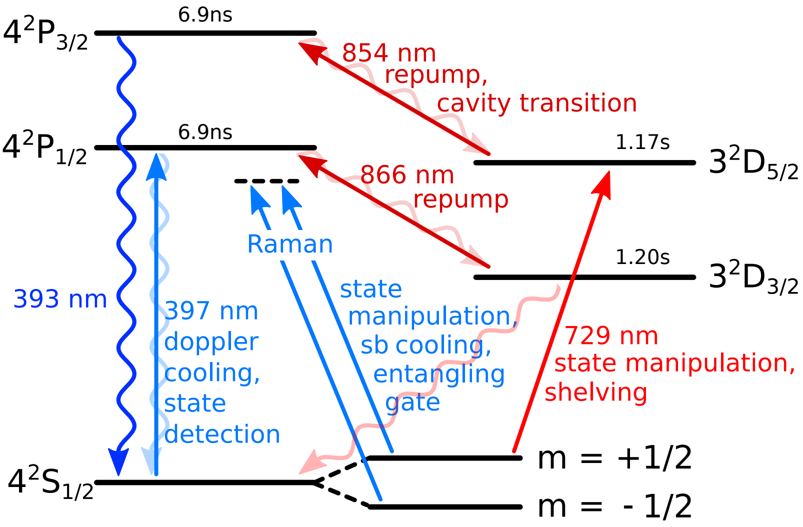

Figure 2.1: The relevant levels of $^{40}\mathrm{Ca}^+$ for this thesis. Included are the wavelengths and technical uses of the transitions, as well as the lifetimes of the excited states. Straight arrows indicate coherent transitions driven by lasers, while the solid wavy arrow describes an incoherent decay. All excited states in this thesis, except the quadrupole transition $|D_{5/2}\rangle \rightarrow |S\rangle$, de-excite mainly through incoherent decay even in the presence of laser light (i.e., they are in the weak coupling regime) unless the laser coupling can be enhanced by a cavity. This is indicated by the transparent wavy arrows underlying the respective coherent transitions.

amplitude U and frequency Ω_{rf}, and static field V, the scalar potential $\Phi(\boldsymbol{x},t)$ then takes the form

$$\Phi\left(\boldsymbol{x},t\right) = \sum_{i=x}^{z} \left(\frac{U}{2} \widetilde{\alpha}_i \sin\left(\Omega_{\text{rf}}\, t\right) + V \alpha_i \right) x_i^2 \ , \tag{2.1}$$

with the geometric factors of the static field α_i, and those of the dynamic field $\widetilde{\alpha}_i$. The potential must fulfill the Laplace equation,

$$\Delta\Phi\left(\boldsymbol{x},t\right) = 0 \ . \tag{2.2}$$

The exact solution of the Laplace equation is dependent on the trap geometry, but inserting Equation 2.1 indicates that it must be satisfied for both dynamic and static parts of the potential independently,

$$\sum_{i=x}^{z} \widetilde{\alpha}_i = 0 \qquad , \qquad \sum_{i=x}^{z} \alpha_i = 0 \ . \tag{2.3}$$

For the special case of linear Paul traps, the Laplace equations are solved by the relationships [Lei03b]

$$\alpha_x = \alpha_y = -\frac{1}{2}\alpha_z \quad , \quad \widetilde{\alpha}_x = -\widetilde{\alpha}_y \quad , \quad \widetilde{\alpha}_z = 0 \, . \tag{2.4}$$

Defining $\boldsymbol{\alpha} = (\alpha_x, \alpha_y, \alpha_z)^T$, $\widetilde{\boldsymbol{\alpha}} = (\widetilde{\alpha}_x, \widetilde{\alpha}_y, \widetilde{\alpha}_z)^T$, this potential then leads to the equations of motion

$$m\ddot{\boldsymbol{x}} = -Z\,e\nabla\Phi\left(\boldsymbol{x},t\right) = -Ze\left(2V\boldsymbol{\alpha} + U\widetilde{\boldsymbol{\alpha}}\cos\left(\Omega_{\text{rf}}t\right)\right)\boldsymbol{x} \tag{2.5}$$

in which the vector components x_i, $i \in x,y,z$, are independent of each other. The factor $Z\,e$ is the charge of the ion. Using the substitutions

$$\xi = \frac{\Omega_{\text{rf}}t}{2} \quad , \quad a_i = \frac{8ZeV\alpha_i}{m\Omega_{\text{rf}}^2} \quad , \quad q_i = \frac{2ZeU\widetilde{\alpha}_i}{m\Omega_{\text{rf}}^2} \tag{2.6}$$

Equation 2.5 can be transformed into the canonical form of the Mathieu differential equations

$$\frac{d^2\boldsymbol{x}}{d\xi^2} + \left(\boldsymbol{a} - 2\boldsymbol{q}\cos\left(2\xi\right)\right)\boldsymbol{x} = 0 \, . \tag{2.7}$$

Note that in the first approximation, $q_z = 0$, and the equation of movement along the trap axis is reduced to a simple oscillation of the ion.

The Mathieu equation can be approximated by the Ansatz

$$r_i(t) = r_{i,0} \cos\left(\frac{\beta_i}{2}\Omega_{\mathrm{rf}} t\right)\left(1 + \frac{q_i}{2}\cos\left(\Omega_{\mathrm{rf}} t\right)\right) , \tag{2.8}$$

$$\beta_i = \sqrt{a_i + \frac{q_i^2}{2}} , \tag{2.9}$$

which is a stable solution, i.e., the values for $\boldsymbol{r}$ are finite in all three dimensions $i \in \{\mathrm{x, y, z}\}$, for $0 \leq \beta_i \leq 1$. It is worth noting that β_i is the first-order approximation of the full Ansatz, given in Leibfried et al. [Lei03a] as a recursive function, or alternatively as a continued fraction. Equation 2.8 is thus only valid for small values of a_i and q_i, close to zero, which lie within the lowest stability region, in which Paul traps are operated. For a richer picture, we can consult Poschinger [Pos10], where the third-order approximation is given as

$$\beta^2 = a - \frac{(a-1)q^2}{2(a-1)^2 - q^2} - \frac{(5a+7)q^4}{32(a-1)^3(a-4)} - \frac{\left(9a^2 + 58a + 29\right)q^6}{64(a-1)^5(a-4)(a-9)} . \tag{2.10}$$

Figure 2.2 shows the stability regions for a linear Paul trap with this approximation, taking the symmetry requirements of Equation 2.4 into account. It shows that the difference to the first order approximation is negligible for a wide range of parameters.

2.2.1 Micromotion

Equation 2.8 shows the ion performing two distinct oscillations. The *secular motion*, described by the factor

$$\cos\left(\frac{\beta_i}{2}\Omega_{\mathrm{rf}} t\right) = \cos\left(\omega_i t\right) , \tag{2.11}$$

has an amplitude $r_{i,0}$, and a *trap frequency* ω_i along the axis i, which is reduced by a factor of $\frac{\beta_i}{2}$ compared to the trap drive frequency Ω_{rf}. In contrast, the second, faster and smaller, oscillation,

$$\frac{q_i}{2}\cos\left(\Omega_{\mathrm{rf}} t\right) ,$$

called *micromotion*, whose amplitude is reduced by a factor $\frac{q_i}{2} < 0.5$ compared to the secular motion, oscillates with Ω_{rf}.

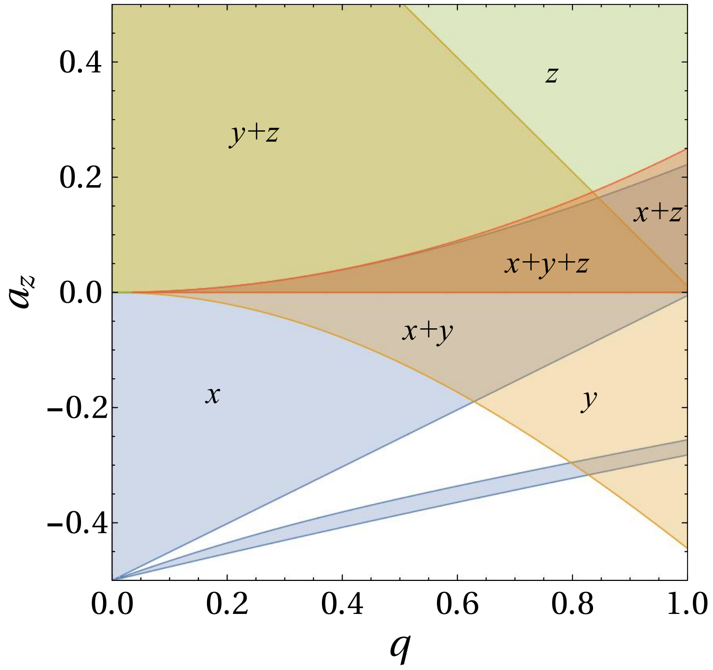

Figure 2.2: Stability regions of a Paul trap, with each β_i approximated by Equation 2.10. The different axes of stability are labeled in the figure. In addition, the first order approximation, as given in Equation 2.9, is overlaid in red. Up to $q \approx 0.8$, the differences to the third order approximation are negligible.

For some problems, it is useful to neglect the micromotion in the *secular approximation.* In this case, the applied radiofrequency field generates only a trapping force known as *ponderomotive force*, created by an effective harmonic potential, the *pseudopotential* Ψ. This transforms Equation 2.1 to the harmonic potential Φ_{secular}:

$$\begin{aligned} \Psi &= \frac{(Z\, e)^2 \, |\nabla V|^2}{4m\, \Omega_{\text{rf}}^2} \ , \\ \Phi_{\text{secular}}(\boldsymbol{x}) &= \sum_{i=x}^{3} \left[(\nabla \Psi)_i + V \alpha_i \right] \, x_i^2 \\ &= \sum_{i=x}^{3} c_i \, x_i^2 \ . \end{aligned} \tag{2.12}$$

The pseudopotential is independent of the time variations of the RF potential, and is as such amenable to static analysis. Because of this, it is a useful approximation to quickly calculate equilibrium properties of the trapped ion, such as the confinement strength of the ion due to the RF field, and the displacement of the ion due to the component of the RF field parallel to the trap axis in linear Paul traps sporting a taper. For more general considerations, like information about trapping stability or details of the micromotion, the full time varying potential must be evaluated instead.

2.2.2 DC and RF Potentials: Simulations

In order to optimize trapping parameters, and to facilitate fast cold ion transport and ion crystal separation (see subsection 2.2.3), it is necessary to simulate trapping potentials for the geometry used. In this work, we use the *Boundary Element Method* (BEM) coupled with a *Fast Multipole Method* (FMM) described in Singer et al. [Sin10]. Boundary element methods trade higher computational complexity for higher precision compared to finite element methods (FEM). The addition of FMM permits us to achieve a high precision while maintaining favorable scaling behavior with an increased number of simulated elements (i.e., surface elements in our case). The *BEMSolver* package [Sin10] developed in our group allows us to import a surface model of the trap, or construct it in code. *BemSolver* then subdivides the surfaces into smaller subelements. The field generating surface charges on these elements are then calculated in a self-consistent way, utilizing FMM to reduce the scaling with the overall number of elements N to $O(N)$ from $O(N^3)$ (though it still scales with the cube of the number of locally relevant surface elements p, $O(p^3)$. This value is, however, independent of overall size).

Results of a such a simulation for the electrostatic potentials created by the individual segments along the trap axis can be seen in Figure 2.3. Each individual line is the potential, along the line of the trap center, created by setting only this segment to 1 V, and the rest to 0 V. Despite the larger distance from the ion, the increased length of the segments in the loading and processor region leads to a higher feedthrough at the trap center.

The radial trapping of the RF field can be seen in Figure 2.4, where the pseudo-potential (see Equation 2.12) at typical RF-drive-voltages of $V_{rf}^{pp} = 200\text{V}$ is plotted for the surface perpendicular to the trap axis, at segment 1. The aspect ratio of the two radial trap axes, given by the trap slit of 350 µm width in the loading zone, and the spacer thickness of 250 µm separating the bottom and top chip of the trap (see section 5.2 ff), is visible in Figure 2.4 through the deformation of the ellipses of constant potential. In Figure 2.5, the same pseudo-potential is plotted at the height of the middle of segment 15. The aspect ratio of 1:1, due to the trap slit reduction to 250 µm width, results in a more symmetric potential. The closer electrodes also create a stronger confinement of the ions.

2.2.3 Transporting Ions and Separating Ion Crystals

Segmented linear Paul traps have the capability to shuttle ions from one segment to another, e.g., to move an ion into and out of the laser interaction zone. To be able to complete the necessary gates of an experimental sequence before the various sources of decoherence have time to act on the qubit, the optimal transport is performed as quickly as possible. However, if the ion is naively shot from one segment to another, the motional state of the ion will be perturbed by coherent excitations, beyond the tolerances of the Lamb-Dicke regime, reducing the fidelity of quantum gates. Thus, it is of paramount importance to carefully craft a transport ramp that will be finished as quickly as possible without disturbing the motional state of the ion.

The transport ramps of this project are of a modular build, meaning that a transport from segment 6 to segment 32 is reduced to 25 one-segment transports. For each of the single segment transports, the basic idea is to ramp the current segment from the trapping voltage to zero volts, while simultaneously ramping down the voltage of the neighboring target segment to trapping depth. The simplest solution of the problem of motional excitation is to choose a smooth, monotonic function ramped, so that transport between neighboring segments is entirely *adiabatic*, that is, the ion is in a non-excited motional state for the entire duration of the transport. Since the trapping stability and heat-

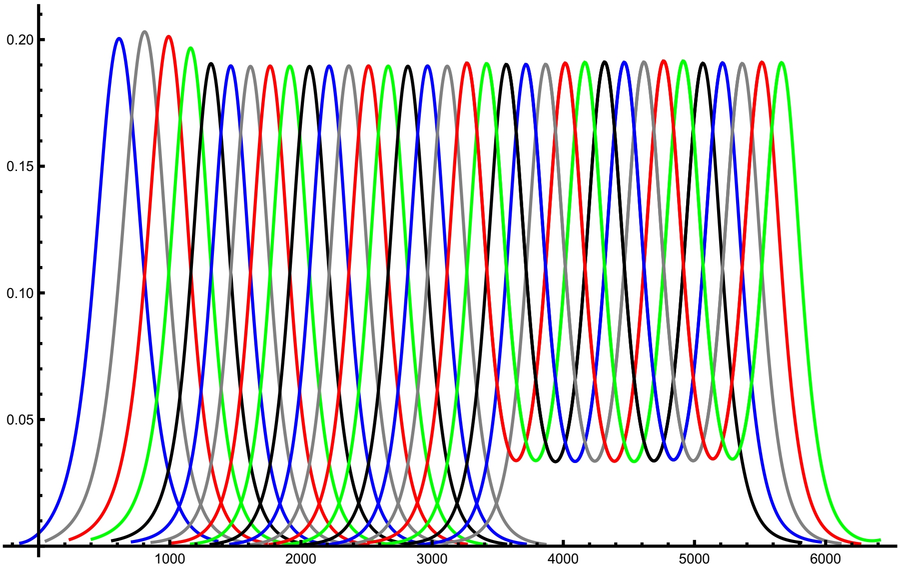

Figure 2.3: Simulated potential functions for all segments of the Fibertrap V3 along the trap axis. In a coordinate system with the z-axis parallel to the trap axis, and the x- and y-axes lying in the radial directions, the figure shows the electrostatic potential in Volts at the point (0,0,z) in micrometers created by the respective segment set to a potential of 1 V, with all others set to 0 V. Visible are the increased feedthrough of the segments of the loading zone and the taper, in the first four lines on the left, and the connected segments on the right, where the potential feedthrough does not reach 0 V between the peaks of one set of segments. Segments are counted from left to right, so the first blue line corresponds to segment 1, the gray one to segment 2, and so on, until the last green line on the right is the potential created by the connected segments 19, 24, 29 and 34.

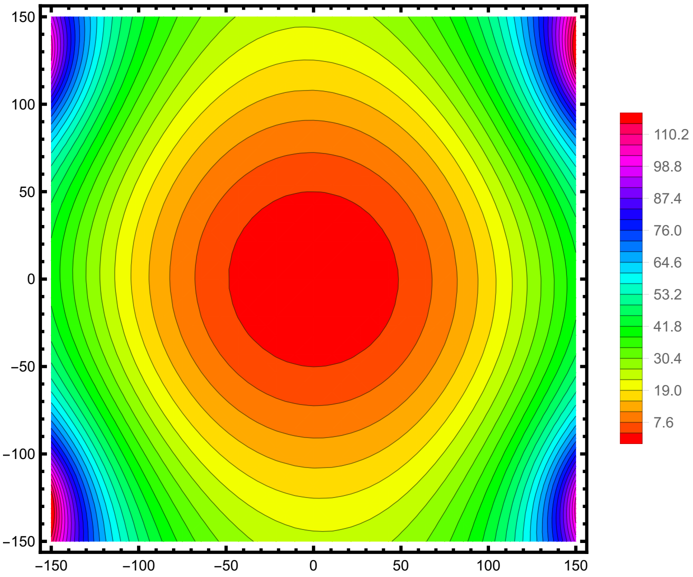

Figure 2.4: Simulated RF potential at the center of segment 1 in the loading zone, in the plane perpendicular to the trap axis. The plot axes are in units of micrometers offset from the trap axis. Note the deformed major axes of the ellipsis circumscribed by the equipotential lines. This is the effect of the aspect ratio of the trap slit to the spacer thickness, which is $350/250 = 7/5$ in the loading zone.

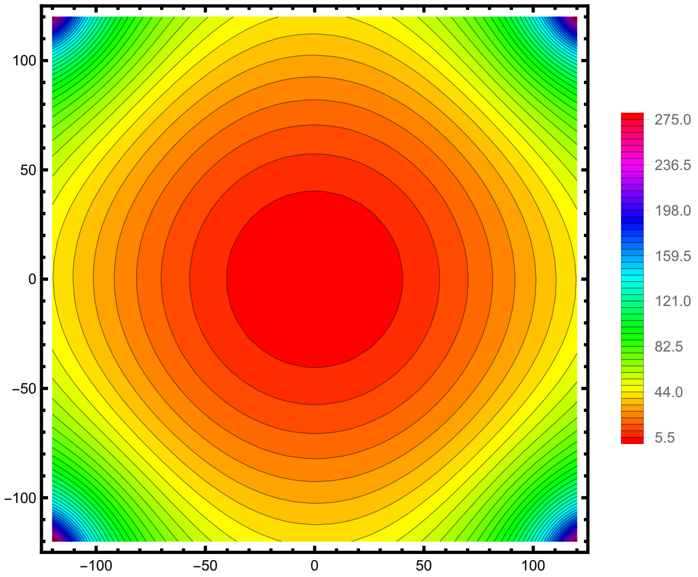

Figure 2.5: Simulated RF potential at the center of segment 15 in the processor zone, in the plane perpendicular to the trap axis. The plot axes are in units of micrometers offset from the trap axis. Note the far lower deformation of the axes of the ellipsis in comparison to Figure 2.4, due to the aspect ratio of the trap being 1:1 in the processor zone.

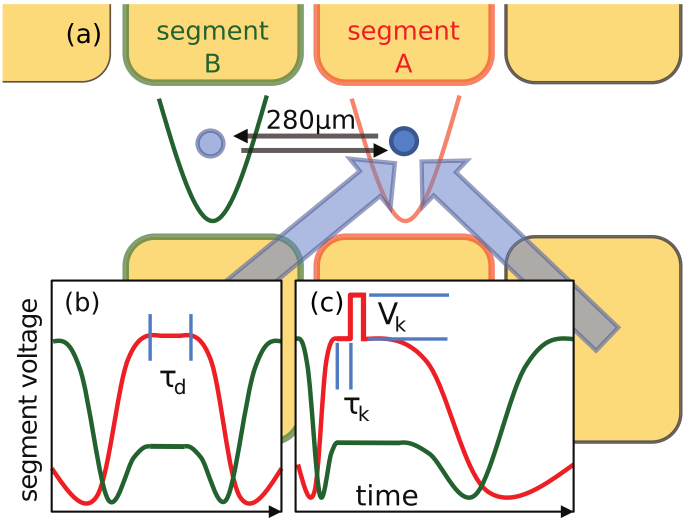

Figure 2.6: a) Transport from segment A to B, into and out of the laser interaction zone. b) Pairwise neutral transport, see text. c) Self-neutral transport: a voltage kick V_k, here on segment A, at the end of the first transport operation, after a time τ_k, removes the coherent motional excitation from the ion. Picture taken from Walther et al. [Wal12], used with permission.

ing rate of the ion both depend on it, we add the requirement that the axial trap frequency ω_ax, and as such the curvature of the DC field along the transport axis, should be constant. The adiabatic limit can generally be reached for transport times longer than a few dozen revolutions of the ion in ω_ax [Rei06a].

If the transports are carefully timed, so that the duration is a multiple of $2 \times \omega_\mathrm{ax}$, coherent excitations of the motional quanta can be strongly reduced [Rei06a]. This leads to two extensions of ionic transport beyond the adiabatic limit developed in this group [Wal12], making faster cool transport possible. The first extension, called *pairwise neutral transport* (Figure 2.6 a), times a transport and return operation so that any coherent excitation of the motional modes during the first transport is undone by the second. More generally useful is the second extension, *self neutral transport* (Figure 2.6 b), which observes that a coherent excitation can also be induced, and thus removed, by a short voltage ”kick” after the transport operation. In Walther et al. [Wal12], it was possible to transport an ion over 240 µm in 3.6 µs, inducing an average motional excitation of only 0.1 phonons.

With these numbers, self neutral transport from one segment to another can be used as a basic operation to create transports of arbitrary length along the trap. Alternatively, it is possible to create a ”monolithic” transport operation for each distance, with a single voltage kick at the end of the process. The experiments performed in the course of this thesis do not require ground state cooled ions yet, and for simplicity, only simple adiabatic transport has been used. However, the entanglement distribution techniques described in section 4.1 require the possibility of performing cool, fast transports.

2.3 State Manipulation and Readout: Laser and Camera Setup

2.3.1 Ionizing Calzium-40

Neutral calcium is produced in the vacuum chamber by heating a calcium oven [Rot03], which is filled with 99.95 % pure ^{40}Ca granules[1], by using roughly 3.5A of electrical current. A cloud of neutral atoms expands into the trapping region of the ion trap, where they are ionized through a resonantly enhanced two-step ionization process. A laser with a wavelength around 423 nm excites one valence electron from the $4^2\mathrm{S}_0$ ground state to the $4^2\mathrm{P}_1$ state. From there, a free running laser at 393 nm pushes the electron into the continuum, ionizing the atom. This method has the advantage of being isotope selective, removing any possible remnant of ^{43}Ca. Since the trapping force of a Paul trap is conservative, the ion must be created close to the trap axis to be retained. Neither laser requires locking, as the transitions are wider than the laser linewidth.

2.3.2 Encoding Qubits

$^{40}\mathrm{Ca}^+$ allows for encoding a qubit, comprised of the two states $|0\rangle$ and $|1\rangle$, in two basically distinct ways (Figure 2.8): One possibility is the *spin qubit* [Pos09], where the ground state levels $\left|S_{1/2}, \downarrow\right\rangle$ and $\left|S_{1/2}, \uparrow\right\rangle$ represent the logical states. Alternatively, we can utilize an *optical qubit* [Roo99; Sch13], where either one or two of the logical states is represented by one of the sublevels of the long-lived metastable $\left|D_{5/2}\right\rangle$ state. The coherence times for both qubits is up to $10 - 100$ ms, limited by magnetic field fluctuation.

The experiment set up in this work has only realized a setup for optical qubits so far, though spin qubits are used in this group as a matter of course. The

---

[1] Calcium granules, redistilled, -16 mesh, 99.5 % (metals basis), Alfa Aesar GmbH & Co KG, Zeppelinstraße 7b, 76185 Karlsruhe, Germany

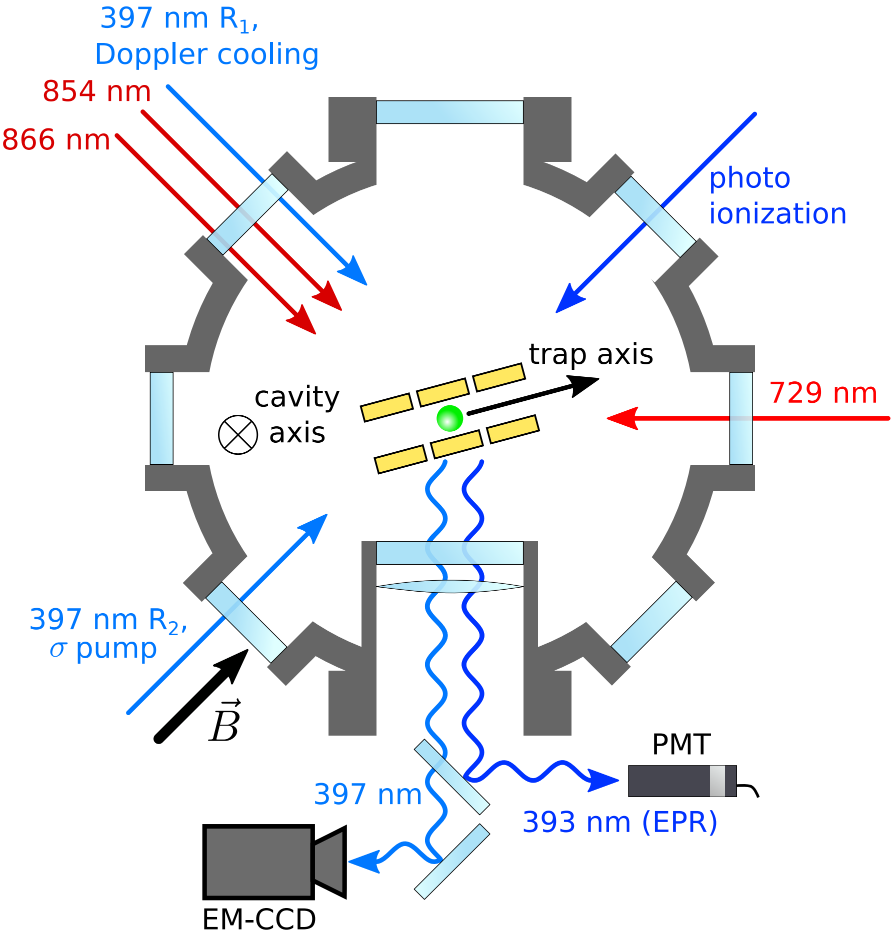

Figure 2.7: Beam geometry of the experimental setup, viewed from the top. Arrows indicate directions for laser beam propagation and the quantization axis defined by the magnetic field $\boldsymbol{B}$. R_1 and R_2: Beams used for driving Raman transitions between $\left|S_{1/2}, \pm 1/2\right\rangle$. Other lasers are described in the text. A lens in the inverted viewport (bottom) collects scattered 397 nm light (and for the EPR-protocol, also 393 nm light) for detection. The cavity axis is perpendicular to plane the of view.

light source for the quadrupole transition is a narrow-linewidth diode laser at

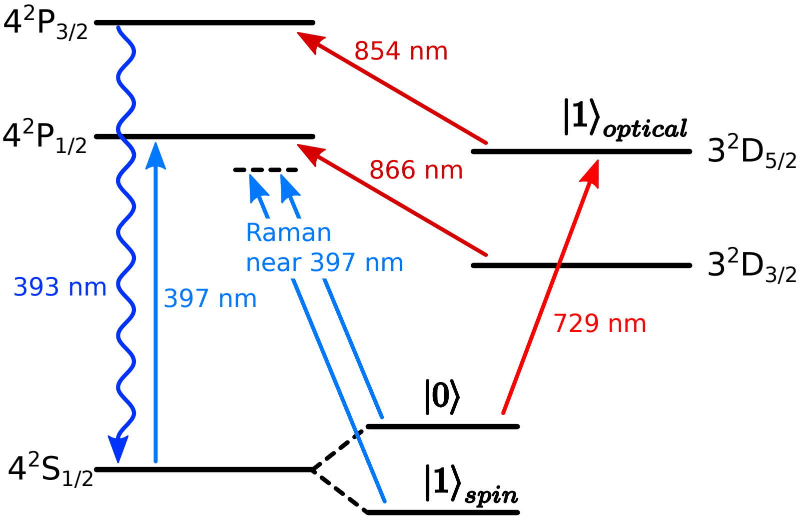

Figure 2.8: Possible qubit implementations for ^{40}Ca^{+}-ions. Shown are the spin qubit, with both logical qubits encoded into the two ground state levels of $\left|S_{1/2}\right\rangle$, and the optical qubit, for which one of the logical states is encoded in a sublevel of the $\left|D_{5/2}\right\rangle$ orbital. For details, see subsection 2.3.2.

729 nm[2], which is locked to a high-finesse cavity[3].

2.3.3 Cooling

For each experimental run, the ion is brought into the Lamb-Dicke regime via *Doppler cooling* [Win78] on the $|S_{1/2}\rangle \leftrightarrow |P_{1/2}\rangle$ *cycling transition* near 397 nm. The laser is red-detuned, so that the ion is in resonance with the beam only during movement along the beam axis *towards* the beam's source. The absorption of a photon imparts a force equivalent to the impulse $p = \hbar k$ of the photon opposite to the ion's direction of movement. This cooling effect is counterbalanced by both the statistical nature of absorption, as well as the undirected emission of photons by the excited ion, which heats the ion along the direction of emission. The minimal steady-state temperature is reached for a detuning of $\delta = \Gamma/2$. For a derivation of this value and a detailed description of the process of Doppler cooling see Roos [Roo00] or Poschinger [Pos10]. Typical average phonon numbers lie in the range of $\bar{n} \approx 20$ on the axial mode of vibration.

The setup also allows us to employ *resolved sideband cooling* on either kind of qubit. In both cases, the idea is to drive the first red sideband of the spectroscopic transition of the respective qubit. The ion imparts the energy of one phonon into the transition, reducing its kinetic energy [Mon95]. For the optical qubit, the quadrupole transition from $|S_{1/2}, +1/2\rangle$ to the respective outer magnetic substate ($|D_{5/2}, +5/2\rangle$) is driven on the first red sideband. The electron is repumped by 854 nm light to $|P_{3/2}, +3/2\rangle$, from where the only possible single-photon decay into the S state is the $m_J = +1/2$ spin state, keeping the spin polarization of the ion intact. However, the $|P_{3/2}\rangle$ orbital also has a 6 % chance to decay back to $|D_{5/2}\rangle$, which then opens up the possibility of ending in the wrong $|S\rangle$ spin configuration, via the faded arrows in Figure 2.9 . To counteract the loss of spin coherence, optical pumping is performed every 10 cooling cycles.

For the spin qubit, we drive a stimulated Raman transition between the Zeeman ground states of the $S_{1/2}$ state for a spin qubit, or by driving a red sideband transition, to cool close to the ground state of the axial mode. The repumping is accomplished by employing a circularly polarized laser field, driving the cycling transition. Typically attainable average phonon numbers are lower than 0.05 in the axial mode with pulsed sideband cooling.

---

[2] TA 100, Toptica Photonics AG, Lochhamer Schlag 19, 82166 Gräfelfing, Germany

[3] Advanced Thin Films, 5733 Central Avenue, Boulder, CO 80301, USA

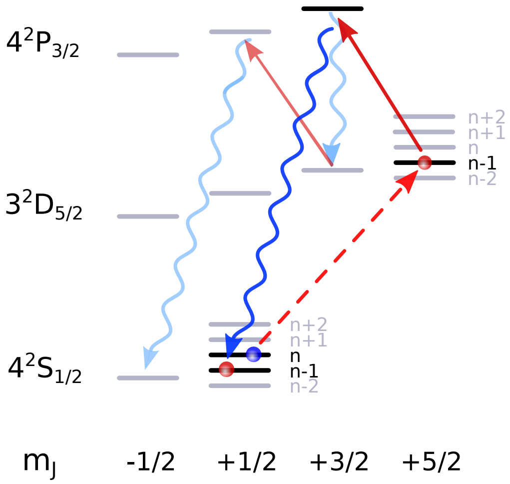

Figure 2.9: Energy levels of resolved sideband cooling for optical qubits. The ion is colored blue when in the n-phonon "hot" state, and red in the $(n-1)$-phonon "cold" state. The coherent quadrupole transition is dashed red, the repumper at 854 nm solid red, and incoherent decays are blue wavy lines. The faded transitions are parasitic decays that degrade the spin coherence of the ion.

2.3.4 State Readout

Readout of the optical qubit is performed by fluorescence detection on the cycling transition with an EM-CCD camera or a photomulitplier tube (PMT).

For the spin qubit, it is necessary to *shelve* one of the qubit states by transferring population from it with a π-pulse on the $|S_{1/2}\rangle \leftrightarrow |D_{5/2}\rangle$ quadrupole transition. Instead of a single π-pulse, one can use rapid adiabatic passage pulses [Vit01], for which a light field is slowly turned on and off while its frequency is swept over the transition's resonance, since RAP pulses are more robust than simple π-pulses. In order to effectively deplete the $|S_{1/2},\uparrow\rangle$ state, two RAP pulses to two different substates of the $|D_{5/2}\rangle$ manifold can be performed. The readout then proceeds analogous for both the optical qubit and the spin qubit.

$10-200\,\mu\mathrm{W}$ of Doppler-cooling-light are shone in, while only the 866 nm repumper is active. Thus, $|D_{5/2}\rangle$ is kept out of the Doppler cycle. The EM-CCD camera takes a picture for $5-50\,\mathrm{ms}$, which is evaluated for the number of counts. A bright event corresponds to the $|S_{1/2}\rangle$ state, and a dark event the $|D_{5/2}\rangle$ state. For high-fidelity requirements, the setup allows the addition of a PMT, which can reach a comparable state differentiation fidelity with roughly an order of magnitude quicker detection times. Readout fidelities of ≈ 0.995 can then be obtained for either qubit species.

2.4 High NA Optics and Optical Cavities

High NA Optical Access

The high readout fidelity for the camera is made possible in part by the high-NA, spherical-aberration-corrected lens system positioned as close to the trap as feasible via the inverted viewport, see Figure 2.7. The lens system is provided by Sill Optics[4]. The light is then funneled to the camera via a closed off tube system, to reduce stray light from the lab. A wavelength filter[5] mounted on the camera objective removes any light outside a narrow band around a wavelength of 397 nm. The distance of the camera to the high-NA lens system defines the magnification of the setup, which in our case is easily adjustable thanks to a system of extendable tubes and tracks. Typical values lie around 15-20× magnification. The camera is an EM-CCD device by Andor Technology[6].

---

[4] S6ASS2214/45, Sill Optics GmbH & Co. KG, Johann Höllfritsch-Str. 13, 90530 Wendelstein, Germany

[5] filter details

[6] ixon+, DU-860D-CS0-UVB, Andor Technology Ltd., 7 Millenium Way, Springvale Business Park, Belfast BT12 7AL, United Kingdom

Fiber-Based Cavity

In order to increase the coupling of light to the ions, and thus realize an interface between flying and resting qubits, we integrated a cavity into our trap. To keep losses minimal, and to achieve a high coupling of the ion to the cavity mode, the mode volume is kept as low as possible. Due to its small size, a fiber based Fabry-Pérot-cavity [Col07; Ste14; Bra13], where highly reflective dielectric mirrors are sputtered onto end facets of optical fibers, can fulfill this requirement. It is suited to be accommodated between the two electrode chips, providing direct coupling into the cavity via one of the fibers.

The cavity drives the $\left|D_{5/2}\right\rangle \leftrightarrow \left|P_{3/2}\right\rangle$ transition near λ =854 nm. The respective field coupling parameter, i.e., the vacuum Rabi frequency g_0, is given by:

$$g_0 = \sqrt{\frac{3\,c\lambda^2\gamma_{\mathrm{PD}}}{\pi^2 w_0^2 L}}\ , \tag{2.13}$$

where $\gamma_{\mathrm{PD}} = 2\pi \times 0.67$ MHz is the radiative field decay rate of the $\left|D_{5/2}\right\rangle \leftrightarrow \left|P_{3/2}\right\rangle$ transition. The cavity mode waist w_0 is set by choosing the radius of curvature (ROC) and the length L of the cavity. The range of suitable values for L is predetermined by the trap dimensions: Both the fibers and the mirror surfaces are comprised of insulating materials, which are prone to uncontrolled charging when exposed to UV laser light, leading to uncontrolled electric stray fields in the trap [Har10; Her11]. However, the trap dimensions cannot be arbitrarily small, since short distances of the electrode surfaces to the ion increase the anomalous heating rates [Bro14] and the optical access needs to be ensured. The cavity length L is thus chosen sufficiently large, such that the fibers are retracted behind the trap electrodes (see Figure 5.2), reducing the electrical feedthrough of the charged insulating surfaces to the trap volume. We utilize a plano-concave cavity setup to reach a high mode matching ε between the mode that emanates from the fiber and the cavity mode. The ROC of the concave mirror can be chosen such that the waist is small while cavity stability and high mode matching are ensured.

2.5 Experiment Control

Central control of the experiment is provided by a program written in C++ that creates the required hardware control sequences and evaluates the measurement results. This encompasses control of the AOM drivers, creating and transferring via USB sequences for the programmable frequency generator controlling the

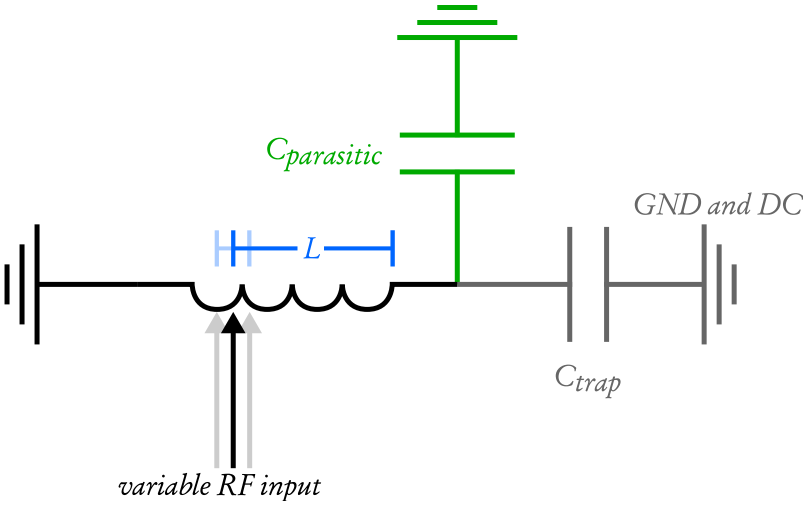

Figure 2.10: Electric schematic of a helical resonator as used in our experiment. The LC circuit is comprised of the helical resonator itself (black) and the RF electrodes of the trap, which are coupled to ground (GND) via the other trap electrodes with the capacitance of C_{trap} (gray). Optionally, an additional parasitic capacitance can be added to the output (green). The inductance L can be controlled by shifting the insertion point of the RF input.

729 nm spectroscopy laser, and readout of the EMCCD camera or PMT device used. Finally, via ethernet the program controls a multichannel arbitrary waveform generator (MAWG) developed in-group, based on a *Field Programmable Gate Array* (FPGA). We use the MAWG to both time laser triggers sent via digital channels, at a sample rate of 50 GSamples/s, as well as to perform the analog sequences that control all DC and compensation electrodes of the trap [Wal12; Rus14]. The MAWG is capable of providing stable voltages between -40 to 40 V with a resolution of 0.3 mV, at ~ 2.6 GSamples/s .

The trap drive radiofrequency Ω_{rf} with amplitude U is supplied by a waveform generator[7]. The output of this generator is passed on to a +30 dB amplifier, and from there to a helical resonator [Mac59] (circuit schema see Figure 2.10). The helical resonator creates a simple RLC-circuit from its inductance and the sum of its own and the ion trap's capacitance. The result is a filtering of the incoming signal, removing the unwanted contributions from all frequencies

---

[7] SMB 100A signal generator, Rohde & Schwarz GmbH & Co. KG, Mühldorfstraße 15, 81671 München

but those in a narrow band around the requested trap drive frequency, with resonance

$$\Omega_{\mathrm{rf}} = \frac{1}{\sqrt{LC}} \,, \tag{2.14}$$

where L is the inductance of the resonator, and C the combined capacitance of the resonator and the ion trap. The quality of the filtering is measured by the Q-factor

$$Q = \frac{1}{R}\sqrt{\frac{L}{C}} \tag{2.15}$$

of the resonator-trap system. In addition, the effective inductance L of the helical resonator can be adapted by tuning the input point of the signal, lengthening or shortening the used coil length as required, to match the impedance

$$|Z| = \sqrt{R^2 + \left(\Omega_{\mathrm{rf}} L + \frac{1}{\Omega_{\mathrm{rf}} C}\right)^2} \tag{2.16}$$

of the resonator-trap system to the $50\,\Omega$ output of the amplifier. In order to also be able to shift the resonance frequency over a larger domain, we can add a tunable parasitic capacitance to the system in parallel to the ion trap. This allows us to reduce the resonance frequency while keeping the matched impedance, albeit at the cost of a reduced Q-factor.

3 Theoretical Elements and Tools

3.1 Light-Ion Interactions

This section mainly follows the two books *Atomic Physics: an exploration through problems and solutions* [Bud08] and *Exploring the Quantum* [Har06] in its presentation, though very similar treatment of the topic can be found in many textbooks for atomic physics.

3.1.1 Two-Level Systems

In order to model the interaction of a $^{40}\mathrm{Ca}^{+}$-ion with laser light, we will treat the ion as a two-level system under periodic perturbation. The state of the system in the Schrödinger picture is described by the wave function

$$|\Psi(t)\rangle = \begin{pmatrix} c_g(t) \\ c_e(t) \end{pmatrix} = c_g(t)\,|g\rangle + c_e(t)\,|e\rangle \ , \tag{3.1}$$

whose time evolution follows by the Schrödinger equation

$$i\hbar\partial_t\,|\Psi(t)\rangle = H\,|\Psi(t)\rangle \ . \tag{3.2}$$

The two levels under consideration are a ground state, $|g\rangle \equiv (1{,}0)^T$ and an excited state $|e\rangle \equiv (0{,}1)^T$. The coherent laser field moving along the $\boldsymbol{e}_k$-direction is characterized by the electric field

$$\boldsymbol{F}(t) = \boldsymbol{\epsilon}F_0 \sin\left(\boldsymbol{k}\cdot\boldsymbol{x} - \omega_{\mathrm{L}}t\right) \ , \tag{3.3}$$

with a circular frequency ω_{L}, a field amplitude of F_0 and a polarization vector $\boldsymbol{\epsilon}$. This light field couples with the transition via the dipole or quadrupole matrix element, given by

$$\begin{aligned} M_{ge}^{E1} &= e\,\langle g|\,\boldsymbol{\epsilon}\cdot\boldsymbol{r}\,|e\rangle \\ M_{ge}^{E2} &= e\,\langle g|\,\boldsymbol{\epsilon}\cdot(\boldsymbol{r}\circ\boldsymbol{r})\cdot\boldsymbol{e}_k\,|e\rangle \ , \end{aligned} \tag{3.4}$$

and a coupling term V in the Hamiltonian, which is proportional to the light field's amplitude, $V \propto F_0$. The Hamiltonian of the system is then represented by an interaction free term, with the unperturbed energies of the ground and excited states, and the interaction term, coupling the two, which should be small compared to the first:

$$\begin{aligned} H &= H_0 + V \ , \\ H_0 &= \hbar\omega_0 \left|e\right\rangle \left\langle e\right| \ , \\ V &= -\hbar\Omega \sin(\omega_{\mathrm{L}} t) \left(\sigma^+ + \sigma^-\right) \ , \\ \sigma^+ &\equiv \left|e\right\rangle \left\langle g\right| = (\sigma^-)^\dagger \ , \\ \omega_0 &\gg \Omega \ . \end{aligned} \tag{3.5}$$

The last requirement enables standard perturbation theory. Here, ω_0 is the circular frequency of the transition in question, and Ω is the transition rate induced by the light field $\boldsymbol{F}$, called *Rabi frequency* of the transition:

$$\hbar\omega_0 = H\left(\left|e\right\rangle - \left|g\right\rangle\right) = E_e - E_g \ , \tag{3.6}$$

$$\hbar\Omega = \frac{F_0 M_{ge}\left(\boldsymbol{\epsilon}\right)}{\hbar} \ . \tag{3.7}$$

The form of Equation 3.5 implies that we set the energy zero-point to the ground state energy E_g. It is possible to transform this Hamiltonian into a frame rotating with ω_0 using the unitary operator

$$U = \left|g\right\rangle \left\langle g\right| + e^{-i\omega_{\mathrm{L}} t} \left|e\right\rangle \left\langle e\right| \ , \tag{3.8}$$

and the transformed wave function and Hamiltonian

$$\begin{aligned} \left|\Psi'\right\rangle =& U^\dagger \left|\Psi\right\rangle \ , \\ H' =& U^\dagger H U \ , \end{aligned}$$

giving rise to the effective Hamiltonian

$$H_i = U^\dagger H U - i\hbar U^\dagger \partial_t U \ , \tag{3.9}$$

with the additional time derivative following from inserting the transformed operators and wave functions into the Schrödinger equation, and signifying that the new reference frame is not inertial. This effective Hamiltonian written out is now

$$H_i = \begin{pmatrix} 0 & -\frac{\hbar\Omega}{2i}\left(1 - e^{-i2\omega_{\mathrm{L}} t}\right) \\ \frac{\hbar\Omega}{2i}\left(1 - e^{i2\omega_{\mathrm{L}} t}\right) & -\hbar\delta \end{pmatrix} \ , \tag{3.10}$$

where we have introduced the *laser detuning* $\delta = \omega_\mathrm{L} - \omega_0$ from resonance, which obviously disappears if the laser is tuned to the transition frequency.

In the *rotating wave approximation* (RWA), the quickly rotating terms proportional to $e^{\pm i2\omega_\mathrm{L}t}$ are neglected, since they average out over times that are far to0 short for us to probe experimentally, finally giving us the RWA Hamiltonian

$$H_i \approx H_\mathrm{rwa} = \begin{pmatrix} 0 & -\frac{\hbar\Omega}{2i} \\ \frac{\hbar\Omega}{2i} & -\hbar\delta \end{pmatrix} . \tag{3.11}$$

For the resonant case, $\delta = 0$, the Schrödinger equation thus reduces to two simple differential equations

$$\begin{aligned} \dot{c}_g(t) &= \frac{\Omega}{2} c_e(t) , \\ \dot{c}_e(t) &= -\frac{\Omega}{2} c_g(t) , \end{aligned} \tag{3.12}$$

with the solutions

$$\begin{aligned} c_g(t) &= \cos\left(\frac{\Omega}{2}t\right) , \\ c_e(t) &= \sin\left(\frac{\Omega}{2}t\right) , \end{aligned} \tag{3.13}$$

for the initial condition that the ion is entirely in the ground state at $t = 0$.

Since the probability to find the system in the state $|e\rangle$ is given by the square of the wave function projected onto that state, the probability to find the ion in the excited state is

$$p_e(t) = |\langle e| \Psi(t) |e\rangle)|^2 = |c_e(t)|^2 = \sin^2\left(\frac{\Omega}{2}t\right) \tag{3.14}$$

when measured at time t. This oscillating probability can be probed by repeated measurements, and the resulting curve is known as *Rabi oscillation* or *Rabi flops.*

3.1.2 Two-Level Ions in a Harmonic Trap

For ions in a Paul trap with a fiber cavity, there are two quite different processes that are well described by coupling a spin-1/2 system to a quantum harmonic oscillator: Firstly, the ion's motion in the trap can be coupled to its internal state via a classically described laser. As Equation 2.12 shows, the ion in the quadratic trapping potential is indeed a harmonic oscillator. Secondly, the light field of the cavity is well described as a harmonic oscillator. While this subsection is concerned with the first system, the second one is covered/dealt with further down in subsection 3.1.3.

The equations are constrained to the one-dimensional case for simplicity. Extension to all spatial dimensions is easily done. The derivation in subsection 3.1.1 neglects the effects of ion motion in the trap. The evolution of a mechanical oscillator in a harmonic potential is given by the single harmonic oscillator Hamiltonian:

$$H_{ho} = \frac{p^2}{2m} + \frac{m\omega^2}{2}x^2 \, . \tag{3.15}$$

Rescaling the position x and momentum p to the commonly used quadratures P and Q,

$$\begin{aligned} x =& \sqrt{\frac{m\omega}{2\hbar}}X \ , \\ p =& \frac{P}{\sqrt{2m\omega\hbar}} \ , \end{aligned} \tag{3.16}$$

results in the Hamiltonian

$$H_{\mathrm{ho}} = \hbar\omega \left(P^2 + X^2\right) \ . \tag{3.17}$$

If we define the *annihilation operator* $a = P + iX$ and its conjugate transposed counterpart $a^\dagger = P - iX$, the *creation operator*, we get the canonical expression for the Hamiltonian of a single harmonical oscillator:

$$H_{\mathrm{ho}} = \hbar\omega \left(a^\dagger a + \frac{1}{2}\right) \ . \tag{3.18}$$

As the Hamiltonian is proportional to $a^\dagger a = N$, the *number operator*, which counts the excitations of the oscillator, its eigenstates are the so-called *Fock states* $|n\rangle$. The energy of the Fock state $|n\rangle$ is $E_n = (n + 1/2)\hbar\omega$, so that the spectrum consists of a "ladder" of equidistant energies starting at the *vacuum energy* $\hbar/2$. When the vacuum energy is of little interest, it is possible to rescale the system so that it disappears,

$$H_{\mathrm{ho}} = \hbar\omega a^\dagger a \ . \tag{3.19}$$

The constant spacing $\hbar\omega$ is the quantum belonging to the system. In the case of trapped ions, the quanta are motional excitations usually called *phonons*[1].

---

[1] In other areas of physics, phonons are generally defined as quanta of collective vibrational modes. The use for motional excitations of single atoms pervades atomic physics, however,

Combining this Hamiltonian with the two-level Hamiltonian of the previous section, Equation 3.5, the model becomes

$$H = H_0 + V = \hbar\omega_i a^\dagger a + \frac{\hbar\omega_0}{2}\sigma_z + V \ . \tag{3.20}$$

In contrast to Equation 3.5, the non-interacting Hamiltonian has terms for both the motional and the internal state, with the trap frequency along the chosen axis, ω_i, and the energy splitting of the ground and excited state ω_0 as before. An important difference to the previous section's treatment of the light field is the ability of the ion to move with respect to the reference frame of the field, incurring an additional phase shift $e^{ikx\cos(\theta)}$:

$$V = -i\hbar\frac{\Omega}{2}e^{-i\omega_\mathrm{L}t}e^{ikx\cos(\theta)}e^{-i\phi}\sigma^+ + h.c. \ , \tag{3.21}$$

where θ is the angle between $\boldsymbol{k}$ and the axis of the oscillator, and ϕ the phase of the laser at the ion's center of motion. In terms of creation and annihilation operators, the ion displacement in a harmonic oscillator can be described by $x = x_0(a + a^\dagger)$, and the phase factor becomes

$$\begin{aligned} e^{ikx\cos(\theta)} =& e^{i\eta(a+a^\dagger)} \ , \\ \eta =& kx\cos(\theta) \ , \end{aligned} \tag{3.22}$$

with the *Lamb-Dicke parameter* η. If this parameter is small,

$$\eta\sqrt{\langle(a^{\dagger 2} + a^2)^2\rangle} \ll 1 \ , \tag{3.23}$$

the system is in the *Lamb-Dicke regime* [Lei03a], which is characterized by $\sqrt{\hbar/2m\omega_i} \ll k$, i.e., the extent of the ionic wave-packet being much smaller than the wavelength of the laser. In the Lamb-Dicke regime, which we will be considering from here on, the exponential function of Equation 3.22 can be simplified by a Taylor expansion around η up to first order,

$$V \approx -i\hbar\frac{\Omega}{2}e^{-i\omega_\mathrm{L}t}(1 + i\eta a^\dagger + i\eta a)e^{-i\phi}\sigma^+ + h.c. \ . \tag{3.24}$$

We again switch to the interaction picture with regards to H_0, using the

---

and will be used throughout the thesis.

unitary transformation $U = e^{iH_0 t/\hbar}$ and get the interaction Hamiltonian

$$H_I = \hbar\omega_i a^\dagger a + \frac{\hbar\delta}{2}\sigma_z - i\hbar\frac{\Omega}{2}e^{-i\delta t}(1 + i\eta a^\dagger{}_I e^{i\omega_i t} + i\eta a_I e^{-i\omega_i t})e^{-i\phi}\sigma^+ + h.c. \ , \tag{3.25}$$

where the operators transform as $a^\dagger \to a^\dagger{}_I e^{i\omega_i t}$ and $a \to a_I e^{-i\omega_i t}$, gaining an additional oscillation term. The detuning $\delta = \omega_i - \omega_\mathrm{L}$ is measured between the laser frequency and the ionic transition frequency. This is a result of using the Campbell-Baker-Hausdorff formula on $U^\dagger a U = e^{-i\omega_i a^\dagger a} a e^{i\omega_i a^\dagger a} = a e^{i\omega_i t}$.

The Hamiltonian Equation 3.25 reveals the existence of three distinct transitions in the Lamb-Dicke regime that can be driven by a laser, dependent on the frequency:

- On resonance, $\delta = 0$, the *carrier* transition $|g,n\rangle \leftrightarrow |e,n\rangle$ is driven, with a Rabi frequency of Ω
- For a laser detuning $\delta = \omega_i$ equals the phonon mode frequency of the ion in the trap, the *blue sideband* transition $|g,n\rangle \leftrightarrow |e,n+1\rangle$ is driven, with a Rabi frequency of $\eta\sqrt{n+1}\Omega$
- For a laser detuning $\delta = -\omega_i$ equals the phonon mode frequency of the ion in the trap, the *red sideband* transition $|g,n\rangle \leftrightarrow |e,n-1\rangle$ is driven, with a Rabi frequency of $\eta\sqrt{n}\Omega$

The sidebands thus open up the ability to couple the ion's motional state with its internal structure, and will allow us to create couplings between multiple ions, creating two-ion entangling gates as described in section 3.3.

Finally, we can easily extrapolate these calculations to the three-dimensional case. Each of the three c_i factors describe the harmonic potential for one axis, so we expect to get three trap frequencies. One frequency, ω_ax in axial direction, is dominated by the DC potential created. Two distinct radial trap frequencies ω_rad1 and ω_rad2 in two radial directions are dominated by the RF trapping potential.

3.1.3 Two-Level Ions in a Cavity

In subsection 3.1.2, the two-level system as model of the ion's internal structure is coupled with a quantized harmonic oscillator in the form of the trapping field arising from electrostatics and the pseudopotential, while the light coupling the two levels was described classically. In this subsection, I will instead describe the quantization of the light field as a quantum harmonic oscillator interacting with the two levels. For clarity, the motion of the ion will be neglected.

The approximations made along the way will lead us to the *Jaynes-Cummings Hamiltonian*, which is a good description of the interactions of atoms and light inside a cavity.

A light field, as electromagnetic field, can be described by the vector potential $\boldsymbol{A}$, from which the electrical field and the magnetic field follow as $\boldsymbol{E} = \partial_t \boldsymbol{A}$ and $\boldsymbol{B} = \nabla \times \boldsymbol{A}$. In second quantization and the Heisenberg picture, this vector potential has the convenient form

$$\boldsymbol{A}(r,t) = \frac{E_0}{\omega_c}\left[\boldsymbol{\epsilon}_c f(\boldsymbol{r}) a e^{-i\omega_c t} + \boldsymbol{\epsilon}_c^* f^*(\boldsymbol{r}) a^\dagger e^{i\omega_c t}\right] , \tag{3.26}$$

where we have used the maximum field amplitude E_0, the complex polarization vector $\boldsymbol{\epsilon}_c$, the dimensionless scalar function $f(\boldsymbol{r})$, describing the spatial extent of the potential[2], and the field mode creation and annihilation operators $a^\dagger$ and a. This leads to the electric field

$$\boldsymbol{E}_c = iE_0\left[\boldsymbol{\epsilon}_c f(\boldsymbol{r}) a e^{-i\omega_c t} + \boldsymbol{\epsilon}_c^* f^*(\boldsymbol{r}) a^\dagger e^{i\omega_c t}\right] . \tag{3.27}$$

The function f is normalized so that it has $|f| = 1$ at those points where the field amplitude is maximum. The field normalization E_0 can be shown to be [Har92]

$$E_0 = \sqrt{\frac{\hbar\omega_c}{2\epsilon_0 V}} . \tag{3.28}$$

In the interaction picture, Equation 3.27 transforms to

$$\boldsymbol{E}_c = iE_0\left[\boldsymbol{\epsilon}_c f(\boldsymbol{r}) a_I + \boldsymbol{\epsilon}_c^* f^*(\boldsymbol{r}) {a^\dagger}_I\right] \tag{3.29}$$

and the total Hamiltonian for the atom in a cavity is

$$\begin{aligned} H =& H_i + H_c + H_{ic} \ , \\ =& \frac{\hbar}{2}\omega_i \sigma_z + \hbar\omega_c n + \boldsymbol{D}\cdot\boldsymbol{E}_c \ , \end{aligned} \tag{3.30}$$

with the atomic dipole operator

$$\boldsymbol{D} = M_{ge}(\boldsymbol{\epsilon}_i \sigma^- + \boldsymbol{\epsilon}_i^* \sigma^+) \tag{3.31}$$

featuring the dipole matrix element M_{ge} (see Equation 3.4) and the polarization vector of the ion's transition $\boldsymbol{\epsilon}_i$. Thus, taking the RWA approximation in the

---

[2] f also includes the $e^{i\boldsymbol{k}\cdot\boldsymbol{r}}$ factor of the potential.

second line,

$$\begin{aligned} H_{ic} =& M_{ge}(\boldsymbol{\epsilon}_i\sigma^- + \boldsymbol{\epsilon}_i^*\sigma^+)\cdot E_0(\boldsymbol{\epsilon}_c a + \boldsymbol{\epsilon}_c^* a^\dagger)\ , \\ \overset{\text{RWA}}{=}& -i\hbar\frac{\Omega_0}{2}(a\sigma^+ - a^\dagger\sigma^-)\ , \end{aligned} \tag{3.32}$$

where

$$\Omega_0 = 2\frac{M_{ge}E_0\boldsymbol{\epsilon}_i\cdot\boldsymbol{\epsilon}_c}{\hbar}\ . \tag{3.33}$$

A quick calculation shows that the total excitation number $a^\dagger a+\sigma^+\sigma^-$ commutes with H, and is thus a constant of motion. This turns the system into an effective two-level system for any given total excitation number, with the two states $|g,n+1\rangle$ and $|e,n\rangle$, and an effective coupling constant

$$\Omega_n = \sqrt{n+1}\,\Omega_0 \tag{3.34}$$

increasing with the square of the photon number.

With a cavity detuning from the atomic transition $\Delta = \omega_\mathrm{c} - \omega_i$, the Hamiltonian turns into

$$H = \hbar\omega_\mathrm{c}(n+\frac{1}{2})\mathbb{1} + \frac{\hbar}{2}(\Delta\sigma_z + \Omega_n\sigma_y)\ . \tag{3.35}$$

The eigenstates of this system are, again, mixed states called *dressed states*

$$\begin{aligned} |+,n\rangle =& \cos\left(\frac{\theta_n}{2}\right)|e,n\rangle + i\sin\left(\frac{\theta_n}{2}\right)|g,n+1\rangle\ , \\ |-,n\rangle =& \sin\left(\frac{\theta_n}{2}\right)|e,n\rangle - i\cos\left(\frac{\theta_n}{2}\right)|g,n+1\rangle\ , \end{aligned} \tag{3.36}$$

with eigenvalues

$$E_n^\pm = (n+1/2)\hbar\omega_\mathrm{c} \pm \frac{\hbar}{2}\sqrt{\Delta^2+\Omega_n^2}\ , \tag{3.37}$$

and a *mixing angle*

$$\tan\theta_n = \frac{\Omega_n}{\Delta} \tag{3.38}$$

describing how the two unperturbed states are blended together for the dressed states. For large detuning, the dressing disappears, while for resonance, the two unperturbed states are degenerate.

3.2 Encoding Qubits and Driving Single-Bit Operations

Initialization

The qubit can be initialized in the state $\left|S_{1/2},\downarrow\right\rangle$ with high fidelity (> 0.99) by repeatedly transferring population from $\left|S_{1/2},\uparrow\right\rangle$ to the $\left|D_{5/2}\right\rangle$ state, and quenching the population back into the $S_{1/2}$ state by driving the $D_{5/2} \leftrightarrow P_{3/2}$ transition with a laser field near 854 nm. The population transfer in the first step is done by driving π-pulses on a suitable subtransition $\left|S_{1/2},\uparrow\right\rangle \leftrightarrow \left|D_{5/2},m_D\right\rangle$, see Figure 2.1. The laser pulses are derived from a laser source near 729 nm, stabilized to a linewidth of below 1 kHz. The frequency is controlled using an acousto-optical modulator. The natural linewidth of the $\left|S_{1/2}\right\rangle \leftrightarrow \left|D_{5/2}\right\rangle$ quadrupole transition of $2\pi \times 0.14$ Hz and the narrow laser linewidth allow for selectively driving transitions between different Zeeman sublevels.

Coherent Manipulation of Single Qubits

Based on the preparation in $\left|S_{1/2},m_S\right\rangle$, we can create arbitrary superposition states within $S_{1/2}$ and $D_{5/2}$ manifolds. Coherent rotations of the spin qubit are driven by stimulated Raman transitions with an effective transition rate of

$$\Omega_{\text{eff}} = \frac{G\Omega_1\Omega_2}{\Delta} \,, \tag{3.39}$$

where Ω_i is the respective on-resonance Rabi frequency of each of the two transitions, Δ the detuning from the resonance for both lasers, and $G = cg \cdot \mathcal{P}_{\mathbf{d}}(\boldsymbol{\epsilon})$ combines the Clebsch-Gordan coefficient cg for both transitions with the projections $\mathcal{P}_{\mathbf{d}}(\boldsymbol{\epsilon})$ of the polarization $\boldsymbol{\epsilon}$ of the laser and the cavity field onto the ionic dipole moment $\mathbf{d}$, see Figure 2.7. At a Raman detuning of about $2\pi \times 100$ GHz, π-times of a few microseconds are achieved. Coherent rotations on the optical qubit are driven by a laser near 729 nm as explained for the initialization. Note that the coherent dynamics on the quadrupole transition depends on the motional state of the ions, such that we need to keep the ions in the Lamb-Dicke regime to achieve high-fidelity operations.

By contrast, the rotations driven by radiofrequency or on the stimulated Raman transition are independent of the motional state. An arbitrary spin qubit state can thus be mapped to the $D_{5/2}$ manifold by using a quadrupole-π-pulse for each spin state.

State Readout

Readout of the optical qubit is performed by fluorescence detection on the cycling transition with an EM-CCD camera or a photomulitplier tube (PMT). A bright event corresponds to the $S_{1/2}$ state, and a dark event to the $D_{5/2}$ state. For the spin qubit, it is necessary to *shelve* one of the qubit states, by transferring population from it with a π-pulse on the quadrupole transition. The readout is then analogous to the case of the optical qubit. In both cases, readout fidelities of ≈ 0.995 can be obtained.

Cavity Induced Stimulated Raman Transition

For the interaction between flying and stationary qubit, we can employ a cavity-induced stimulated Raman transition between the $S_{1/2}$ and $D_{5/2}$ states, driven by a laser off-resonant to the cycling transition and the cavity field. In this case, the coupling strength is analogous to Equation 3.39, with the second Raman beam on-resonance coupling strength Ω replaced by g:

$$\Omega^{\mathrm{eff}} = \frac{G\, g\, \Omega_{\mathrm{L}}}{\Delta} \, , \tag{3.40}$$

where Ω_{L} is the on-resonance Rabi frequency of the laser, g the cavity vacuum coupling rate and Δ the laser detuning from the transition resonance. G again combines the Clebsch-Gordan coefficients with the projections of the polarization onto the dipole moments. We estimate, based on the cavity properties (section 5.1) and the available laser power, that effective transition frequencies of $\Omega^{\mathrm{eff}} \approx 1$ MHz are within reach.

3.3 Two-Bit Gate Operations

Entanglement Generation

A two-ion crystal is entangled using a *geometric phase gate*, or, more specifically, the *light shift gate* of Leibfried et al. [Lei03b]. This gate is based on the creation of a forced oscillator Hamiltonian for the ion crystal. A single ion in a driving field is described by the Hamiltonian

$$\widehat{H} = \hbar\omega \left(\hat{\boldsymbol{a}}^\dagger \hat{\boldsymbol{a}} + \frac{1}{2} \right) + \left(f^*(t) x_0 \hat{\boldsymbol{a}} + f(t) x_0 \hat{\boldsymbol{a}}^\dagger \right) \, , \tag{3.41}$$

using the root mean square spatial spread $x_0 = \sqrt{\hbar/(2m\omega)}$ of the ground state wave function, as well as the usual creation and annihilation operators. Con-

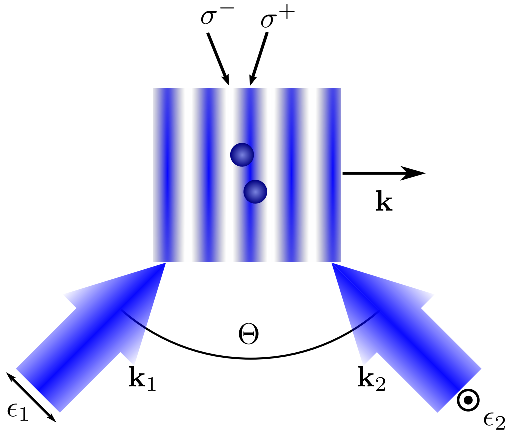

Figure 3.1: Geometric Phase Gate. Two Raman beams are directed into the trap at an angle Θ to each other, with orthogonal linear polarizations $\boldsymbol{\epsilon}_1$ (in plane) and $\boldsymbol{\epsilon}_2$ (out of plane). The superposition of both beams at the location of the ion crystal creates a traveling polarization wave pattern with wave vector $k = k_1 - k_2$.

sidering a force slightly detuned from resonance ω, $\omega \gg \delta$, $f(t) = \hbar\Omega i\, e^{-i(\omega-\delta)}$, where Ω is the force's coupling strength, this translates to an interaction-picture Hamiltonian

$$\widehat{H}_I(t) = \hbar\Omega i \left(\hat{\boldsymbol{a}}\, e^{-i\delta t} + \hat{\boldsymbol{a}}^\dagger e^{i\delta t} \right) \ . \tag{3.42}$$

The driving force provides the system with a time evolution operator equivalent to a time-dependent displacement operator

$$\widehat{D}(\alpha) = e^{\alpha\, \hat{\boldsymbol{a}}^\dagger + \alpha^* \hat{\boldsymbol{a}}} \ , \tag{3.43}$$

$$\alpha(t) = -\frac{i}{\hbar} \int_0^t \Omega e^{i\delta t'} dt' \ , \tag{3.44}$$

which displaces a state in position-momentum phase space without changing its phase space volume. In particular, a ground state wave packet is transformed into a coherent state, displaced in phase space but with minimal phase space volume. For a near-resonant driving force, detuned by δ, the path in phase space for the two qubits is given by

$$\alpha(t) = \frac{\Omega}{\delta} \left(1 - e^{i\delta t} \right) \ , \tag{3.45}$$

a circular trajectory with radius Ω/δ. For any interaction time $\tau = 2\pi N/\delta$, $N \in \mathbb{N}$, a full circle in phase space is traversed, and the ion's motional state returned to the original one.

Extending the interaction Hamiltonian Equation 3.42 to two ions, we wish to create a spin-dependent displacement force, with a resulting Hamiltonian

$$i\hbar\Omega\left(\hat{\boldsymbol{a}}\,e^{-i\delta t} + \hat{\boldsymbol{a}}^{\dagger}e^{i\delta t}\right)\left(\hat{\boldsymbol{\sigma_z}} \otimes \mathbb{1} + \mathbb{1} \otimes \hat{\boldsymbol{\sigma_z}}\right) \ . \tag{3.46}$$

The spin dependency is brought into the system by a beat pattern of two Raman-beams with orthogonal polarizations, see Figure 3.1. The beams both have frequencies ω_i and enter the trap at an angle Θ relative to each other, with linear polarizations that are orthogonal to each other. The resulting wave vector $\boldsymbol{k} = \cos\Theta(\boldsymbol{k}_2 - \boldsymbol{k}_1)$ is perpendicular to the trap axis. This beat pattern changes polarization from σ^- to σ^+ periodically with each wave maximum, with linear polarization in between. Due to the detuning between the two beams, the beat pattern moves, so each ion is treated to the same force after one oscillation $2\pi/\left(\omega_2 - \omega_1\right)$ of the beat. The different light polarizations couple differently to the spins, creating a spin-dependent ("dynamical") Stark shift, and as such a spin dependent force. The spin-independent Stark shift can be tuned to zero by a suitable choice of laser detunings and polarizations. For the fastest gate time $\tau = 2\pi/\delta$, the laser intensities and polarizations, and the gate detuning have to be chosen so that the geometric phase $\phi_0(\tau) = \pi/2$ is just a quarter rotation. The gate then has the following transformation properties:

$$\left|\uparrow\right\rangle\left|\uparrow\right\rangle \to \ \left|\uparrow\right\rangle\left|\uparrow\right\rangle \ , \tag{3.47}$$

$$\left|\uparrow\right\rangle\left|\downarrow\right\rangle \to i\left|\uparrow\right\rangle\left|\downarrow\right\rangle \ , \tag{3.48}$$

$$\left|\downarrow\right\rangle\left|\uparrow\right\rangle \to i\left|\downarrow\right\rangle\left|\uparrow\right\rangle \ , \tag{3.49}$$

$$\left|\downarrow\right\rangle\left|\downarrow\right\rangle \to \ \left|\downarrow\right\rangle\left|\downarrow\right\rangle \ . \tag{3.50}$$

This can either be transformed into a controlled-NOT-gate (CNOT) for universal quantum computation by two single-qubit pulses, or can transform the two qubits into a maximally entangled Bell pair,

$$\left|\Psi\right\rangle = \frac{1}{\sqrt{2}}\left(\left|\uparrow\right\rangle\left|\uparrow\right\rangle + i\left|\downarrow\right\rangle\left|\downarrow\right\rangle\right) \ , \tag{3.51}$$

by adding a π-pulse on both qubits into the middle of the geometric phase gate [Kau17b; Gae16; Bal16].

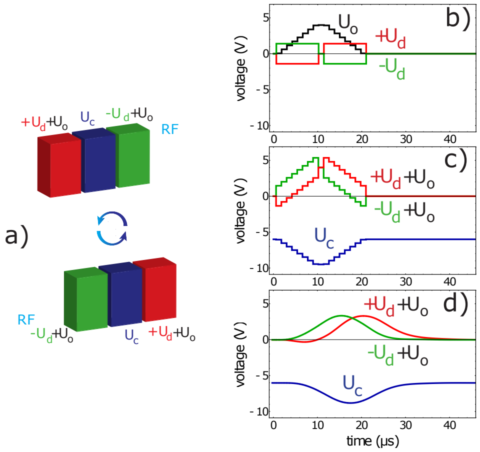

Figure 3.2: Ion swapping in a segmented trap. a) shows the relevant trap electrodes, indicating how the trapping voltage U_c , diagonal voltage U_d and offset voltage U_o controlling the process are applied. Panels b) and c) show the voltage ramps in the form of discrete samples, as they are programmed to the arbitrary waveform generator. Here, b) shows U_d and U_o , while c) shows the actual electrode voltages. Panel d) shows the voltage ramps, measured behind the low-pass filter, which leads to smoothing and delay of the ramps. e) shows the relevant part of the level scheme of ^{40}Ca$^+$. Picture taken from Kaufmann et al. [Kau17a], used with permission.

Ion Crystal Reordering

In a linear ion trap that strives to entangle qubits via next-neighbor interactions, we require the ability to swap entanglement between qubit registers. This SWAP gate can be implemented as a laser-driven gate [Gul03] based on composite pulses. However, with the control over the trap made possible by the MAWG setup, we can instead physically rotate the positions of two ions in a segment potential [Kau17a]. This has the advantage of not requiring a coupling to the internal states of the ions, in contrast to the composite laser pulses, which results in minimal loss of fidelity.

The ions are rotated by applying a diagonal, symmetry-breaking potential to the electrodes neighboring the two-ion-crystal. As shown in Figure 3.2, two diagonally positioned electrodes are offset by $+U_d$ (red), while the other two are offset by $-U_d$ (green). Now, the trapping voltage U_c is decreased, and the neighboring segments are ramped up to a positive voltage U_0. This increases the axial confinement far enough that the lower radial mode is of lower energy, forcing the ion crystal to realign itself along this axis. The diagonal potential is switched off, then reapplied with switched polarity, and U_0 finally ramped back down, so the ion crystal realigns along the axis, but with inverse ordering. Applying this procedure for a total gate time of 42 µs, we achieve excitations of the axial modes of less than 0.05 Phonons per SWAP gate [Kau17a].

3.4 EPR Pair Readout

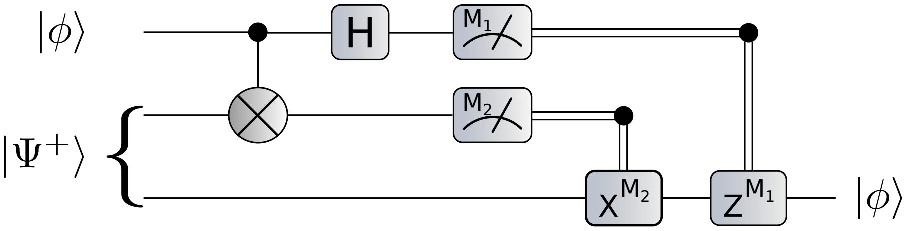

Figure 3.3: Circuit representation of quantum teleportation. The superposition state $\phi = \alpha\,|0\rangle + \beta\,|1\rangle$ is transferred from the initial qubit to the second qubit of a Bell pair. X^{M_2} and Z^{M_1} are conditional rotations performed only if the respective measurement M_i returned $|1\rangle$ as a result.

A central element of quantum teleportation, and thus of most quantum repeater protocols, is the *Bell state measurement*, i.e., the determination which of the four Bell states

$$\begin{aligned}
\Phi^+ &= \frac{1}{\sqrt{2}}\Big(\,|{\downarrow}\rangle\,|{\downarrow}\rangle + |{\uparrow}\rangle\,|{\uparrow}\rangle\,\Big)\ ,\\
\Phi^- &= \frac{1}{\sqrt{2}}\Big(\,|{\downarrow}\rangle\,|{\downarrow}\rangle - |{\uparrow}\rangle\,|{\uparrow}\rangle\,\Big)\ ,\\
\Psi^+ &= \frac{1}{\sqrt{2}}\Big(\,|{\downarrow}\rangle\,|{\uparrow}\rangle + |{\uparrow}\rangle\,|{\downarrow}\rangle\,\Big)\ ,\\
\Psi^- &= \frac{1}{\sqrt{2}}\Big(\,|{\downarrow}\rangle\,|{\uparrow}\rangle - |{\uparrow}\rangle\,|{\downarrow}\rangle\,\Big)
\end{aligned} \tag{3.52}$$

a pair of qubits is in. Since detection methods cannot observe superposition states with a single detection, it is necessary to map the Bell states onto the four product states $|{\downarrow}\rangle\,|{\downarrow}\rangle$, $|{\downarrow}\rangle\,|{\uparrow}\rangle$, $|{\uparrow}\rangle\,|{\downarrow}\rangle$ and $|{\uparrow}\rangle\,|{\uparrow}\rangle$. This map can be achieved by doing a CNOT gate on the two qubits, with the first as control and the second as target qubit, and applying a $\pi/2$ rotation on the control qubit. Subsequent state detection of the two ions removes any additional local phases caused by the rotation, and gives a unique answer to which Bell state the ions were in, within the bounds of state fidelity.

3.5 Entanglement Swapping

A central idea of quantum repeaters is to create entanglement between two qubits at distance L from N entangled pairs of qubits at distances L/N. We thus require the ability to perform heralded entanglement generation to create the base pairs. We will look at a selection of methods to create entangled qubit pairs at a distance in section 4.1. After this chain of base pairs is summoned into existence from the Platonic dungeon dimensions, it is necessary to perform entanglement swapping, to entangle successively further apart qubits, up to the final end pair.

Entanglement swapping was first proposed by Bennett et al. [Ben93] in 1993. The protocol for this thesis was performed by Riebe et al. [Rie08] on $^{40}\mathrm{Ca}^{+}$ ions in a linear Paul trap 15 years later. For two EPR pairs i, j of qubits, each in a state $|\Psi_{ij}\rangle$, with $|\Psi\rangle$ defined as in Equation 3.52, for a total state of

$$|\Psi_{1234}\rangle = \left|\Psi_{12}^{-}\right\rangle \otimes \left|\Psi_{34}^{-}\right\rangle \ . \tag{3.53}$$

This state is rewritten by shuffling the grouping of ions into unentangled pairs 2,3 and 1,4 with the basis states $|\Psi^{\pm}\rangle$ and $|\Phi^{\pm}\rangle$:

$$\begin{aligned} |\Psi_{1234}\rangle = &-\frac{1}{2}\Big(\left|\Phi_{14}^{+}\right\rangle \otimes \left|\Phi_{23}^{+}\right\rangle - \left|\Phi_{14}^{-}\right\rangle \otimes \left|\Phi_{23}^{-}\right\rangle \\ &- \left|\Psi_{14}^{+}\right\rangle \otimes \left|\Psi_{23}^{+}\right\rangle + \left|\Psi_{14}^{-}\right\rangle \otimes \left|\Psi_{23}^{-}\right\rangle \Big) \ . \end{aligned} \tag{3.54}$$

Finally, a Bell-state measurement, as in section 3.4, projects the ion 2 and 3 into an entangled pair $|\Phi^{\pm}\rangle$ or $|\Psi^{\pm}\rangle$ according to Equation 3.54.

3.6 Coherent Light Fields as Continuous Variable Qubits

So far, we have restricted ourselves to discrete quantum variables as qubits, especially for the stationary qubits, but also in the CQED treatment of the flying qubit. One of the entanglement distribution protocols looked at in chapter 4, however, the *hybrid protocol* (subsection 4.1.3), uses continuous variables to distribute entanglement between nodes.

The flying qubit, called *qubus*, is a *coherent state* $|\alpha\rangle$ according to Glauber [Gla63]. They are eigenstates of the annihilation operator a, and in terms of Fock number states, can be expressed as

$$|\alpha\rangle = e^{-|\alpha|^2/2} \sum_n \frac{\alpha^n}{\sqrt{n!}} |n\rangle \ , \tag{3.55}$$

where α is a complex number.

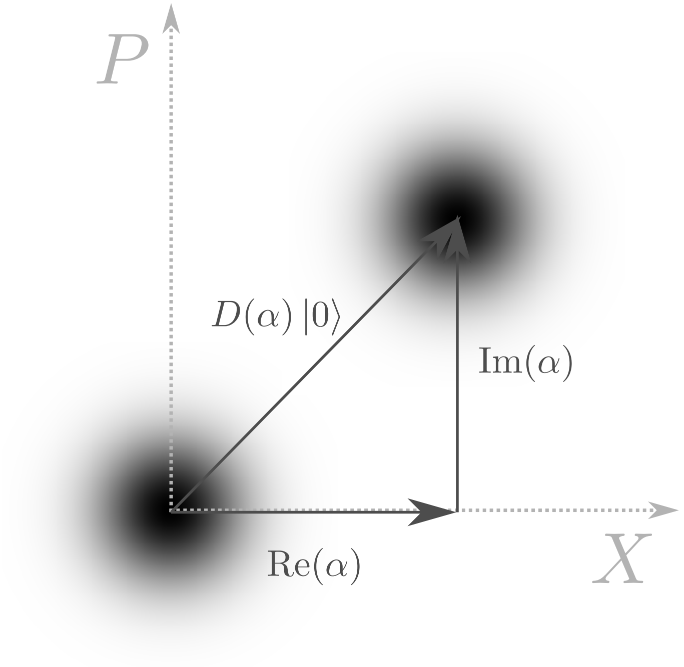

Figure 3.4: Coherent states in phase space spanned by the quadratures X and P (see Equation 3.16). The vacuum state $|0\rangle$ of the oscillator around the coordinate origin is shifted by the operator $D(\alpha)$, keeping its shape in phase space and thus the extent of its uncertainty.

The expectation value for the number of excitations in this state $\langle n\rangle = |\alpha|^2$ is the square modulus of α. The dynamics of classical harmonic oscillators is most closely reproduced in quantum mechanics by coherent states, where the amplitude and phase of α correspond to the amplitude and phase of the classical oscillator. In further correspondence to classical oscillators, coherent states are created by displacing the quantum oscillators rest state, or vacuum state, in phase space,

$$\begin{aligned} |\alpha\rangle =& D(\alpha)\,|0\rangle \ , \\ D(\alpha) =& e^{\alpha a^\dagger + \alpha^* a} \ , \end{aligned} \tag{3.56}$$

with *displacement operator* $D(\alpha)$ corresponding to applying a shift $\mathrm{Re}(\alpha)$ to its position and imparting a kick $\mathrm{Im}(\alpha)$ to its momentum, as shown in Figure 3.4. The phase space in the figure is spanned by the dimensionless operators X and P, the quadratures from Equation 3.16. In our case, the coherent states will be those of the light field, which are well approximated by laser pulses. As we will elaborate in subsection 4.1.3, the quantum information is encoded into the phase of the qubus, which can be entangled with the ion's internal state when it is kept in the cavity.

4 Long Distance Entanglement Distribution Using Ions

This chapter contains the results and conclusions of a paper published during the thesis, *A quantum repeater node with trapped ions: a realistic case example* [Pfi16], which was published in *Applied Physics B*. Phrasing, formatting and links have been adapted to better harmonize with this dissertation.

In this chapter, we will investigate the following entanglement distribution protocols:

- a scheme using *distributed Einstein-Podolski-Rosen-(EPR) states* from a source of entangled photons [Sch13; Llo01]
- two variations of the *Duan-Lukin-Cirac-Zoller-(DLCZ) protocol* [Dua01; Cab99; Sim03]
- a protocol using a combination of discrete and continuous variables dubbed *hybrid protocol* (HP) [Loo06]

The key parameters for the assessment of the protocols are the fidelities F and rates of successful entanglement per second $r_e = P/t_d$, where P is the success probability, and $1/t_d$ the repetition rate. The fidelities and rates of entanglement for all three protocols are inferred using experimentally determined or estimated parameters of the apparatus.

All the protocols have in common that they use photonic flying qubits, although the hybrid protocol is unique in that entanglement is distributed using a continuous variable encoded in a coherent light pulse instead of polarization entangled photons. Furthermore, all protocols feature heralding of entanglement creation.

4.1 Introducing Entanglement Distribution Protocols

4.1.1 Distributed EPR-States Protocol

One of the most prominent schemes proposed for quantum communication through multiple repeater stations is based on the idea of distributing the constituents of an entangled photon pair, e.g., polarization entangled photons from a spontaneous down conversion source. These are transmitted via fibers to neighboring QR nodes (N) and (N+1), c.f. Figure 4.1 a). There, the photon state is mapped onto stationary qubits, giving rise to inter-node entanglement [Llo01]. Building blocks of this scheme have been realized e.g., in Kurz et al. [Kur14] and Schug et al. [Sch14].

For this protocol, the stationary qubits are initially prepared in a superposition state, $|\Psi_i\rangle_q = |0_i\rangle + |1_i\rangle$. Throughout the paper, we omit the normalization of wavefunctions, unless the normalization factor is of specific interest. A polarization-entangled photon pair in the state $|\Psi\rangle_p$ interacting with the stationary qubit couples both states $|0_i\rangle$ and $|1_i\rangle$, depending on its polarization, to levels of a short lived, excited state, $|0_e\rangle$ and $|1_e\rangle$:

$$\begin{aligned} |\Psi_i\rangle_q^{\otimes 2} \otimes |\Psi\rangle_p =& (|0_i\rangle + |1_i\rangle)^{\otimes 2} \big(|\sigma^+,\sigma^-\rangle + |\sigma^-,\sigma^+\rangle \big) \\ \xrightarrow{\text{abs.}}& |0_e,1_e\rangle + |1_e,0_e\rangle \\ &+ \big(|0_e,0_i\rangle + |0_i,0_e\rangle \big) |\sigma^-\rangle \\ &+ \big(|1_e,1_i\rangle + |1_i,1_e\rangle \big) |\sigma^+\rangle \\ &+ |0_i,1_i\rangle |\sigma^-,\sigma^+\rangle + |1_i,0_i\rangle |\sigma^-,\sigma^+\rangle \ . \end{aligned} \tag{4.1}$$

The excited states decay into long-lived states, $|0_f\rangle$ and $|1_f\rangle$, leaving an entangled final state upon two-photon emission:

$$|\Psi_f\rangle_q = \big(|0_f,1_f\rangle + |1_f,0_f\rangle \big) \ . \tag{4.2}$$

This decay provides access to herald photons via the spontaneous emission. Both the initial states and the herald detection basis have to be chosen such that the decay via the distinct channels $|0_e\rangle \to |0_f\rangle$ and $|1_e\rangle \to |1_f\rangle$ is guaranteed. At the same time, the availability of which-path-information has to be prevented for preserving entanglement.

Due to a low absorption efficiency, in most cases either only one or zero photons of an EPR pair interact at a node. We are interested in the probability of a single-photon-interaction taking place at either node within time t, after an initialized stationary qubit is exposed to the EPR source, which is given by

$$P_1(t) = 1 - e^{-r_1 \cdot t} \ . \tag{4.3}$$

The rate of single herald photon emission events

$$r_1 = r_{\mathrm{EPR}} \cdot \eta \tag{4.4}$$

depends on the brightness of the EPR source, r_{EPR}, and the probability η of a photon from the EPR source to be injected into a cavity at a node and to interact with the stationary qubit.

The probability density for both photons of one EPR pair to interact each with its stationary qubit at time t, while *no* single-photon-interaction at neither node has happened previously, is

$$p_2(t) = r_2\, e^{-r_2 \cdot t}\, (1 - P_1(t))^2 = r_2\, e^{-(r_2 + 2\, r_1) \cdot t} \ . \tag{4.5}$$

The rate of *both* photons from one EPR pair interacting with their respective stationary qubit is given by

$$r_2 = r_{\mathrm{EPR}} \cdot \eta^2 \ . \tag{4.6}$$

In Equation 4.5 we explicitly exclude a single photon event taking place during time t, since such an event would change the state of a stationary qubit and thwart any two-photon event. Integrating Equation 4.5 over t, we find the total probability of a successful two-photon mapping within time t after initialization to be

$$P_2(t) = \int_0^t p_2(\tau) d\tau = \frac{r_2}{r_2 + 2\, r_1} \left(1 - e^{-(r_2 + 2 r_1) \cdot t}\right) \ . \tag{4.7}$$

The emitted heralds are detected at a probability P_{det}, leading to a success probability for one experimental run of

$$P_e(t) = P_{\mathrm{det}}^2 P_2(t) \ . \tag{4.8}$$

Thus, the entanglement generation rate of stationary qubits at neighboring QR nodes is given by

$$r_e = \frac{P_e(\tau_W)}{\tau_W + \tau_{\mathrm{prep}}} \ , \tag{4.9}$$

where $\tau_W \approx \frac{1}{2 r_1}$ is the detection window for coincident herald photons. After expiry of τ_W without coincident herald detection, the stationary qubits at both nodes are re-initialized, which takes the time τ_{prep}. Thus, for fixed r_1 and τ_{prep}, τ_W can be chosen to provide an optimum entanglement rate.

4.1.2 The DLCZ Protocol

This repeater protocol entangles stationary qubits at different repeater nodes by probabilistically creating a stationary qubit-photon pair in either of the nodes (N) and (N+1), see Figure 4.1 b). A detection registering the arrival of one photon, but unable to distinguish the source node, projects the stationary

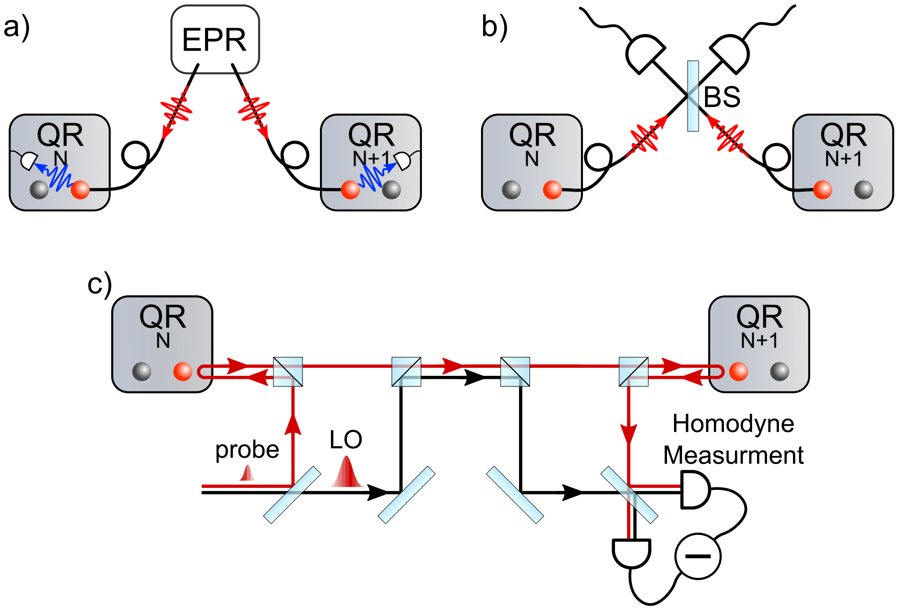

Figure 4.1: Basic principle for distant entanglement generation for the three protocols investigated. Stationary qubits with shared entanglement are indicated as red balls.
a) Distributed EPR-states protocol. An entangled photon pair (red waves) is generated by an EPR source and sent to two adjacent repeater nodes. The quantum state of the photons is then mapped on a stationary qubit at each node, leaving one qubit at each node entangled with each other after detection of the herald photon (blue).
b) DLCZ protocol. A local operation at each repeater node probabilistically generates a photon in either of the nodes. Interfering the possible photon paths on a beam splitter (BS) before detection entangles the qubits.
c) Continuous variables hybrid protocol, adapted from van Loock et al. [Loo06]. A coherent light pulse is split into a weak probe pulse (qubus) and a strong local oscillator (LO). The qubus interacts dispersively with the stationary qubit, resulting in a state dependent phase shift of the qubus. After transferring the qubus via the optical channel, the same operation is performed at the second repeater station. Measurement of the qubus phase leaves the system in an non-maximally entangled Bell state, for a correct detection pattern.

qubits at the two nodes into a Bell state.

The stationary qubits are initialized in a state $|q_0\rangle$. A laser beam then drives a cavity-induced stimulated Raman transition [Stu12] via the excited state $|q_e\rangle$ to a stable, final state $|q_1\rangle$. The quantum state of the stationary qubit and the cavity mode at one node evolves as

$$|q_0\rangle\,|0_c\rangle \xrightarrow{\text{Raman}} |q_0\rangle\,|0_c\rangle + \sqrt{p_1}\,|q_1\rangle\,|1_c\rangle \ . \tag{4.10}$$

Here, $|n_c\rangle$ is the n-photon Fock state of the cavity mode.

The entanglement between neighboring nodes is achieved by a *single-photon detection scheme* [Cab99]. Driving the Raman transition such that the transition probability fulfills $p_1 \ll 1$, the state evolution in both nodes is

$$(|q_0\rangle\,|0_c\rangle)^{\otimes 2} \rightarrow |q_0, q_1\rangle\,|0_c{,}1_c\rangle + |q_1{,}q_0\rangle\,|1_c{,}0_c\rangle \ , \tag{4.11}$$

where we have omitted the parts of the final wave function where either no or two photons are emitted. The emitted photons are transmitted to a detection setup, where a 50/50 beamsplitter in front of two detectors erases which-path information, see Figure 4.1 b). This scheme results in the two-qubit wave function

$$\big(\,|q_1{,}q_0\rangle + |q_0{,}q_1\rangle\,\big)\,|A\rangle + \big(\,|q_1{,}q_0\rangle - |q_0{,}q_1\rangle\,\big)\,|B\rangle \ , \tag{4.12}$$

where either detector A or B registers a photon.

The success probability of this entanglement creation, with single-photon emission probability p_1 and probability to detect the emitted photon P_{det}, is given by [Zip08]

$$P_1 = 2\,P_{\text{det}}\,p_1\,(1 - P_{\text{det}}\,p_1) \ . \tag{4.13}$$

The two-photon emission process omitted in Equation 4.10 leads to an infidelity of entanglement generation. Therefore, p_1 has to be chosen sufficiently small in order to reach a given threshold fidelity F_{thr},

$$p_1 \leq \frac{1 - F_{\text{thr}}}{1 - P_{\text{det}} F_{\text{thr}}} \ . \tag{4.14}$$

The entanglement generation rate r_e with success rate P_1 can be obtained by dividing P_1 by the required time per experimental run τ_{run}:

$$r_e = \frac{P_1}{\tau_{\text{run}}} \ . \tag{4.15}$$

4.1.3 Continuous Variables Hybrid Protocol

The two previous protocols operate on discrete variables, both for the flying and the stationary qubits. In contrast, the hybrid protocol [Loo06; Lad06; Loo08] employs continuous variables for encoding photonic quantum information, while retaining the discrete stationary qubit, see Figure 4.1 c).

The continuous variable is embodied by a coherent light pulse, the *qubus* (see section 3.6). The stationary qubits are initially prepared in a superposition state $|\Psi_i\rangle = |0\rangle + |1\rangle$, and interact with the qubus, which is injected into a cavity, to enhance the interaction. The cavity field off-resonantly drives the transition $|1\rangle \leftrightarrow |e\rangle$ to an auxiliary excited state. The detuning Δ from this transition is much larger than the vacuum Rabi splitting, $\Delta \gg 2g$, such that the interaction is *dispersive*. The state of the stationary qubit is imprinted into the phase of the qubus state $|\alpha\rangle$. The Hamiltonian pertaining to this regime is given by

$$\hat{\boldsymbol{H}}_{\text{int}} = \hbar \frac{g^2}{\Delta} \hat{\boldsymbol{\sigma}}_z \hat{\boldsymbol{a}}^\dagger \hat{\boldsymbol{a}} \ . \tag{4.16}$$

The operator $\hat{\boldsymbol{a}}^\dagger$ ($\hat{\boldsymbol{a}}$) is the creation (annihilation) operator of the field mode, and $\hat{\boldsymbol{\sigma}}_z = |0\rangle\langle 0| - |1\rangle\langle 1|$ is the Pauli z-operator. This Hamiltonian describes an energy shift dependent on the state of the stationary qubit. The evolution operator of this Hamiltonian is

$$\hat{\boldsymbol{U}}_{\text{int}} = \exp\left(-i\frac{\theta}{2} \hat{\boldsymbol{\sigma}}_z \hat{\boldsymbol{a}}^\dagger \hat{\boldsymbol{a}} \right) , \tag{4.17}$$

with a phase shift

$$\theta = \frac{2\,g^2}{\Delta}\,\tau_\kappa \ , \tag{4.18}$$

where τ_κ is the interaction time in the cavity. For a coherent state in the cavity, this leads to the following evolution of a superposition state of the stationary qubit:

$$\hat{\boldsymbol{U}}_{\text{int}}\big(|0\rangle + |1\rangle \big) |\alpha\rangle = |0\rangle \left|\alpha e^{-i\theta/2}\right\rangle + |1\rangle \left|\alpha e^{i\theta/2}\right\rangle \ . \tag{4.19}$$

Neglecting losses, the interaction of the qubus with two stationary qubits in neighboring QR nodes leads to the state [Loo06; Loo08]

$$|\Psi\rangle = \left|\psi^+\right\rangle |\alpha\rangle + |00\rangle \left|\alpha e^{-i\theta}\right\rangle + |11\rangle \left|\alpha e^{i\theta}\right\rangle \ . \tag{4.20}$$

A measurement determining the phase of the qubus projects the state into either one of the three components. The Bell state $|\psi^+\rangle$ is generated in the QR nodes if no phase shift is detected.

We thus require that the *distinguishability*

$$d = \alpha \sin\theta \tag{4.21}$$

of the phase shifted states is sufficiently large to separate the coherent states in phase space [Loo06].

While a large amplitude of $|\alpha\rangle$ will guarantee a high distinguishability, it also leads to decoherence when losses in the transmission of the qubus are taken into account. One thus faces a trade off between fidelity and efficiency. Taking losses into account, we introduce a total transmission η from the cavity in QR (N) to the cavity in QR (N+1), so that on average $(1-\eta)|\alpha|^2$ photons will be lost to the environment while the qubus propagates between neighboring nodes. Following [Loo08], we define the coherence parameter

$$\mu^2 = \frac{1}{2}\big(1 + e^{-(1-\eta)\alpha^2(1-\cos\theta)}\big) \ . \tag{4.22}$$

The initial pure state evolves to a mixed state, after a local operation on each qubit, with a density matrix

$$|\Psi\rangle\langle\Psi| = \mu^2 \left|\Psi^+\right\rangle\left\langle\Psi^+\right| + (1-\mu^2)\left|\Psi^-\right\rangle\left\langle\Psi^-\right| \ , \tag{4.23}$$

where

$$\begin{aligned}\left|\Psi^\pm\right\rangle =& \frac{1}{\sqrt{2}}\left|\sqrt{\eta}\alpha\right\rangle\left|\psi^\pm\right\rangle \pm \frac{1}{2}e^{-i\eta\xi}\left|\sqrt{\eta}\alpha e^{i\theta}\right\rangle|11\rangle \\ &+ \frac{1}{2}e^{i\eta\xi}\left|\sqrt{\eta}\alpha e^{-i\theta}\right\rangle|00\rangle \ .\end{aligned} \tag{4.24}$$

The relative phase ξ is of no further significance for our discussion. Projecting the wave function of the qubus to the non-phase-shifted part at detection selects the maximally entangled Bell states $|\psi^\pm\rangle = |10\rangle \pm |01\rangle$. A high distinguishability implies reliable identification of the Bell states, but mixes the two pure states $|\Psi^\pm\rangle$, whereas for low distinguishability, a pure state $|\Psi^+\rangle$ is dominant, at the price of reduced success when identifying the Bell state $|\psi^+\rangle$.

In order to collapse the wave function to the required part, it is necessary to identify the phase of a coherent state $|\alpha\rangle$. One possibility is *p-homodyne detection*, which requires a setup as depicted in Figure 4.1 c). In this setup, the reference signal for homodyning is created by splitting a coherent pulse into the weak qubus signal and a local oscillator (LO) phase reference pulse, which does not interact with the cavities. The p-homodyne measurement amounts to a projection of the qubus state onto the p-quadrature of phase space. Following [Lad06], for an acceptance window $-p_c < p < p_c$, we can assign a probability P_S of a 'non-phase-shifted' detection event and a fidelity F of the resulting state,

$$\begin{aligned} P_S =& \frac{1}{4}\Big(2\,\mathrm{erf}\left(\sqrt{2}p_c\right) + \mathrm{erf}\left(\sqrt{2}(p_c+\eta d)\right) \\ &+ \mathrm{erf}\left(\sqrt{2}(p_c-\eta d)\right)\Big)\ , \end{aligned} \tag{4.25}$$

$$\begin{aligned} F =& \langle\psi^+|\,\rho\,|\psi^+\rangle \\ =& \frac{1}{4P_S}\left(1+e^{-d^2(1-\eta^2)/2}\right)\mathrm{erf}\left(\sqrt{2}p_c\right)\ . \end{aligned} \tag{4.26}$$

In each of the presented protocols, a Bell state is generated first between nodes QR (N) and QR (N+1), and then between QR (N) and QR (N−1) in the network (Figure 1.1 a). Entanglement swapping [Ben93; Rie08] then creates Bell states in nodes QR (N−1) and QR (N+1), which have twice the distance (Figure 1.1 b). The repeated application of entanglement swapping finally leads to entanglement between the end nodes Alice and Bob.

4.1.4 Unambiguous State Discrimination

Unambiguous State Discrimination (USD) [Dus00; Loo08] is an alternative to homodyne detection, where the measurement is set up so that the possible results are {*definitely entangled, definitely unentangled, unknown*}, ruling out the possibility of bit-flip errors. The scheme introduced here is based on van Loock [Loo08], and is derived in detail there.

We are interested in unambiguously identifying the non-phase-shifted part of Equation 4.24, which projects the qubits onto the mixed Bell state $\mu\,|\psi^+\rangle + \sqrt{1-\mu^2}\,|\psi^-\rangle$. Figure 4.2 shows the detection setup, with an input port for the qubus (the remaining input port is depicted with the vacuum mode), and two output ports to detectors A and B. The first beamsplitter changes an incoming coherent state $|\beta\rangle$ to

$$|\beta{,}0\rangle \rightarrow \left|\frac{1}{\sqrt{2}}\beta,\frac{i}{\sqrt{2}}\beta\right\rangle\ . \tag{4.27}$$

The other two beamsplitters are used to displace the two resulting coherent pulses in phase space by sending phase-shifted coherent pulses $|\alpha_A\rangle$ and $|\alpha_B\rangle$,

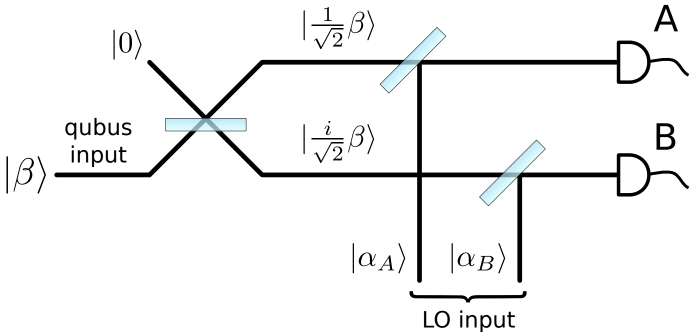

Figure 4.2: Unambiguous state discrimination setup. The incoming qubus $|\beta\rangle$, consisting of the superposition of the three coherent states $|\alpha\rangle$, $\left|\alpha e^{i\theta}\right\rangle$, and $\left|\alpha e^{-i\theta}\right\rangle$, is transformed by a 50/50 beamsplitter into the two output pulses $\left|\frac{1}{\sqrt{2}}\beta,\frac{i}{\sqrt{2}}\beta\right\rangle$. For each output pulse, at another 50/50 beamsplitter, a coherent pulse $\left|\alpha_{\{A/B\}}\right\rangle$ outcoupled from the LO creates a displacement in phase space.

outcoupled from the LO, into their respective input ports:

$$\begin{aligned} &\hat{\boldsymbol{D}}_A(\alpha_A)\otimes\hat{\boldsymbol{D}}_B(\alpha_B) \\ &= \hat{\boldsymbol{D}}_A(-\frac{1}{\sqrt{2}}\sqrt{\eta}\alpha e^{i\theta})\otimes\hat{\boldsymbol{D}}_B(-\frac{1}{\sqrt{2}}\sqrt{\eta}\alpha e^{-i\theta})\ . \end{aligned} \tag{4.28}$$

The displacements are chosen such that for the two phase shifted parts of the wave function $\left|\sqrt{\eta}\alpha e^{\pm i\theta}\right\rangle$ as input pulse $|\beta\rangle$, one of the detection ports is always in the vacuum mode (see Figure 4.3). This can be seen by applying these transformations to the three different qubus input states from Equation 4.24:

$$\begin{aligned} |\sqrt{\eta}\alpha{,}0\rangle &\rightarrow \left|\frac{1}{\sqrt{2}}\sqrt{\eta}\alpha(1-e^{i\theta}),\frac{1}{\sqrt{2}}\sqrt{\eta}\alpha(1-e^{-i\theta})\right\rangle\ , \\ \left|\sqrt{\eta}\alpha e^{i\theta}{,}0\right\rangle &\rightarrow \left|0{,}\frac{1}{\sqrt{2}}\sqrt{\eta}\alpha 2i\sin\theta\right\rangle\ , \\ \left|\sqrt{\eta}\alpha e^{-i\theta}{,}0\right\rangle &\rightarrow \left|-\frac{1}{\sqrt{2}}\sqrt{\eta}\alpha 2i\sin\theta{,}0\right\rangle\ . \end{aligned} \tag{4.29}$$

Of the 4 possible detector click patterns, only both detectors firing in coincidence definitely identifies the entangled part of Equation 4.23.

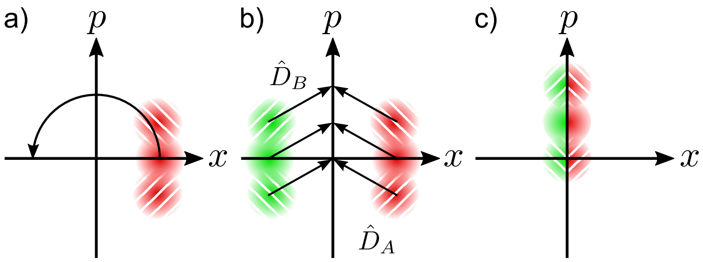

Figure 4.3: Effect of the USD setup on the qubus in phase space. a) The qubus, in the incoming port, is in a superposition of $|\alpha\rangle$ (solid), $\left|\alpha e^{i\theta}\right\rangle$ (shaded upper left to lower right), and $\left|\alpha e^{-i\theta}\right\rangle$ (shaded lower left to upper right). b) Behind the first beamsplitter output port A (red) leaves the states unchanged except for the amplitude (not shown), and output port B (green) rotates the states by π. The displacement pulses $\hat{\boldsymbol{D}}_A$ and $\hat{\boldsymbol{D}}_B$ shift the coherent states in phase space such that in each output port, one of the phase shifted states is displaced onto $|0\rangle$. c) A detection event incompatible with $|0\rangle$ in both detectors A and B is only possible for $|\alpha\rangle$.

The success probability for this event is given by

$$P_\mathrm{e} = \frac{1}{2}\left(1 - e^{-\eta\alpha^2(1-\cos\theta)}\right)^2 , \tag{4.30}$$

with a fidelity of the final state

$$F = \left\langle\psi^+\right| \rho \left|\psi^+\right\rangle = \mu^2 . \tag{4.31}$$

Note that P_e already includes the effect of the USD setup, e.g., the signal reduction by the first beamsplitter of Figure 4.2. It was assumed that the signal remains strong enough to be clearly discerned from the vacuum state, which should be easily attainable with modern detectors and a moderate pulse amplitude α. The final repetition rate of entanglement distribution is given by

$$r_e = \frac{P_e}{\tau_\mathrm{run}} , \tag{4.32}$$

for a time per experimental run τ_run.

4.2 Calculations for the Protocols on the given Experimental Setup

In this section we investigate how the different repeater protocols can be implemented on our hardware platform. We specify the experimental requirements and derive possible experimental sequences. For each protocol, we quantitatively estimate the attainable fidelities and entanglement generation rates for spatially separated Bell states at QR (N) and QR (N+1). Figure 4.4 depicts the experimental sequence at QR (N) in the chain of repeater nodes (see Figure 1.1). The neighboring QRs have an analogous sequence.

All protocols have similar initialization sequences in the beginning and entanglement swapping sequences in the end, see section 3.2 and section 3.3. The duration of the entire protocol run in combination with the success probability determines the entanglement generation rate of the protocol. The time necessary to run one entangling sequence, from initialization to entanglement of a local ion with a distant one, is called τ_{run}, and is split into a preparation time τ_{prep}, and τ_e. The latter is the time each protocol requires to entangle the two distant ions, once they are initialized and have entered the cavity. The time $\tau_{\text{prep}} \approx 210\,\mu\text{s}$ includes the initialization of the ion state $\tau_{\text{init}} \approx 10\,\mu\text{s}$, the shuttling of the ion into the cavity $\tau_S \approx 100\,\mu\text{s}$, as well as the shuttling back to the processor region to be re-initialized if the protocol does not succeed, which again takes the time τ_S. It does not include the post-processing of the ions necessary after the successful entanglement has been heralded. Errors *before* the herald detection decrease the success probability, whereas errors obtained *after* the herald detection reduce the fidelity F.

4.2.1 The EPR Protocol

To implement the EPR protocol in our apparatus, we finish the initialization process from section 3.2 by creating a superposition between the states $\left|D_{5/2}, -3/2\right\rangle$ and $\left|D_{5/2}, +3/2\right\rangle$, in the following denoted as $|D_1\rangle$ and $|D_2\rangle$, using suitable pulses on the $S \leftrightarrow D$ quadrupole transition (see Figure 4.5).

We thus choose the starting state of each stationary qubit as (Figure 4.5 (i))

$$|\Psi_D(t)\rangle = |D_1\rangle + e^{i\phi_D(t)}\,|D_2\rangle \ , \tag{4.33}$$

with the phase

$$\phi_D(t) = (\Delta m_D g_D - \Delta m_S g_S)\frac{\mu_B}{\hbar}Bt + \phi_0 \ . \tag{4.34}$$

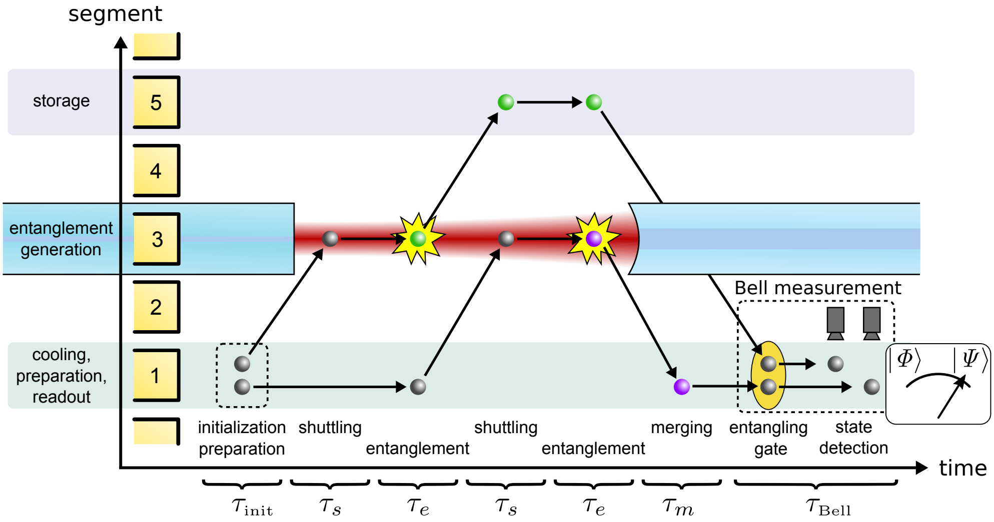

Figure 4.4: Experimental sequence for a basic quantum repeating operation with the presented setup. The trap axis is divided into three regions with different purposes: ions are shuttled into the region around segment 1 for cooling, state preparation, state manipulation, and state readout. The ions are shuttled into the region around electrode 3, into the fiber cavity, for entanglement generation. The region around electrode 5 serves as a short-term storage. After cooling and initializing both (unentangled, grey) ions, one is shuttled into the cavity where entanglement with a qubit from QR (N−1) is generated by either of the three protocols (entanglement indicated by color), see subsection 4.2.1-4.2.3. After shuttling the first ion to the short-time storage, the second ion is shuttled into the cavity and the same operation is performed with a qubit from QR (N+1). This requires a fiber switch in front of the single mode fiber (left), see section 2.4. The ions are then shuttled back to segment 1, a two-ion crystal is formed and a Bell state measurement is performed.

The Δm_i are the differences of the magnetic quantum numbers of the respective manifold, the g_i are their Landé factors, μ_B is the Bohr magneton, and ϕ_0 the phase offset at initialization.

After transporting the ion into the cavity, an EPR source between QR (N) and QR (N+1) provides the polarization entangled photon pairs as flying qubits for this repeater protocol, producing the state

$$|\Psi_{\mathrm{EPR}}\rangle = |L\rangle\,|R\rangle + |R\rangle\,|L\rangle \ , \tag{4.35}$$

with left-handed (L) and right-handed (R) circularly polarized light. To ensure that the frequency and linewidth of the photon match the $D_{5/2} \leftrightarrow P_{3/2}$ transition close to 854 nm, one uses a Single Parametric Downconversion (SPDC) source with a filter cavity [Sch10]. The production rate of entangled photon pairs after cavity filtering is denoted r_{EPR}.

The photons are coupled into the fibers whose ends constitute the cavities of QR (N) and QR (N+1) with an efficiency η_{FC}, and from there into the cavities with an incoupling efficiency between fiber and cavity η_{dip}. A photon successfully injected into the cavity of the node interacts with the ion (Figure 4.5 (ii)) with a probability P_{int}, giving rise to the following state evolution:

$$\begin{aligned} & |\Psi_D\rangle \times |\Psi_{\mathrm{EPR}}\rangle \\ \xrightarrow{abs.}\, & |P_1\rangle + e^{i\phi_D}\,|P_2\rangle \\ \xrightarrow{em.}\, & \big(\,|S_1\rangle + e^{i\phi_D}\,|S_2\rangle\,\big)\,|\pi_{393}\rangle \ . \end{aligned} \tag{4.36}$$

ϕ_D is taken from Equation 4.34, at the time t when the ion absorbs the photon and decays into S.

In case of success, the interaction maps the state of one photon onto the two Zeeman sublevels of the ion's $S_{1/2}$ state, under creation of a π-polarized herald photon at a wavelength near 393 nm (Figure 4.5 (iii)), detected with probability P_{det}. A detection event in each node's herald detector, within a detection window τ_c of each other, denotes a successful entanglement of ions in QR (N) and QR (N+1), after which the ion is moved out of the fiber cavity, and the second ion is entangled with an ion at QR (N−1).

We assume that the rate of EPR photon pairs resonant with the $D_{5/2} \leftrightarrow P_{3/2}$ transition is $r_{\mathrm{EPR}} = 7800\,\mathrm{s}^{-1}$ [Huw13] behind the filter cavity. Throughout this section, it is assumed that only one photon ever populates the cavity mode at the same time. This approximation breaks down as soon as the cavity population decay rate $2\,\kappa$ is no longer considerably greater than the EPR arrival

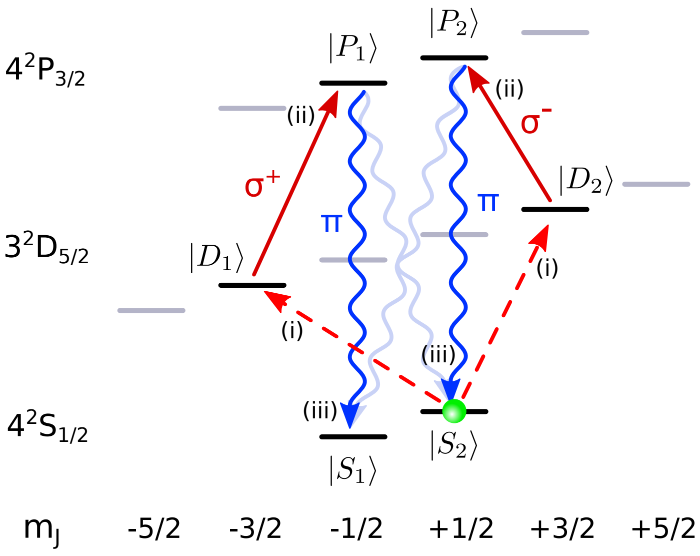

Figure 4.5: Level scheme of a ^{40}Ca$^+$-ion with relevant transitions for the distributed EPR protocol. Lower case Roman numerals indicate protocol steps. (i) After cooling and pumping to the $|S_2\rangle$ state, the ion is initialized in a superposition of $|D_1\rangle$ and $|D_2\rangle$ (dashed red arrows). (ii) In the cavity, the entangled photon induces a transition to one of the $|P\rangle$-states, depending on its polarization, σ^+ or σ^- (dark red arrows). (iii) The ion quickly decays into one of the $|S\rangle$-states under emission of a photon at 393 nm as herald. By filtering out circular polarizations (faint blue waves), only the events which preserve the information (solid blue waves) are detected.

rate at a single cavity, $\kappa \ggg r_{\text{EPR}}\, \eta_{FC}\, \varepsilon$. With $\kappa = 2\pi \times 18.3\,\text{MHz}$, such rates of EPR pair production are beyond current technological proficiency, and our approximation holds.

Solving the Liouville master equation for our setup, including all sublevels of the S, P and D states, with cavity parameters as given in section 5.1, returns the interaction probability of $P_{\text{int}} = 0.047$. Required is a Zeeman splitting less than the cavity bandwidth $2\,\kappa$, thus limiting the magnetic field to $B < 11\,\text{G}$ in order to ensure that the cavity field drives the transitions $D_1 \rightarrow P_1$ and $D_2 \rightarrow P_2$ at similar rates.

The η in Equation 4.4 and Equation 4.6, the probability of one of the photons behind the filter cavity to interact with one ion, is given by

$$\begin{aligned} \eta = \eta_{FC}\, \eta_{\text{in}}\, P_{\text{int}} &\approx 0.005 \\ \eta^2 &\approx 3 \times 10^{-5} \ . \end{aligned} \tag{4.37}$$

Here, $\eta_{FC} \approx 0.9$ is the efficiency of coupling the photons into the fiber after the filter cavity, and $\eta_{\text{in}} = \eta_{\text{out}} = 0.13$ is the probability of coupling a single photon into the cavity, by time-reversal symmetry to the outcoupling process. The detection probability

$$P_{\text{det}} = \frac{d\Omega}{4\pi}\, \eta_{QE}^{397} = 0.007 \tag{4.38}$$

depends of the solid angle of our detection lens $d\Omega/4\pi$, and the quantum efficiency η_{QE}^{397} of the PMT for UV light (section 2.3).

Entanglement generation Rate: With these efficiencies, the entanglement generation rate, Equation 4.9, becomes

$$r_e(\tau_W) = \frac{P_e(\tau_W)}{\tau_{\text{prep}} + \tau_W} \tag{4.39}$$

for a given time to wait on an entanglement event τ_W. We have yet to account for dark counts on the detectors, which both increase the apparent rate of successful events and decrease the fidelity of our final state. A typical dark count rate for UV detectors can be assumed to be $r_{\text{dc}} = 60\,\text{s}^{-1}$ [Kur15]. For a detection window τ_c, during which detector events are counted as concurrent, the probability of registering two simultaneous dark counts is given by

$$P_{2dc}(t,\tau_c) = (1 - e^{-r_{\text{dc}} t}) \cdot (1 - e^{-r_{\text{dc}} \tau_c}) \ . \tag{4.40}$$

Similarly, a photon-qubit interaction in one of the nodes can be concurrent with a dark count in the other, with a probability of

$$P_{hdc}(t,\tau_c) = P_{\text{det}} P_1(t) \cdot (1 - e^{-r_{\text{dc}}\tau_c}) \ , \tag{4.41}$$

with $P_1(t)$ from Equation 4.3 in subsection 4.1.1.

The probability $P'_e(t,\tau_c)$ of any two-detector event, true or false positive, happening during time t, where the window for coincidence detection is set to τ_c, is given by

$$P'_e(t,\tau_c) = P_e(t) + P_{2dc}(t,\tau_c) + P_{hdc}(t,\tau_c) \tag{4.42}$$

$$\Rightarrow r'_e = \frac{P'_e(t,\tau_c)}{\tau_{\text{prep}} + \tau_W + \tau_c} \ . \tag{4.43}$$

We set $\tau_W = r_1^{-1} \approx 15\,\text{ms}$ (see Equation 4.4) to the time by which we can expect one of the photons to have interacted with an ion, making a new initialization necessary. Using $\tau_{\text{prep}} \approx 210\,\mu\text{s}$ (see the beginning of this section), and $\tau_c = \frac{1}{20\kappa}$, the repetition rate becomes $r_e(\tau_W) = 6.4 \times 10^{-6}$. Inserting the values of the setup, this culminates in a rate $r'_e \approx 7.4 \times 10^{-6}\,\text{s}^{-1}$, i.e., about one event every 35 hours. We see that a highly efficient detection of herald photons at 397 nm, together with an effective in-coupling of EPR photons into the cavity, is required to improve this rate.

Fidelity: The fidelity of the final state is limited by the ratio of real entanglement events to total heralded events, $F = r_e/r'_e \approx 0.86$. Another fidelity error is the imperfect filtering of σ-light for detection optics that is not pointlike in extent. For a solid angle of $d\Omega = 4\pi \cdot 0.035$ of the collecting lens, the opening angle is $\theta = 21°$. However, integrating the arriving herald wave function over this area shows the amount of σ-light in the wrong mode to be negligible.

Finally, imperfect initialization and readout (section 3.2) reduce the fidelity to $F \approx 0.86 \times 0.995$ for the EPR protocol.

4.2.2 The DLCZ Protocol

The implementation of the DLCZ protocol in our apparatus, depicted in Figure 4.6, starts with initializing the ion in the state

$$|S\rangle = |S_{1/2}, -1/2\rangle \ . \tag{4.44}$$

After transport of the ion into the cavity, a photon is created by a cavity-induced stimulated Raman transition (section 3.2) between the $S_{1/2}$ and the $D_{5/2}$ manifolds, with $|0\rangle = |D\rangle$ and $|1\rangle = |S\rangle$ chosen as shown in Figure 4.6.

The photon is emitted into the cavity with a probability p_1, which is con-

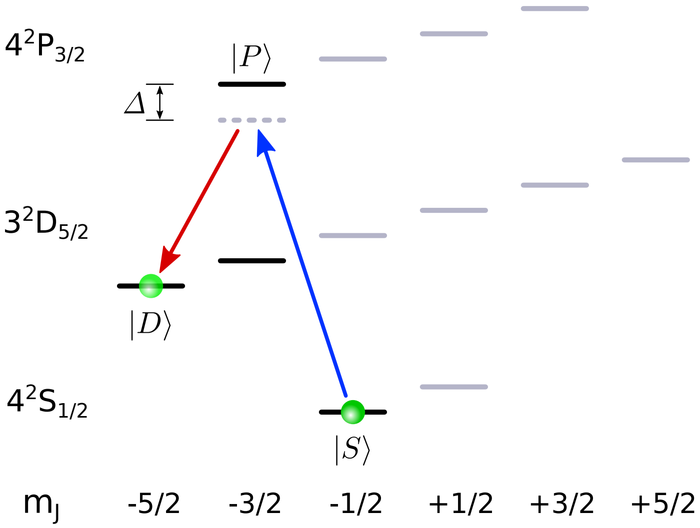

Figure 4.6: Level scheme with relevant transitions for the single-photon DLCZ protocol. After initialization in the $|S\rangle$-state, a cavity-induced stimulated Raman transition is driven to $|D\rangle$ via the $|P\rangle$ state, consisting of a Raman pulse (blue arrow) with detuning Δ, and the cavity fulfilling the Raman resonance condition with the beam. A single cavity photon is generated for both nodes, and the detection setup eliminates which-way information (see Figure 4.1 b) to entangle the nodes in $|S{,}D\rangle + |D{,}S\rangle$.

trolled by the duration of the Raman drive. It is detected with a probability P_{det} once emitted. This probability is given by

$$P_{\mathrm{det}} = \eta_P \cdot \eta_{\mathrm{out}} \cdot \varepsilon \cdot \eta_{QE}^{854} , \tag{4.45}$$

where η_P is the probability that the photon is emitted into the cavity mode through Purcell enhancement, η_{out} is the the cavity outcoupling coefficient, ε the mode matching efficiency between cavity and fiber and $\eta_{QE}^{854} = 0.5$ the quantum efficiency of the photon detectors near 854 nm. All of these parameters are defined and given in section 2.3, and lead to a detection efficiency of about $P_{\mathrm{det}} = 0.03$.

For a threshold fidelity of $F_{\mathrm{thr}} = 0.99$, and thus a single photon emission probability $p_1 = 0.01$, these parameters result in a success probability for one experimental run of $P_1 \approx 6 \times 10^{-4}$ according to Equation 4.13.

Entanglement generation rate: Each single experimental run can be conducted in time $\tau_{\mathrm{run}} = \tau_{\mathrm{prep}} + \tau_R + \tau_\kappa$, which is the sum of the preparation time τ_{prep}, the Raman pulse time τ_R, and the cavity decay time τ_κ (negligible in our case). For a threshold fidelity of $F_{\mathrm{thr}} = 0.99$, the single photon emission probability must fulfill $p_1 \leq 0.01$ according to Equation 4.14. A typical duration of the Raman drive pulse is $\tau_R = 2\,\mu\mathrm{s}$. The preparation time $\tau_{\mathrm{prep}} \approx 210\,\mu\mathrm{s}$ is substantially longer, leading to $\tau_{\mathrm{run}} \approx 212\,\mu\mathrm{s}$. The entanglement generation rate for these parameters results in $r_e \approx 2.8\,\mathrm{s}^{-1}$.

Fidelity: The fidelity loss due to events where two photons are generated from driving the stimulated Raman transition is preset by choice of F_{thr} and corresponding tuning of the drive pulse area. Additional fidelity loss is due to dark count events. However, choosing a detection window of $\tau_{\mathrm{det}} = 2\tau_\kappa$ after the Raman pulse, in order to capture the majority of real events, and with typical dark count rates of 20 Hz for IR detectors, erroneous events are 5 orders of magnitude less frequent than entangling events. Imperfect initialization and readout (section 3.2) also reduce the fidelity by a factor of $F_{\mathrm{init}} \approx 0.995$, similar to the EPR protocol, so the final fidelity for $F_{\mathrm{thr}} = 0.99$ is $F_1 \approx 0.99 \cdot 0.995$. Note that the single-photon DLCZ run time of $\tau_{\mathrm{run}} \approx 212\,\mu\mathrm{s}$ is short enough to ensure interferometric stability between two nodes for repeater distances well below 100 km [Min08]. For longer QR chains, or too-far distances of the nodes, some kind of active phase stabilization between distant nodes in the chain is needed, the requirements dependent on the length of the chain and the rate of entanglement generation. A possible solution is reference pulses with low jitter, as realized by Musha et al. [Mus08] or by Jiang et al. [Jia08].

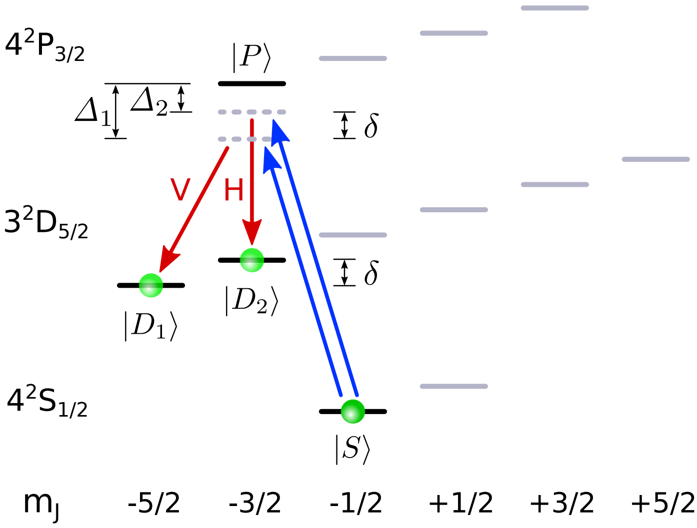

Figure 4.7: Level scheme with relevant transitions for the two-photon DLCZ protocol following Stute et al. [Stu12]. After initialization in the $|S\rangle$-state, two Raman transitions are driven simultaneously to $|D_1\rangle$ and $|D_2\rangle$ via the $|P\rangle$ state, consisting of a bichromatic Raman pulse (blue arrows) with detunings Δ_1 and Δ_2, and two modes of the cavity (V and H with respect to the cavity axis, red arrows). A cavity photon is generated, whose polarization V or H is entangled to the electronic state of the ion, $|D_1\rangle$ or $|D_2\rangle$, respectively.

Two-Photon-Detection DLCZ

We also investigate an alternative version of the DLCZ protocol based on deterministic photon emission and coincident two-photon detection [Sim03; Bar09].

The single Raman beam of subsection 4.1.2 is substituted by a bichromatic Raman beam, so that two cavity-induced stimulated Raman transitions are driven, see Figure 4.7:

$$|S\rangle\,|0\rangle_p \xrightarrow{\text{Raman}} |D_1\rangle\,|V\rangle + |D_2\rangle\,|H\rangle \ . \tag{4.46}$$

Note that $|D_1\rangle$ and $|D_2\rangle$ differ from the levels defined in subsection 4.2.1. The photons emitted on the σ- and π-transitions are mapped to the $|V\rangle$ and the $|H\rangle$ mode of the cavity by setting the quantization axis of the ion to right angles with the cavity axis.

The stationary qubits are entangled by two-photon detection. As Zippilli

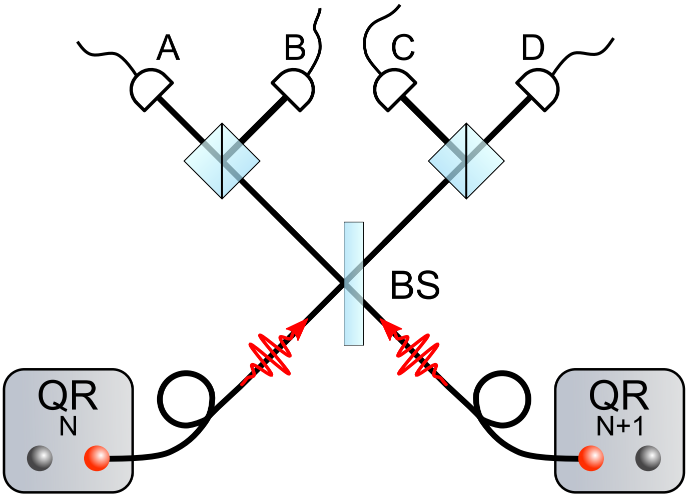

Figure 4.8: Alternative to the DLCZ method introduced in subsection 4.1.2. Both nodes emit a photon induced by a Raman transition, which is entangled with the ion according to Equation 4.46. The photons are brought to interference within a detection setup as pictured. Coincident clicks in detectors {AB, CD, AC, BD} project the two ions onto a Bell state.

et al. [Zip08] elaborates, this requires a 50/50 beamsplitter, with a polarizing beamsplitter (PBS) and two detectors at each output port, as depicted in Figure 4.8. Coincident clicks in detectors {AB, CD, AC, BD} project the two-qubit state onto the Bell state $\{\phi^+, \phi^-, \psi^+, \psi^-\}$. As these possibilities represent half of the two-photon detection events possible, this protocol cannot exceed a success probability of $P_2 = \frac{1}{2}$. Including the probability of detection P_{det} for each photon, and the probability p_1 of successfully inducing the Raman transition from Equation 4.46, which can be set as close to unity as possible, the success probability of this protocol is

$$P_2 = \frac{1}{2} p_1^2 P_{\text{det}}^2 \approx 4 \times 10^{-4} \; . \tag{4.47}$$

The two-photon detection eliminates the fidelity's dependence on photon loss, and is limited by the initialization and readout losses ($F = 0.995$), and the width of the cavity compared to the Zeeman splitting of the used transitions. Assuming a cavity centered on the transitions shown in Figure 4.7, a magnetic field of 10 G, and taking the Clebsch-Gordan-Coefficients for the transitions into account, the parasitic transition $|S\rangle \rightarrow \left|D_{5/2}, -1/2\right\rangle$ has an excitation probability of $\approx 0.75\,\%$. These detrimental effects reduce the fidelity to $F = 0.992$. Due to the coincident detection scheme, typical dark count rates for modern detectors lead to negligible errors.

The single experiment run time of this protocol is slightly lower than in the probabilistic DLCZ case, $\tau_{\text{run}} \approx 240\,\mu\text{s}$, as the Raman pulse duration is longer, $\tau_R \approx 30\,\mu\text{s}$, in order to achieve a π-pulse. The entanglement generation rate follows as $r_e \approx 1.6\,\text{s}^{-1}$.

This is slightly higher than the respective rate for the single-photon-detection DLCZ protocol at $F = 0.99$. Additionally, the two-photon-detection DLCZ rate r_e quickly surpasses that of the single-photon protocol for higher detection quantum efficiencies, a field of active technology development [Had09].

4.2.3 The Hybrid Protocol

An interesting alternative to the previous two protocols, the hybrid protocol as introduced in subsection 4.1.3 employs a continuous variable qubus. Although the protocol requires an overcoupled cavity, in contrast to the undercoupled one available in our setup, this section will show that upon realization of this condition, the protocol is by far the fastest means of entanglement distribution for medium high finesse. The qubus is encoded in the phase of a coherent light pulse near 854 nm, to distribute entanglement between QRs, and the optical qubit of the $^{40}\text{Ca}^+$-ion (section 3.2) as stationary qubit in the QR nodes. The

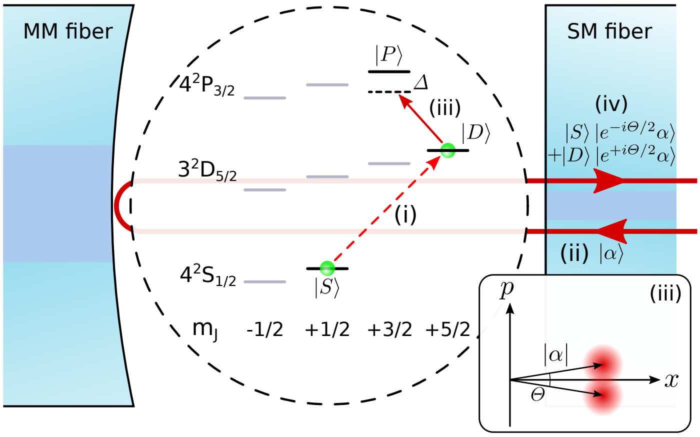

Figure 4.9: Sketch of the continuous variables hybrid protocol. (i) The ion is initialized in a superposition of $|S\rangle$ and $|D\rangle$, and then shuttled into the cavity mode. Now, the qubus is coupled into the cavity (ii), where both qubus and cavity are detuned by Δ to the $|P\rangle \leftrightarrow |D\rangle$ transition. The relevant levels of the $^{40}\mathrm{Ca}^+$-qubit are shown. (iii) The qubus obtains a phase shift θ (see inset) depending on the qubit state, entangling the flying qubus with the stationary qubit in the QR node (iv).

latter is initialized into the superposition (Figure 4.9)

$$|\Psi_i\rangle = \left|S_{1/2}, +1/2\right\rangle + \left|D_{5/2}, +5/2\right\rangle = |S\rangle + |D\rangle \ . \tag{4.48}$$

The ion is then shuttled into the cavity for interaction with the qubus. The qubus and the local oscillator (LO) reference pulse (subsection 4.1.3) are created by suitable attenuation and outcoupling of a laser pulse of duration τ_q. For the generation of entanglement, the qubus mode successively interacts dispersively and cavity-enhanced with stationary qubits in distant nodes QR (N) and QR (N+1), see Figure 4.1 c). The qubus is resonant with the cavity, far detuned by the frequency Δ from the transition frequency of $|D\rangle \rightarrow |P\rangle$. The detuning must fulfill $\Delta \gg 2 \cdot g_c = 2\pi \times 40.2\,\mathrm{MHz}$, in order to realize the dispersive regime.

Unlike the two previous protocols, the implementation of the hybrid protocol suggests the employment of an asymmetric cavity, where the mirror on the I/O fiber features a larger transmittance $T_1 = 200\,\mathrm{ppm}$, with T_i (R_i) the intensity transmittance (reflectance) of mirror i. All other cavity parameters are assumed to be the same as in section 5.6. The resulting minor decrease of the cooperativity from $C_c \approx 16$ to $C_c \approx 13$ is of no further relevance in this case.

In order to be able to send the coherent pulse from QR (N) to QR (N+1), we require an optical circulator. This can be realized, e.g., by inserting a $\frac{\lambda}{4}$-waveplate between the PBS and the QR nodes in Figure 4.1 c). Our imperfect cavity incoupling efficiency η_{dip} reduces the quality of our reflection signal. However, this detrimental effect can be eliminated by utilizing pulses split off of the LO for error correction, similar to the correction called tuning displacement by Ladd et al. [Lad06]. An LO pulse of correctly chosen amplitude interferes with the qubus at a weak beamsplitter, positioned behind the output port of the optical circulator. The beamsplitter is set up such that the LO pulse is phase shifted by π, and the unwanted, directly reflected field is subtracted from the qubus. For a weak beamsplitter, the entangled pulse is almost undisturbed (see Ladd et al. [Lad06]). The same error correction must be done after the pulse leaves QR (N+1), but before the detection. For an incoming field E_{inc}, the field E_{ref} reflected from the resonant cavity has the form [Mes05]

$$E_{\text{ref}} = \left(\sqrt{R_1} - \sqrt{\varepsilon} \frac{\sqrt{T_1^2 R_2}}{1 - \sqrt{R_1 R_2}} \right) E_{\text{inc}} \; . \tag{4.49}$$

The corrective pulse in this scheme is chosen to be by $E_{\text{corr}} = \sqrt{R_1} E_{\text{inc}}\, e^{i\pi}$. Combining both pulses results in the following effective reflection efficiency of the coherent pulse, including mode matching:

$$\eta_{\text{hyb}} = \frac{(E_{\text{ref}} + E_{\text{corr}})^2}{E_{\text{inc}}^2} = \varepsilon \frac{T_1^2 R_2}{(1 - \sqrt{R_1 R_2})^2} = 0.25 \tag{4.50}$$

for the parameters given above, and the mode matching $\varepsilon = 0.445$.

The qubus pulse duration τ_q should be suitably long, so that the cavity does not distort the shape of the pulse. We assume a pulse length of $\tau_q = 500\,\text{ns} \gg \tau_\kappa$, which satisfies this condition. Due to the length of the qubus, the detection needs to wait the same amount of time, so the entanglement time of the protocol is $\tau_e = 2\tau_\kappa + \tau_q + \tau_{\text{det}} \approx 1\,\mu\text{s}$, plus the time of light travel between the nodes, with τ_κ the cavity decay time, and τ_{det} the time needed to evaluate the detection events. As we aim for comparability between the protocols, we set the travel time to zero in this section.

The total transmission efficiency is

$$\eta = \eta_{\text{hyb}}^2 \, \eta_{FL} \approx 0.06 \; . \tag{4.51}$$

The effect of absorption due to fiber length, with a transmission efficiency of η_{FL}, further reduces η, but is beyond the scope of this paper, and is set to 1 for the remainder of this section.

The protocol is concluded by a homodyne detection, in order to project the joint state of the qubits in both QR nodes onto the mixed Bell state $\mu \left|\psi^{+}\right\rangle + \sqrt{1-\mu^{2}} \left|\psi^{-}\right\rangle$ of Equation 4.23 and Equation 4.24. This homodyne detection has to be able to discriminate the phases of the targeted part of the wave function and of the undesired part, see Equation 4.26. Using the estimated parameters from our setup, we find that the fidelity of Bell states is below 0.5 for any value of the distinguishability, and thus for any combination of α and θ, a result of the relatively large transmission loss η. The resulting state is a mixture of the four Bell states, which we cannot distinguish, rendering the homodyne measurement useless for entanglement distribution. However, we can completely eliminate the *bit-flip* errors that stem from the badly distinguishable phase-rotated and non-phase-rotated parts of Equation 4.23, by changing the detection scheme to an unambiguous state discrimination setup, as described in detail in subsection 4.1.4.

Entanglement generation rates: Similar to the other two protocols, one has to find a trade off between fidelity and efficiency. Choosing a fidelity $F = 0.99$ for good comparison with the DLCZ schemes, Equation 4.30 provides us with a success probability of $P_e \approx 9 \times 10^{-7}$ for optimal values of the distiguishability d, Equation 4.21. In order to find the optimal parameters, we require that $F = \mu^2 = 0.99$ (Equation 4.22), and maximize P_e with this constraint, with respect to α and θ. For, e.g., $\alpha = 100$, the optimal phase shift angle is $\theta \approx 2 \times 10^{-3}$. Thus, there are two ways to experimentally achieve the optimal rate: We can either change the qubus intensity $|\alpha|^2$ to optimize P_e for a given interaction strength between qubus and qubit, or we can move the ion within the cavity field, and thus change θ, to optimize P_e for a given qubus intensity α.

Since the dispersive interaction does not disturb the ionic state, we can skip ion initializations in between tries, until a new cooling cycle is necessary, greatly reducing the time investment required per run as compared to the other two protocols, setting $\tau_{\text{prep}} = 0$. These assumptions lead to a mean time to entanglement of $\tau_e \approx 0.13\,\text{s}$, and an entanglement generation rate of $r \approx 8\,\text{s}^{-1}$, which includes the ion initialization. Already for a modest drop in fidelity to 0.95, the rate increases to $170\,\text{s}^{-1}$, while for $F = 0.8$ the rate is $\approx 700\,\text{s}^{-1}$. The initialization and state readout errors once again reduce the fidelities presented in this section by a factor of 0.995 .

4.2.4 Performance Comparison of the Protocols

In the following we discuss key results for all protocols. The entanglement generation rate as a function of the fidelity is plotted for all considered protocol versions in Figure 4.10. Typically, there is an experimental parameter that can be tuned to trade the fidelity of resulting Bell states for their production rate. Also, the protocols differ considerably in their requirements for inter-node phase coherence of lasers used for state manipulation of the ion, and for the stability of the connecting fiber link.

The tunable parameter for the *EPR protocol* is the detection window τ_W, i.e., the time to wait for re-initialization. Up to a point, a short τ_W increases the fidelity by making erroneous dark counts less likely (see Equation 4.40 and Equation 4.41), while reducing the success probability by stopping the protocol before any EPR photon has interacted with an ion, see Equation 4.42 . Choosing this parameter too short, however, reduces the rate quickly, as the waiting time becomes shorter than the temporal shape of the herald photon wavepackets leaving the cavities. The interferometric stability of optical frequencies between QR nodes is not required in this protocol: The phase imprinted on the initial ionic state is set by the relative phase of the two transitions near 729 nm at each node (see Figure 4.5), whose frequency difference lies in the RF range. Consequently, phase coherence can be attained by distributing a stable RF reference signal between neighboring nodes. Any phase collected by the entangled photonic state during transmission is a global one. In order to improve the EPR protocol, one would work on the two major inefficiencies: On the one hand, the small photon detection probability of the herald is the largest contributor to the slow entanglement generation rate. Recent work (e.g., [Kur14; Sch14]) uses high aperture laser objectives for improved herald collection efficiency. On the other hand, the detection could also be improved by using a high-finesse, dual wavelength cavity for both the detection wavelength near 393 nm light, and the EPR-pair wavelength near 854 nm. Enhanced emission through the Purcell effect, however, would require a strong coupling regime for UV-cavities and come at the price of technical complexity.

The *single-photon detection DLCZ* offers as tunable parameter the single photon generation rate, see Equation 4.13 and Equation 4.14. The rate of Bell pair production rises with a higher rate of single photons, while the fidelity drops are caused by a higher probability for simultaneous photon emission in both QR nodes. The absolute phase of the laser field creating the qubit (see Figure 4.6) cannot be controlled, such that phase coherence between neighboring nodes needs to be established at optical frequencies. The relative phase of the photonic state depends on the position of the detector [Cab99] which requires that

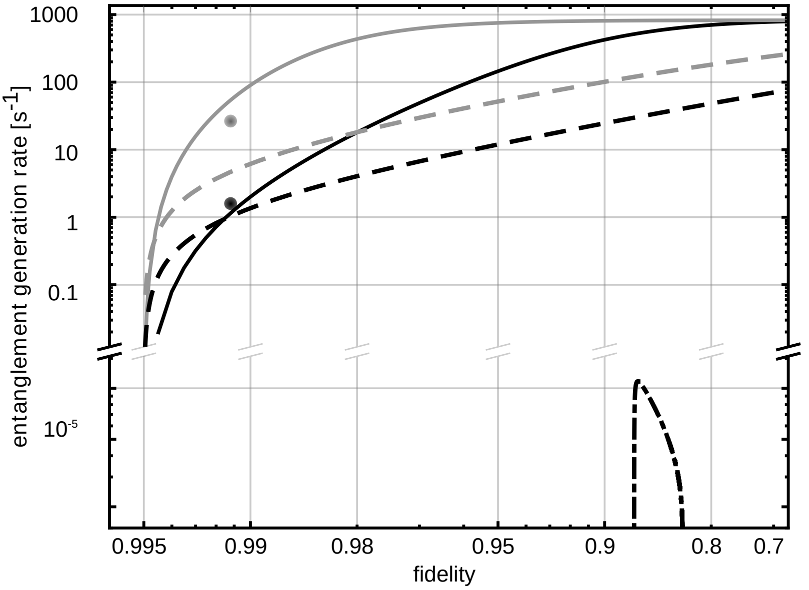

Figure 4.10: Entanglement generation rates possible at a given fidelity for each protocol. The EPR protocol (dash-dotted), the single-photon DLCZ protocol (dashed), the two-photon DLCZ protocol (dot), use the undercoupled cavity. The hybrid protocol with USD, for an overcoupled but otherwise identical cavity, is drawn solid. For high fidelities, $F \gtrsim 0.99$, the DLCZ protocol shows the best performance for our apparatus, while at fidelities below 0.99 the hybrid protocol becomes visibly better. For higher quantum efficiencies and an optimized cavity (see text), upper bounds for hybrid and DLCZ protocol rates are also plotted (grey). Results have been obtained numerically from Equation 4.39, Equation 4.15 and Equation 4.32.

the fiber link between QR nodes must be interferometrically stabilized. For details concerning the interferometric stability of fiber links, see e.g., [San11; Ma94; Min08; Jia08]. The rate of entangled pairs would benefit mostly from an improved transfer of the entangled photon to the detection apparatus, which is typically mainly limited by the coupling efficiency between the fiber cavity mode and the fiber mode. We realistically aim for increasing the mode matching ε from 0.44 to ≈ 0.54. Ultimately we are limited by the geometry of our setup to $\varepsilon_{\max} \approx 0.57$. For small values of the transfer and detection probability P_{det}, the entanglement rates increase only linearly with mode matching, by at most $\approx 23\,\%$. Similar gains could be achieved by reducing mirror losses to optimize the impedance matching, Equation 5.2, or by optimizing the ratio of reflectivity of the two cavity mirrors to improve the cavity outcoupling coefficient η_{out}.

For the *two-photon DLCZ*, decreasing the rate does not improve the fidelity of Bell states. Consequently, its performance is depicted in Figure 4.10 by single points. In this protocol, the ionic state is created by a bichromatic optical field (see Figure 4.7), which allows for a phase control by an RF-link. During the photon transmission, only the global phase of the photonic state is altered, which means the stability of the fiber link needs to ensure temporal coincidence of both of the photons impinging at the beamsplitter, but interferometric stability is not required [San11]. Any improvement of the mode matching would be most important for this protocol, as this parameter enters quadratically in Equation 4.47. A gain in performance (up to a $51\,\%$ increase for the optimized mode matching) is expected for a more precisely aligned fiber cavity.

Concerning the *hybrid protocol*, the larger the parameters θ or α are chosen, the higher the increase of the rate, at the cost of fidelity. This follows from Equation 4.22 and Equation 4.30 which mirror the mixing of pure and entangled states described in subsection 4.1.3. The protocol needs optically phase-stable lasers, as a monochromatic field is used to create the initial ionic state (see Figure 4.9). Interferometric stability for the fiber link is not required: The quantum information in the qubus is transmitted together with a local oscillator pulse, and a homodyne-type measurement eliminates all phases collected by both those parts during transmission, also in the case of USD detection. The hybrid protocol would benefit, similar to the DLCZ protocols, from an improved mode matching between fiber cavity and fiber, as well as an enhanced impedance matching. Realistically, we could refine the mode matching to $\varepsilon = 0.54$ which would yield an almost two orders of magnitude larger entanglement generation rate with $F = 0.99$.

In the hybrid and single-photon DLCZ protocols we might alleviate the requirement for inter-node phase coherence of lasers with an alternative way of creating the superposition of the $|S\rangle$- and $|D\rangle$-states: Creating a coherent superposition between the two $S_{1/2}$-Zeeman states using a Raman laser interaction (see Figure 2.1) [Pos09], followed by a coherent population transfer from one of those sublevels to the D-state via rapid adiabatic passage (RAP). After entanglement as been generated, each qubit could be coherently returned to the spin qubit by a second RAP, before the necessary local operations are performed. The phase coherence between QR nodes would then be ensured by an RF reference exchange.

In conclusion and taking above discussion into account, we note that the EPR protocol shows a comparatively small rate of entanglement generation and can hardly be implemented in our ion trap-cavity platform. However, for both the DLCZ protocol and the hybrid protocol utilizing USD, the estimated rates and fidelities for our parameters suggest the possibility of outperforming the state-of-the-art [Huc14], where free-space photon collection is employed. Both protocols would profit from a fiber optical cavity with a high reflectance end mirror on the multimode fiber [Ste14]. If the losses in the mirror coatings and the transmission through the high reflectance mirror could be brought well below 50 ppm, the cavity outcoupling coefficient would improve to a value that we estimate with $\eta_{\text{out}} \approx 0.26$. This would double η_{out} and in turn P_{det} for both DLCZ protocols, see Equation 4.45. Furthermore, with $\varepsilon \approx 0.54$, these conditions could enable the hybrid USD protocol to reach a rate of $\approx 750\,\text{s}^{-1}$ for a state fidelity of $F = 0.95$ (Figure 4.10).

5 Design and Construction

5.1 A Fiber Cavity for Paul Traps

This section concerns itself with the measured values for the fiber-based resonator developed during this thesis. Details of the development, and a more detailed characterization, can be found in the thesis of Marcel Salz [Sal13]. The electrodes for the Fibertrap V3 in the cavity region are 250 µm apart (see Figure 5.3 and Figure 5.12), which restricts the cavity fiber length to at least this distance. This demands a large diameter concave mirror structure on the fiber facet to avoid finesse limitations by clipping losses. We developed a novel technique for shaping these facets using a commercial focused ion beam (FIB) device[1], which allows us to create spherical structures with a large range of possible ROCs. Our cavity setup has a length of $L = 250$ µm and consists of a singlemode fiber with a plane surface and a multimode fiber with 350 µm ROC concave facet. The facets are coated with dielectric mirror layers with a target transmission of 50(15) ppm at a wavelength of 854 nm[2]. The linewidth was determined to be $2\,\kappa = 2\pi \times 36.6(5)$ MHz using frequency modulation as a frequency marker. The field decay rate of the cavity follows as $\kappa = 2\pi \times 18.3(3)$ MHz. A finesse of $\mathcal{F} = 1.65(2) \times 10^4$ is deduced. The cavity has a mode waist of $w_0 = 6.6$ µm, i.e., the maximum cavity-ion coupling parameter at the plane mirror is $g_0 = 2\pi \times 25.7$ MHz. In the cavity center, the coupling is reduced to

$$g_c = \frac{w_0}{w(L/2)} g_0 \ . \tag{5.1}$$

The set of cavity parameters thus reads

$$(g_c,\, \kappa,\, \gamma_{\mathrm{PD}},\, \gamma_{\mathrm{PS}}) = 2\pi \times (20.1,\, 18.3,\, 0.67,\, 10.7)\ \mathrm{MHz}\ ,$$

which means that the cavity operates in the intermediate coupling regime. As the decay rate $P_{3/2} \rightarrow S_{1/2}$ is as strong as the coupling parameter, this system will not display resonant coherent dynamics on the $D_{5/2} \leftrightarrow P_{3/2}$ transition. However, excitation and off-resonant dynamics supported by the cavity can be

---

[1] *FEI Helios NanoLab*

[2] *Laser Optik Garbsen*

utilized. Further effective reduction of the cavity coupling g_c due to geometrical considerations or Clebsch-Gordan coefficients of a particular atomic transition have been taken into account in the discussion of the protocol efficiencies in section 4.2.

It has been recently shown [Gal16] that mode matching for a fiber based cavity differs from the usual approach for Fabry-Pérot cavities as found, e.g., in Meschede [Mes05]. Most importantly, the minimum of the reflection signal no longer corresponds to the optimal incoupling. However, in our case we find minimal corrections, and will use the latter approach for brevity here. When coupling light into the cavity, two effects reduce the contrast of the reflection dip on resonance $\eta_{\text{dip}} = \varepsilon \cdot \eta_{\text{imp}}$ [Hoo01; Gal16]: The mode matching ε and the impedance matching, described by the coefficient η_{imp}, which depends on the transmission T of the cavity mirrors and the total losses $\mathcal{L}$ per round trip. The losses are determined to be $\mathcal{L} = 280(30)$ ppm. For symmetric coating $T_1 = T_2 \equiv T$:

$$\eta_{\text{imp}} = 1 - \left(\frac{\mathcal{L}}{2\,T + \mathcal{L}}\right)^2 = (45.6 \pm 9.1)\,\% \ . \tag{5.2}$$

Comparing this to the experimentally observed contrast of $\eta_{\text{dip}} = 20.3(1)\,\%$, one obtains

$$\varepsilon = \frac{\eta_{\text{dip}}}{\eta_{\text{imp}}} = (44.5 \pm 8.9)\,\% \ . \tag{5.3}$$

The probability that a resonant photon emitted from the ion enters the cavity mode is enhanced by the Purcell effect and given by

$$\eta_P = \frac{2C_c}{2C_c + 1} = 0.97 \ , \tag{5.4}$$

where C_c is the cooperativity in the cavity center,

$$C_c = \frac{g_c^2}{2\,\gamma_{\text{PD}}\,\kappa} = 16.5 \ . \tag{5.5}$$

Neglecting mode matching, such a photon then has the probability

$$\eta_{out} = \frac{T}{2T + \mathcal{L}} = 0.13 \tag{5.6}$$

of leaving the cavity through the single mode mirror, which is the ratio of this mirror's transmission loss to the sum of all loss channels of the cavity. To ensure the frequency stability of the fiber cavity, the fiber cavity can be actively stabilized to a laser before each experimental shot. The setup so far features only one input/output (I/O) port, in the form of the fiber-based cavity. In order to extend the setup to actual QR chains, the singlemode I/O fiber can also be equipped with a fiber switching device in front of the left fiber of Figure 4.4.

5.2 Trap Design

5.2.1 The Segmented Linear Micro Ion Trap

The trap design used in this thesis is derived from the linear segmented microfabricated design of [Sch08; Sch09].

Microfabricated ion traps are three-layered structures of alumina-wafers, with the outer layers sporting a structured gold layer of conductors, while the middle layer functions as spacer to set the electrode distance between the outer layers to $125 - 250\,\mu\mathrm{m}$, dependent on design. Each layer also features a trap slit, with a width of $250 - 500\,\mu\mathrm{m}$, through which laser and camera access is possible, and calcium loading is performed. The layer distance and slit width together provide the two principal numbers for the trapping geometry, inscribing the rectangle of the electrodes.

The small dimensions of the trap allow for deep trapping potentials and thus high mode frequencies in the range of a few Megahertz for all eigenmodes of a trapped ion. This leads to a high speed of quantum gates, and fine control over the position of the ions in the trap.

A segmented linear ion trap features multiple independent electrodes along the trap slit, over 30 in each of our designs, which can be used to create multiple distinct trapping wells. With cold and fast transport, ion crystal splitting and ion swapping operations [Wal12; Bow12; Rus14; Kau14; Kau17a], these individual wells make it possible to address single ions as well as arbitrary ion pairs with high fidelity.

5.2.2 Cavity Integration

Integrating a high-finesse fiber-based cavity with a trapped ion experiment leads to very specific constraints on the experimental design. In general, trapped ion experiments require an electrode separation balanced between two competing requirements: a comparatively large trap slit for easy laser access and low anomalous heating rates, as well as the precise control of the ion positions and faster gate times given by more compact designs. The cavity adds the additional requirement of low mode volume to enhance the coupling, as well as the additional difficulty of introducing a dielectric material into both the RF field of the trap and the region of scattered laser light [Har10], pushing the optimal equilibrium of diverging demands further towards tight trap slits and close electrodes. The similar magnitude of the electrode distance of a microfabricated ion trap and of a fiber-based cavity allow us to integrate the latter into the former. For a trap slit of 250 µm width and a cavity of roughly 260 µm length, the dielectric material of the fiber and the mirrors is at least partly shielded by the electrodes from ionizing laser light. Furthermore, unlike in bladed ion trap designs with integrated fiber-based cavities, the distorting effect of the fibers on the trapping RF field are reduced by the relative closeness of the electrodes to the ions compared to the fiber mirrors.

The ease of cold and fast transport operations make it possible to designate a *laser interaction zone* roughly 2 mm from the cavity, strongly reducing stray light ionization of the fibers and mirrors, from which prepared ions are then shuttled into the cavity mode, or *cavity interaction zone*.

One important design constraint for the integrated trap in comparison to the original design of [Sch08] is the need for mounting the cavity fibers as close to the mirrors as possible, to achieve a stable configuration and reduce as many of the eigenmodes of mechanical oscillation as possible. This then reduced the area available for conducting paths and connection pads to the voltage sources by half in comparison to the original design by Schulz et al. The size of the connection pads, on the other hand, is limited to a minimum of 660 µm by the width of the pitch capacitance arrays subsection 5.4.2, and by the need for multiple wire bonds with a radius of roughly 100 µm. This means we cannot connect all the segments individually to the outside. Instead, for the integrated trap, later segments are grouped together and connected by *vertical interconnect accesses* (VIAs). This permits us to control the last 14 to 20 DC segments, corresponding to 28 to 40 electrodes, through only 8 to 10 bond pads.

5.2.3 Further Considerations

Despite the small trap slit of 250 µm, ion trapping and manipulation are easily manageable. However, in case stray light requirements become more demanding, it is possible to utilize a special *loading zone* with a wider slit of $350 - 500$ µm, which reduces the amount of scattered light from the lasers. The loading zone is connected by a three-electrode wide taper region, in which the slit becomes increasingly narrow.

Slight misalignment of the outer layers of the trap can lead to a shift in the minimum of the RF potential. In ordinary ion trap experiments, it is sufficient to shift the ion position into the RF minimum by applying a compensation voltage of equal magnitude but opposite signs to the two DC electrodes of each segment. For CQED experiments, however, it is necessary to align the cavity mode with the ion position, and thus with the RF minimum. This can be achieved by two individually addressable RF electrodes in our trap designs, which enable us to apply two different RF voltage levels to precisely shift the RF minimum along the axis of the two RF sides [Her09]. Four additional compensation electrodes are added to the layers, two behind each RF electrode on the ion facing side. With their help, it is possible to compensate the ions in both radial directions, to keep them well compensated even when the RF minimum is shifted. The two compensation electrodes per side are responsible for the cavity region and the non-cavity region. Here, we define "cavity region" as "segments that are connected by VIAs" for the purpose of trap construction. The setup allows independent compensation of ion micromotion for the case that the cavity shifts the ion out of the RF minimum to a troublesome degree.

5.3 Trap Fabrication

As mentioned above (in subsection 5.2.1), the integrated ion trap consists of three alumina (Aluminum Oxide, Al_2O_3)[3] layers, two of which have a gold layer evaporated onto them as basis for conducting paths. The basic resource for trap production are either 125 µm or 250 µm thick alumina wafers, in a standard 2 in×2 in wafer. Our designs all follow the same four steps, namely laser cutting the layer shapes into the wafers, evaporating a thin gold layer onto the substrate, laser cutting the conducting paths into the gold layers, and breaking the layers out of their respective wafers. The latest trap design also includes the additional next-to-last step of electroplating gold onto the conductors to increase the thickness of the gold layer by about a factor of 10. Unless otherwise described, the steps follow the procedures laid out by Schulz [Sch09] and, for the latest trap design, by Kaufmann [Kau17b].

In more detail, the steps are as follows:

1. **Laser machining:** A number of alumina wafers are sent to an external contractor [4] and cut into shape according to autocad files provided by us. The cutting process is done by a femtosecond laser, which cuts multiple layers, usually eight, into one wafer. This first laser machining step contains all cuts which penetrate the chip, but which should be coated with gold in the end. This are mainly the trap slits and all required VIAs.

---

[3] Coors ADS996-polished / Al_2O_3 99,6 %

[4] Micreon GmbH, Garbsener Landstraße 10, 30419 Hannover, Germany

2. **Gold coating:** The laser machined wafers are then subjected to an intense cleaning regimen to ensure a clean surface for the gold coating. The wafers are first dipped into a succession of heated solvents (70 °C deionized water, 40 °C isopropyl alcohol, 40 °C acetone) and, if the slit geometry is stable enough, subjected to an ultrasonic bath. After each step, the wafer is rinsed with deionized water. It is then cleaned with *piranha solution*, an highly corrosive and aggressive oxidizer, prepared by slowly adding one part hydrogen peroxide (30 % H_2O_2 solution) to four parts sulfuric acid (98 % H_2SO_4). The piranha removes most leftover organic components that survived the solvent treatment, as well as inorganic but oxidizeable reactants on the wafer's surface. It is then rinsed with deionized water and isopropyl alcohol, and hung from wires stretched across a suitably large beaker, whose top is closed off with aluminum foil to prevent contamination. After about an hour of drying, the wafers are packaged and sent to the University of Ulm for gold coating.

   The coating is done by Rudolf Rösch[5] with an electron beam physical vapor deposition machine. The wafers need to be coated with 50 nm of titanium to prepare for the gold coating. The gold is then evaporated onto this layer with a thickness of 500 nm. For each process, the wafer is rotated, to ensure a uniform deposition. However, it seems as if small VIAs and the edges of wafers are plated significantly less thick, even though this precaution has been taken.

3. **Cutting the conducting paths:** The wafers are sent to Micreon again, where the final cuts into the gold surface and the wafer are made. This is a two-step process, in which first the femtosecond laser is set to only cut through the gold and titanium layers. The isolation trenches of the trap layers are cut in this step. The next step is to cut through the entire wafer again, to create all necessary conduction breaks that isolate all electrodes on the side of each chip. All but the last design of chips are cut out of the wafers in this step. For the last integrated ion trap design, the chips are still attached to the wafer by a perforation that connects each electrode of the chip to the wafer's gold coat.

4. **Electroplating:** This step was not done for Fibertrap V1. Fibertrap V2 was created by repairing the broken, but already finished, Fibertrap V1 through electroplating. Fibertrap V3 was constructed from parts electroplated before being combined. The plating was performed based on

---

[5] Universität Ulm, Institut für Optoelektronik, Albert-Einstein-Allee 45, 89081 Ulm

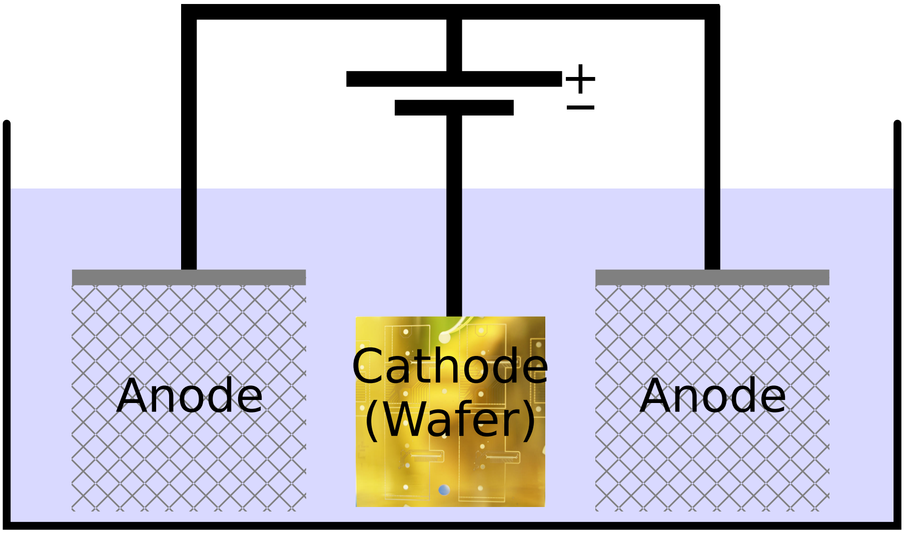

Figure 5.1: Basic scheme of an electroplating setup. The target of the electrodeposition, the wafer, is placed as cathode in between two anodes. Applying a current leads to gold ions in the electroplating solution (blue) to flow to the wafer, where they are reduced on any conducting surface connected to the circuit, thereby growing the thickness of the gold layer. The anodes are platinum coated titanium in our case.

the work of Blakestad and of Kaufmann [Bla10; Kau17b], with a sulfite-based gold solution (see subsection 5.3.1). A detailed description of the procedure is appended to this section.

5.3.1 Electroplating

Electroplating creates a thin coherent metal coating on an electrode by reducing metal cations dissolved in an electroplating solution. The reduction is effected by electrical current. The entire process is called *electrodeposition*. The electrode to be plated is the cathode of the circuit, a basic setup is depicted in Figure 5.1.

We used a non-cyanide, sulfite based gold solution from the company Metakem[6]. As a sulfite (SO_3^{2-}) based solution, it dissolves the gold ions, Au^{3+}, in water by bonding with the sulfite, which encases each gold ion in a layer of multiple molecules. The applied potential transports these complexes to the cathode,

---

[6] Gold-SF-Bath, Metakem GmbH, Achtzehnmorgenweg 3, 61250 Usingen, Germany

where the sulfite is oxidized to sulfate (SO_4^{2-}), and the gold is reduced to Au and incorporated into the gold layer present on the cathode. The result is a growth of the gold layer on the wafer, increasing the thickness of the previously vapor-deposited gold layer from 500 nm to up to 10 µm. This upper bound is due to limitations in our trap construction, not of the electrochemical process.

The following items are prepared before starting the procedure:

- A thoroughly cleaned chemical beaker for 1 L of liquid. It should be wiped clean with dishwater and a clean sponge, then rinsed with a succession of isopropanol and acetone, and finally DI water. Intermediate steps, in which dishwashing detergent is filled into the beaker and the beaker set into an ultrasonic bath for a couple of minutes, increase the confidence in the cleaning process. Fatty residues that require further cleaning show up on the glass surface when the DI water runs off, either as areas of heavy droplet formation, or otherwise suspiciously uneven water runoff. The beaker need not be dried as long as the DI water droplets are sure to be clean, since the Gold-SF-Bath is water based. In addition to the beaker, a ceramic coated magnetic stirrer is used so that we can stir the solution.

- The thoroughly rinsed anodes[7] of the electroplating circuit. We use platinum coated titanium anodes, made to fit a standard beaker. The target is placed between two anodes. Wiping the anodes is best avoided, as lint from any sponge or wipe is likely to catch on to the rough edges of the anodes, so cleaning them in an ultrasonic bath (with a succession of dishwater, isopropanol, acetone and DI water) is recommended.

- A wafer holding frame made of PVC. This fixes the wafer to be plated in the center of the beaker, in the middle of the two anodes, while still leaving the frame the degree of freedom to move vertically. This should avoid a standing, but uneven, flow of the electroplating solution along the wafer. Care must be taken when cleaning the PVC frame, since PVC dissolves slowly in isopropanol, and quickly in acetone. As an alternative, long ultrasonic baths in dishwater made from DI water are recommended. As usual, the final step should be a thorough rinse with pure DI water, to remove any residual solvents.

- A current source, an ampere meter and a voltmeter to supply the electrogalvanic circuit with current and monitor the current and voltage. A

---

[7] `http://www.metakem.com/en/products/special-chemicals-a-equipment/beaker-glass-anodes.html`

silver reference electrode is used to monitor the potential drop from the solution to the target. Due to the high conductivity of the solution, this works well without additional measures to create a small measure point as close to the target as possible.

- An electromotor with rotating arm, to create the up-down motion referenced above.
- A heat plate with magnetic stirrer motor to heat up the solution and drive the ceramic stirrer.

The operating temperature of this solution is 60(2) °C. The solution is poured into a beaker of appropriate size, for wafer plating we have used 1 L of solution. Importantly, the solution must be filtered each time it is poured into the beaker, and again after extended use (ca 4 hours of electroplating or more) to remove tiny gold nuggets that grow due to the oxidization of the sulfite. If unfiltered, these nuggets can reach sizes that threaten to short out the electrodes and conducting paths of the chips. To reach this temperature, the outer bath of water is heated to $\approx$ 80 °C, and 1 L of the Gold-SF-Bath, in the beaker, is placed into this outer bath. The thermalization is supervised by a thermometer inserted into the beaker. The temperature is regulated by the heat plate, and in the case of overheating, by adding cold water to the outer bath. Once the solution is at the correct temperature, the circuit according to Figure 5.1 is set up, with the measuring devices included appropriately. The ampere meter is inserted serially after the current source, and the voltmeter set up to measure the potential drop from the reference electrode to the cathode. To achieve an even distribution of the gold growth, the solution is stirred at $400 - 600$ rpm, and moved vertically for a couple of centimeters at 2-5 rpm. The technical data sheet fo the Gold-SF-Bath suggests an optimal current of $1\,\mathrm{A/dm^2}$ of plated area. This value was never reached with whole chips or wafers in this setup. The reasons for this, and the limits we experienced, are described in section 5.6.

5.4 Mounting of Trap and Fiber Cavity

5.4.1 Combining the Chips to an Ion Trap

To fix the three alumina chips that make up one trap, we mount them on top of a soft, but residually conductive plastic synthetic material[8]. The residual conductivity should help reduce the attraction of this mount for electrostatically

---

[8] S plus+ Bright ESD, Murtfeldt Kunststoffe GmbH & Co. KG, Heßlingsweg 14-16 44309 Dortmund, Germany

charged lint floating around that could damage the gold layer. Due to the sensitive nature of the conducting gold layer around VIAs, it is of paramount importance that the holder features a gap around the area of the trap that contains VIAs, to avoid any contact with them. The chips are aligned to each other under a microscope with up to 1000× magnification.

Glue mounting the trap chips

For all but the last design of the integrated ion trap, the three alumina chips are glued together using UV-hardening epoxy[9]. It is applied to gluing holes left in each chip. In comparison to the screw mounted method described next, this has the benefit of minimal disturbance of the setup after alignment, while the glue is hardened. The entire trap is then glued to the filterboard described in subsection 5.4.2.

Screw mounting the trap chips

For the last design of the integrated ion trap, the three chips are screw mounted onto an alumina support holder that will attach the trap to the filterboard. This procedure closely follows the one laid out by Kaufmann [Kau17b], with minor variations. We use M1.2 titanium screws instead of M1, for increased ease of use. The maximum torque we apply to the screws, which all chips are able to endure, is 5 Ncm. This suffices to fix the trap chips stably.

In comparison to the glue mounted method, this method has the drawback of torque necessarily being applied slightly shifting the chips versus each other, in a manner incompatible to the exacting requirements of ion trap alignment. It is thus necessary to compensate for this shift before applying the screw torque. It does have the benefit of reversibility, though, so multiple tries can be undertaken, and errors fixed.

5.4.2 Filterboard

The DC and the RF compensation electrodes of the trap are filtered by two sets of consecutive RC lowpass filters. These filters serve the dual purpose of removing electrical noise picked up from the lab on the DC signals, as well as protecting the voltage supplies from RF pickup from the trap drive. The first and outer filters are built into custom made plugs mounted to the outside of the vacuum chamber flange feedthroughs for the DC and RF compensation signals. The cutoff for this set is around $2\pi \times 50\,\mathrm{MHz}$.

---

[9] OG 116, Epoxy Technology, Inc., 14 Fortune Drive, Billerica, MA 01821

Close to the trap, on an alumina board mounting the trap, a second set of filters for all DC electrodes including the RF compensation is produced via thick film printing technology. This board was built by Marco Luniak[10]. Conductors, solder- and bondpads, and 10 Ω resistances are printed onto a laser cut alumina wafer. In a second step, pitch capacitance arrays are soldered onto the filterboard, and connected to the conductors on one side, and the respective trap electrodes on the other, via gold ball bonding. The trap is screwed to the filterboard using support wafers with screw holes for the trap and for the filterboard.

5.4.3 Cavity Mount

The fiber-based cavity introduced in section 5.1 has exacting requirements in order to operate at acceptable efficiency while integrated into an ion trap. The small size of fiber ends, as well as the fact that only a certain region of the FIB shaped fiber is acceptably circular for a high-finesse cavity, result in a system that must be aligned to at least single micrometer precision. Another source of difficulties is keeping the alignment stable over short and long times scales.

The long time scale can be effectively dealt with via setups with included 3D translation stages. However, the relatively large size of such a setup, especially the long distance that the fibers are connected with each other over, leads to a large amount of mechanical oscillations and thus difficulties of keeping the cavity locked. For our setup, we have chosen a monolithic cavity holder of 5 cm × 5 cm extent. This minimizes the instabilities mentioned above, but we are unable to adjust the lateral cavity position after the setup is integrated into the ion trap.

5.5 Bakeout

It is standard procedure for ion trapping experiments to perform a final round of evaporative cleaning of the vacuum chamber, the so-called *bakeout*. The entire vacuum setup is assembled and attached to a turbo-molecular pump stand. Depressurization and heating of the setup to about 200 °C leads to evaporation of residual oils, fats and solvents, hydrogen from the steel material and most importantly water attracted by the steel surface, all of which can then be removed via the pump. This procedure usually takes about two weeks. The fiber cavity, however, is very susceptible to de-alignment while being heated, as well as to

---

[10] Technische Universität Dresden: Fakultät Elektrotechnik und Informationstechnik, Institut für Aufbau und Verbindungstechnik der Elektronik

loss of fidelity in the mirror surfaces if heated under vacuum [Bra13]. Experiments conducted with a mock setup under atmospheric pressures show that a cavity attached to our holder permanently de-aligns at temperatures over 80 °C. Since we lack the ability to realign the cavity once it is integrated, a bakeout including the cavity is out of question. Instead, we opted to perform a bakeout for each trap without the fiber cavity integrated, in order to anneal and clean most surfaces. This bakeout is performed according to the usual parameters, 180 °C for two weeks, with a mass spectrometer measuring the decrease of the contaminants flowing through the valve to the pump. Afterwards, the ion trap is removed from the vacuum setup in a clean room atmosphere. The fiber cavity setup is then carefully attached to the ion trap setup, so that the cavity mode is aligned with segment number 31 of the ion trap. After the cavity is integrated into the ion trap, the whole setup is reattached to the vacuum chamber and depressurized. No further bakeout is performed. This lack of a further bakeout degrades the vacuum within the chamber. In general, the ion trap chambers in our group reach pressures in the order of 10^{-11} mBar, while our traps with incomplete bakeout procedures only attain $10^{-10} - 10^{-9}$ mBar. This has more frequent ion losses as effect. In our trap operation, we can still reach average ion retainment times of 10 to 30 min, long enough by far to perform experiments in an ion trap.

5.6 Integrated Fiber Cavity Ion Trap Designs

In the course of this thesis, a succession of ion traps was built in order to overcome difficulties with previous designs. The starting point was the micro trap design by Schulz [Sch09], which had already been adapted to incorporate a fiber cavity integrated into the spacer layer of the trap [Hei11; Zie12]. This setup allowed a cavity length of up to 100 µm, less than the distance of the electrodes. This design led to the following realizations:

- For longer cavities, a different cavity holding mechanism is required
- The UHV-compatible copper-coated fibers we use to build our cavities are coated in an inconspicuous layer of carbon to bond the copper to the glass, which needs to be burnt off near the fiber tip prior to any further mirror fabrication step
- The redesign of the cavity holding mechanism requires a redesign of the entire trap

The trap was integral in testing our high-stability voltage supply (described in section 2.5) and in developing the transport sequences required to move ions

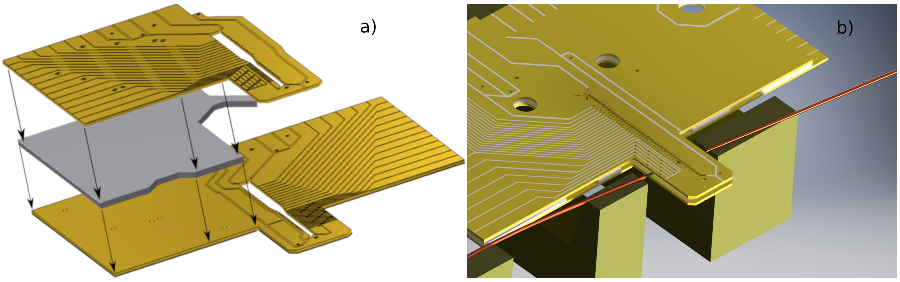

Figure 5.2: a) Elements of a microfabricated ion trap. The bottom layer and top layer are separated by a spacer. The three layers are either glued together with UV-hardening glue (Fibertrap V1 and V2, as in *a)*), or fastened to a support layer with small titanium screws (Fibertrap V3, shown in *b)*). The fiber is inserted into the snout of the trap, between the top and bottom layer as shown in *b)* with the fiber depicted in red.

from the loading and processor to the cavity zone. However, it was clear that a new design was required to realize a light-ion interface in an ion trap.

Typical trap operation parameters for ions in the loading zone were around $V_{\mathrm{rf}}^{\mathrm{pp}} \approx 300 - 400\,\mathrm{V}$, and $V_{\mathrm{DC}} \approx -(4 - 9)\,\mathrm{V}$, at a trap drive frequency of $\Omega_{\mathrm{rf}} = 18.6\,\mathrm{MHz}$. For operations in the processing zone, the parameters were often reduced to roughly half the voltages. The same values are true for the Fibertraps V1 and V2, up to the realization described in subsection 5.6.2 that these high RF voltages were damaging the VIAs.

5.6.1 Fibertrap V1

The next iteration of the fibertrap, *Fibertrap V1*, was presented by Max Hettrich [Het16]. The main focus lay on the integration of a fiber cavity with slightly over 250 µm length, so that the fibers are no longer closer to the ions than the trapping electrodes are, reducing their impact on the trapping potential. Additionally, the fibers are shielded by the electrodes from direct laser light, reducing surface charge buildup on the dielectric surfaces. This trap is the first one for which the cavity holder described in subsection 5.4.3 was developed, and required the removal of half of the trap circumference (see Figure 5.3). In order to accommodate the attachment points of the fiber cavity, half the trap slit is now part of an extrusion out of the chip bodies.

Since we coat the trap with a 500 nm thick sheet of gold, via a vapor deposition machine (section 5.3), it is necessary to make conducting paths with a

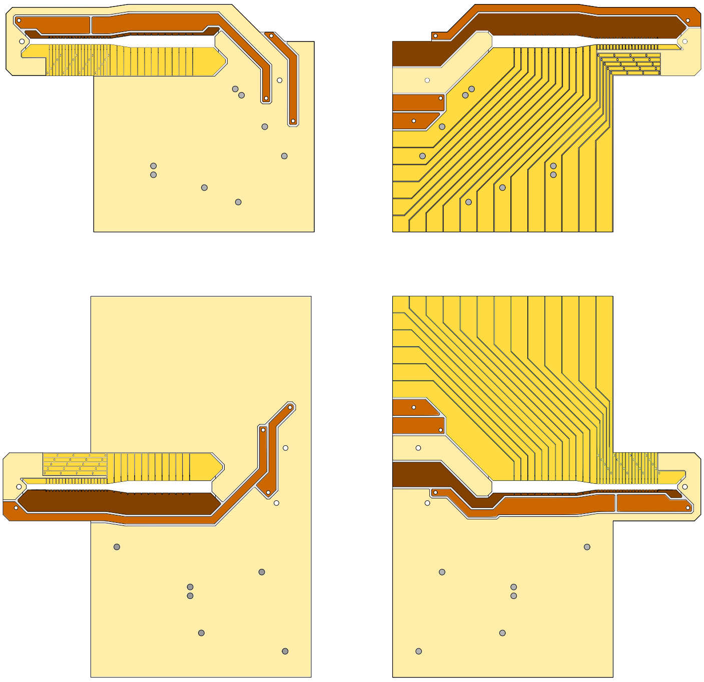

Figure 5.3: CAD drawing of the Fibertraps 1 and 2 presented by Hettrich [Het16]. DC electrodes are colored golden, RF in brown, the two compensation electrodes per chip are orange, and all ground planes are beige. Clockwise from the top left corner: Top layer, ion facing. Top layer, outward facing. Bottom layer, outward facing. Bottom layer, ion facing. Grey filled circles in the ground plane are alignment and gluing holes. The open circles are VIAs (see subsection 5.2.2) that connect conductors across the layers of one chip.

minimum width of 100 µm to avoid large resistances on the trap surface, which would degrade ion transport and crystal operations. Taking the minimum width of the conducting paths and the maximum width of the extrusion into account, we had to connect the electrodes towards the cavity zone via a Vertical Interconnect Access design (see subsection 5.2.2). While the Heinrich-Ziesel trap successfully used VIAs for some of the electrodes, the new DC electrode VIAs needed to be smaller, with an elongated rounded profile of 50 µm×30 µm, instead of the round 100µm profile of the previous versions. The gold vapor deposition was also the source of the most severe weakness of the Fibertrap V1: The thin gold layer was only weakly connected around the DC VIAs, leading to extraordinarily sensitive connections. The first time we installed the Fibertrap V1, 11 of 40 DC VIA connections were broken during the construction phase, while the chips were aligned to each other and glued together. We suspect that this happened on a construction holder made of polytetrafluoroethylene (PTFE). However, it was first discovered when transport tests with a trapped ion revealed floating electrodes, or those with unacceptably high resistances to the voltage source. The broken connections were confirmed later on, once the trap was removed from vacuum.

The replacement Fibertrap V1 was thus constructed on a new PTFE construction holder, with a hollow where the VIAs would touch the material otherwise. This guaranteed that the connections would stay inviolate. All electrode connections from the bond pads to the segment tips were measured after the trap was completed, but not yet vacuum mounted, and proven to be valid. When operation started up, however, even the unscratched VIAs proved to be too tenuous for trap operation: During startup operations, a resonance shift in the trap drive frequency portended the breaking of the VIA for segment 13. Later transport tests with ions confirmed the suspicion that the first VIA broke down under operation, presumably due to currents picked up from the RF electrodes, which were too overpowered for the weak VIA connection. The connections were again confirmed to be broken once the trap left the vacuum chamber.

5.6.2 Fibertrap V2

For the construction of *Fibertrap V2*, we were able to utilize a new trap construction technique: Electrogalvanic plating of gold (*electroplating*) onto the sputtered structure (subsection 5.3.1). This technique had been successfully applied during trap construction in Blakestad [Bla10], and by Kaufmann [Kau17b] in this group. As the second iteration of Fibertrap V1 had to be replaced, we decided to reinforce and repair the VIA connections of this trap by electroplat-

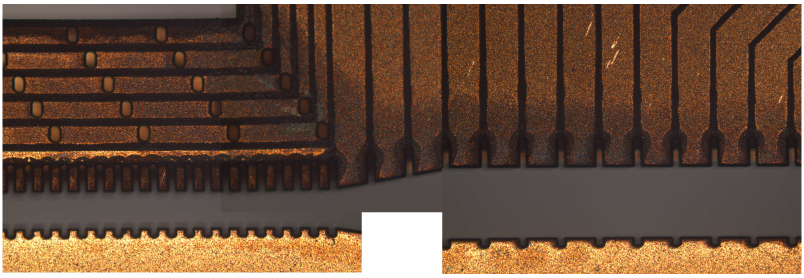

Figure 5.4: Combined microscope pictures of the trap slit of Fibertrap V2 after electroplating. Note the discoloration of the gold layer, especially around small structures of the trap.

ing. It follows that the plans of Fibertrap V2 are identical to Fibertrap V1, Figure 5.3. The assembled but broken trap was electroplated in 900 mL of a sulfite-based gold solution[11].

A test setup constructed from a dummy trap (bad chips used to train trap construction) showed that an assembled trap cannot be electroplated with the same current, and thus gold deposition speed, as the freshly created chips described by Kaufmann [Kau17b]. If the settings of Kaufmann are used, the isolation trenches are filled with gold, leading to shorted circuits and an inoperable ion trap. However, slow electroplating speeds and frequent checks on the state of the isolation trenches allowed us to keep the trap free of shorts between the conducting lanes, while sufficiently increasing the thickness of the gold layer to significantly strengthen all remaining VIAs. The enhanced gold layer showed discolorations on many surfaces (see Figure 5.4 and Figure 5.5 for examples). A range of possible explanations where found in dialog with the CEO of METACHEM[12].

The discoloration could be:

- the result of the low current applied to the circuit during the electroplating process. The recipe calls for applying 1 A/dm^2, typical values during operation were around one fifth the value. Due to the shorting problems mentioned, we could only apply 1.0 V to the circuit, keeping the current well below the suggested value. Gold electroplated with wrong currents can, instead of growing in a metallic sheet, grow in fine structures appearing dark-colored to the eye.

- the result of contaminants on the trap surface. These would be a result of

---

[11] Gold-SF-Bad, METACHEM GmbH, Achtzehnmorgenweg 3 D-61250 Usingen

[12] Dr. Friedrich von Stutterheim

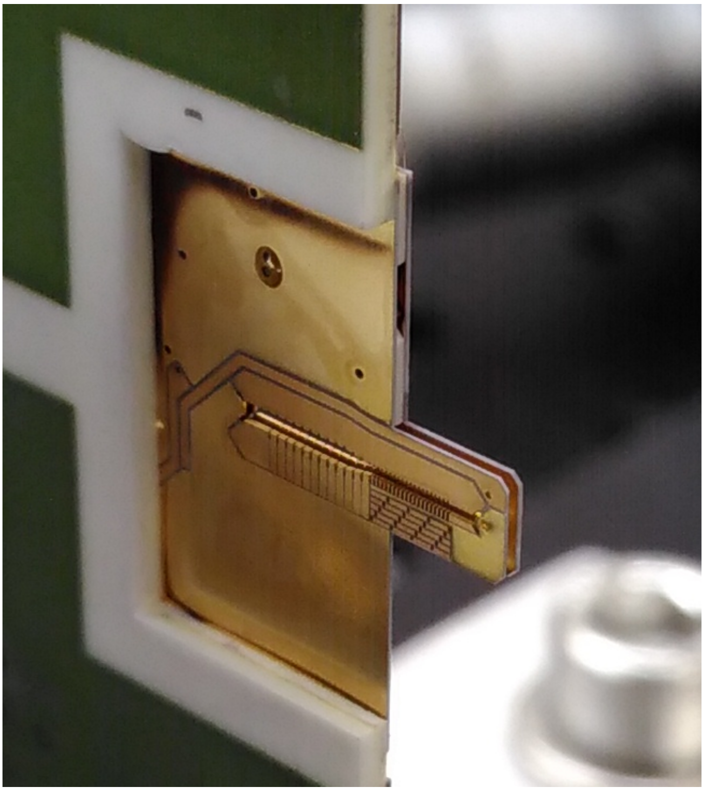

Figure 5.5: Dark discoloration of electroplated gold on the outward facing side of Fibertap V2. The effect of inadequate flow of the electroplating fluid can be seen in the almost black frame the filterboard–trap interface shows. The probable cause for this is the presence, and possible integration into the gold layer, of sulfate ions (SO_4^{2-}), a waste product of the electrolysis process that needs to be flushed from the reaction region.

the trap already being glued together during electroplating. This made it impossible to clean as rigorously as we usually do. Ultrasonic baths were deemed too risky for the trap structure, and simple bathing in solvents, and rinsing the trap off with them, was done. In addition, the surface seen in Figure 5.4 was subjected to being sputtered with a large amount of calcium from the calcium oven during operation. While it was dissolved in deionized water, it is possible contaminating amounts remained.

- the result of inadequate turbulence of the solution at the affected areas, leading to a buildup of sulfates, SO_4^{2-}, at the interaction interface. These either disturb the gold accumulation, leading to uneven structures that become dark-colored, or are integrated into the gold structure. Figure 5.5 seems to support this hypothesis. The discoloration is confined to the edges of the trap–filterboard connection, where the solution cannot be easily mixed and sulfate accretions are to be expected. Even the more extensive area covered by the weaker discoloration of Figure 5.4 could fit into this paradigm. It is probable that the trap was held off-center in the beaker due to being held at the connecting cables, so that different turbulence on either side of the trap is easily possible.

The electroplating was done for a sum of 1 min, which amounts to roughly 2 µm of gold, though that value is encumbered with a large uncertainty due to the inability to guarantee equivalent rates of solvent flow around the trap. The unwieldiness of the trap connected to the filterboard made microscope measurements of the depth impossible. The procedure was stopped because a short of 4Ω appeared between electrodes 114 and 115 on the top chip, as evidenced in Figure 5.6. Luckily, it appeared in an accessible part of the constructed trap, and the short could be removed by applying force via a specialized tool[13]. All other conducting paths were confirmed to be isolated from each other. The broken connection of VIA 17 had not been repaired by that time, but additional electroplating was deemed to be too risky. While the remaining VIAs now were stable enough to withstand the requirements of trap operation, confirmed by low resistances measured from bond pad to electrode tip, electrode 17 and its dependent electrodes had to be connected by another method. We decided to use the same gold wire ball bonding technique we regularly utilize to connect the ion traps to the filterboards, and thus with the voltage supplies. To stabilize the trap while the bonding machine exerts pressure onto the surface, a setup was conceived which used a spare piece of spacer material guided into the trap

---

[13] An acupuncture needle was repeatedly scratched across the isolation groove until the short disappeared

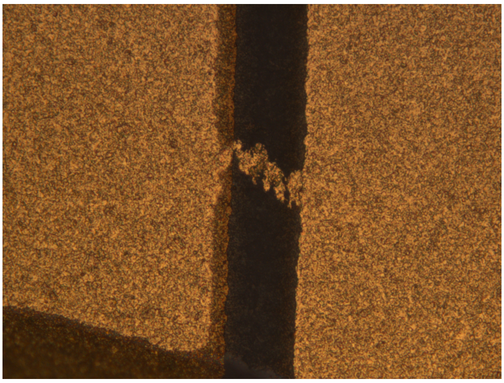

Figure 5.6: Short between electrodes 114 and 115 on the top layer of Fibertrap V2, which appeared after electroplating.

between the bottom and the top layer, with the same orientation as the actual spacer layer (Figure 5.7). The two bonds were set onto the Fibertrap V2, one from electrode 12 to the VIA backplane of electrodes 17, 22, 27 and 32, and one from that backplane to the tip of electrode 17, as can be seen in Figure 5.8. This bypasses the broken VIA 17 completely. Altogether, both repair procedures managed to significantly reduce the resistances of the conducting paths, which can be taken as evidence of thicker gold layers and higher survivability of weak joints against high currents. The old and new resistances are contrasted in Figure 5.9. In general, resistances of $\leq 10\,\Omega$ up to $\simeq 50\,\Omega$ are reduced to resistances of $\simeq 7\,\Omega$ after the repair. A view of the repaired cavity-trap-system can be seen in Figure 5.10.

Because the insides of the trap surface could not be plated, and because the plating thickness of the VIAs could not be verified in the setup, upper bounds for the RF voltage were set in place during trap operation. Due to the failure of the VIA connections at $V_{\mathrm{rf}}^{\mathrm{pp}} = 180\,\mathrm{V}$, the maximum peak-peak RF voltage was set to $V_{\mathrm{rf}}^{\mathrm{pp}} = 160\,\mathrm{V}$. Equation 2.6 shows that the crucial stability parameter $\boldsymbol{q}$ is linearly dependent on the amplitude $U = V_{\mathrm{rf}}^{\mathrm{pp}}/2$ of the RF voltage. This lead to difficult transport operations and short trapping times of ions within the trap for the safety voltages $V_{\mathrm{rf}}^{\mathrm{pp}} \leq 160\,\mathrm{V}$. Clearly, the ratio of the parameters $\boldsymbol{a}$ and $\boldsymbol{q}$ was no longer in a very stable trapping regime. To keep the trapping parameters a and q constant, in order to be in a roughly equivalent regime of trapping ions, the trap drive frequency Ω_{rf} needed to be reduced equivalently. Comparing the parameters of operation of Fibertrap V1, Ω_1 and $V_{\mathrm{rf},1}^{\mathrm{pp}}$ (given in subsection 5.6.1), with the new maximum $V_{\mathrm{rf},2}^{\mathrm{pp}}$ value, the new trap drive

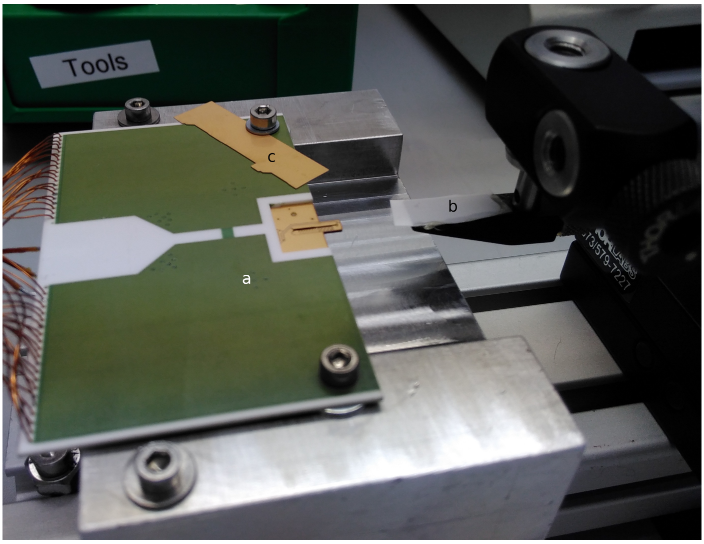

Figure 5.7: Repair bonding setup for Fibertrap V2. a) Filterboard and fibertrap, with the broken VIA for electrode 17 exposed. b) Spacer to stabilize the extrusion of Fibertrap V2 against the pressure exerted by the bonding machine, so that it does not break off. c) Broken piece of gold-coated wafer used to un-stick the bonding tip in case the gold ball gets caught in it. This avoids extraneous bonds on the trap itself.

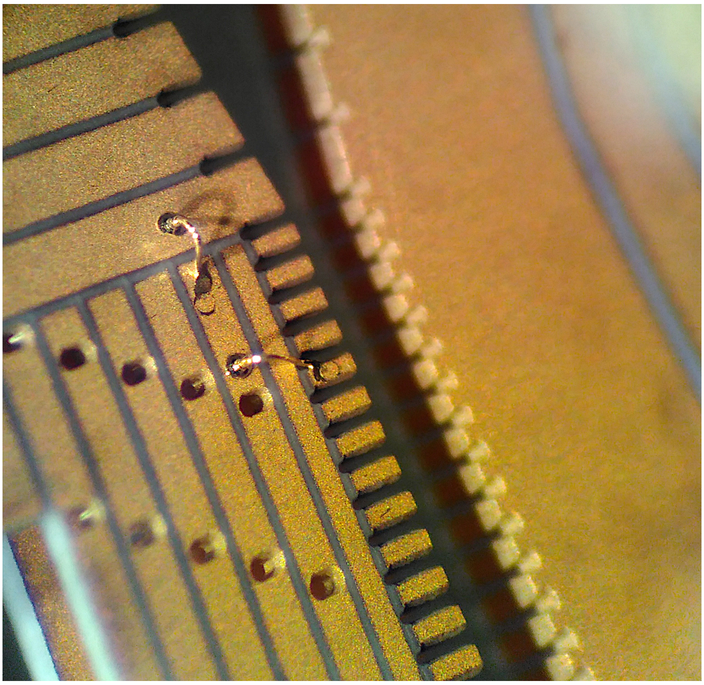

Figure 5.8: Fibertrap V2 with the VIA of electrode 17 repaired by ball bonding, after electroplating. The VIA backplane connecting all 5 VIAs had to be connected to electrode 12, as well as electrode 17 to its VIA backplane.

frequency needed to be reduced to

$$\Omega_2 = \Omega_1 \sqrt{\frac{V_{\mathrm{rf},2}^{\mathrm{pp}}}{V_{\mathrm{rf},1}^{\mathrm{pp}}}} = 12.2\,\mathrm{MHz} \tag{5.7}$$

to achieve an equivalent $\boldsymbol{q}$. The tunable parasitic capacitance included into our helical resonator (see section 2.5) only allowed us to tune the resonance of the resonator-trap system down to 13.6 MHz. While this limit is above the target trap drive frequency, it is close enough to provide stable solutions to the $\boldsymbol{a}$ and $\boldsymbol{q}$ parameter manifold.

The peak-peak RF voltage was slowly increased from $V_{\mathrm{rf}}^{\mathrm{pp}} = 100\,\mathrm{V}$ to $V_{\mathrm{rf}}^{\mathrm{pp}} = 160\mathrm{V}$. The Fibertrap V2 was able to trap ions easily, and transport up to segment 25 was possible by moving the ion through slowly adjusting the target distance, and if necessary the compensations. However, a trapped ion often melted to a hot ion cloud, despite adjusting the Doppler cooling frequency.

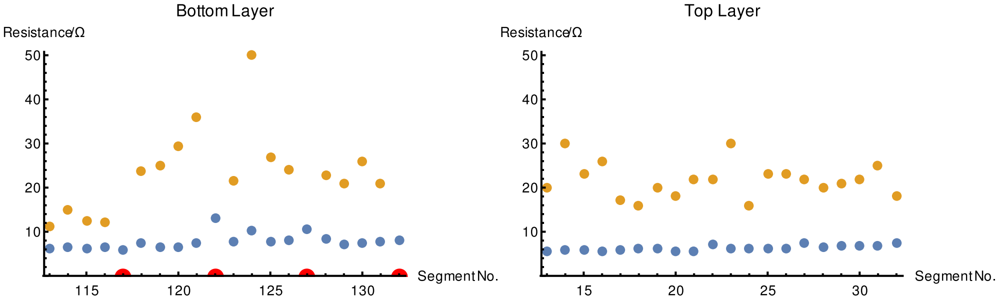

Figure 5.9: Resistances of Fibertrap V2 conducting paths, measured from the bond pads to the electrode tips. **Orange** are the resistances before electroplating, and **red** the electrodes that are completely severed from their bond pad. **Blue** are the resistances after electroplating, and after the broken VIA 17 has been bridged by wire bonds. The fluctuations in the blue graph are most probably due to the fact that we decided not to use excessive pressure on the probe tips. On the one hand, his would guarantee good contact, but could on the other hand damage the sample irreversibly. In tests with expendable pieces, such outliers could usually be corrected for by increasing the probe tip pressure on the object.

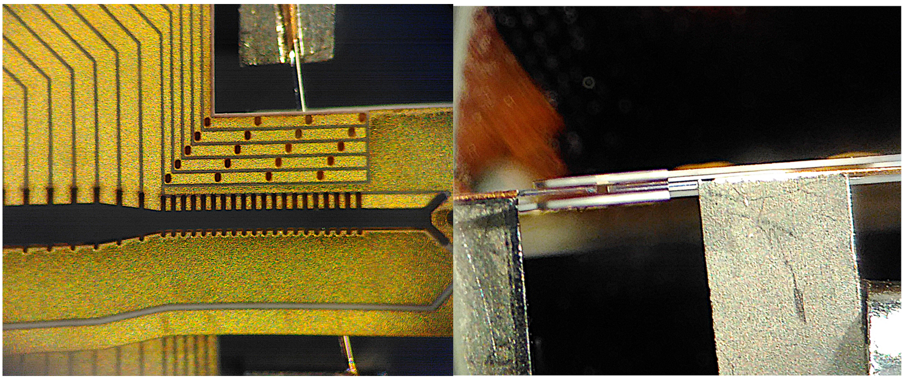

Figure 5.10: Microscope picture of a fiber cavity embedded into Fibertrap V2. The cavity resides around segments $28 - 29$. The cavity holder for the upper fiber intrudes on the left hand picture, including the groove the fiber is glued into. Side view on the right. The loop of the bond repairing the disconnected segment 12 can be discerned on the lower side of the trap, when zooming into the right hand picture.

In addition, the ion often seemed to take up different directional modes of the main harmonic potential's eigenmodes. This was visible by the ion not being an almost circular ellipse on the camera picture, but instead an elongated ellipse which switched directions every so often. Furthermore, the ion transport was volatile and required minute adjustments to position-dependent compensation voltages. We suspect that the repair bonds at electrode 17 were too close to the ion and impacted the stability of the trap negatively by acting as an antenna for the RF voltage. The low trap drive frequency was another added factor. The stability diagram for Paul traps is best for low values of a and q, as described in subsection 2.2.2. The low frequency for Ω_{rf} in this setup meant that the trap parameters may have been close to nonlinear instabilities not captured by the model used, which are unimportant for low a and q values.

5.6.3 Fibertrap V3

To alleviate the VIA problems, Fibertrap V3 was designed with plans incorporating the new knowledge and procedures we had learned in constructing the previous fibertraps. The loading region was reduced to one segment, enough to consistently trap ions. The processor/cavity region is now divided roughly into two distinct regions, the processor region in front of the VIAs, and the cavity region. This allows us to do gate logic in the narrow part of the trap, where transport to and from the cavity need not pass the taper, and where gate speed can be enhanced by higher frequencies of the motional eigenmodes of the ion. The VIAs connecting the DC electrodes, which had been the weak points of the previous design, were enlarged to 90 µm×50 µm, to increase the quality of the evaporated gold layer. Finally, the trap was designed with electroplating in mind from the very beginning. This means the individual chips can be plated in groups of four on a wafer, before being conjoined to an ion trap. Access of the electrogalvanic solution to all parts of each trap chip is easily guaranteed, unlike in the case of Fibertrap V2 in subsection 5.6.2, where a significantly thinner gold layer must be expected for the ion-facing parts of the trap after electroplating than for the outer parts. Trap construction proceeded as described in section 5.3, including electroplating from subsection 5.3.1. The ion trap and the fiber cavity were then combined via an adapted cavity holder by Marcel Salz.

Dimension of Fibertrap V3

The Fibertrap V3 can be partitioned into 4 zones:

- A loading zone of only one electrode width, where the trap slit is 40 % larger than in the other two, for an electrode-electrode distance of 350 µm, in order to reduce stray light while capturing ions. The loading electrode is 140 µm wide.

- A taper zone of three electrodes width connecting the large trap slit with the smaller ones used for gates and cavity interaction. The widths of the three taper electrodes are reduced from the loading width to the processor width linearly with the distance to the ion, so that the feedthrough of segments stays roughly the same.

- A processor zone, spanning segments 5 to 17, which is used for ion cooling, state preparation and detection, and gate operations. This zone already has a trap slit width of 250 µm.

- The same trap slit width of 250 µm applies to the final zone, the cavity zone. This last zone spans the remaining trap up to segment 34. The main purpose of this zone is to enable interaction of the ion with the cavity mode near segment 31. The supporting electrodes are used to shuttle the ion to the cavity.

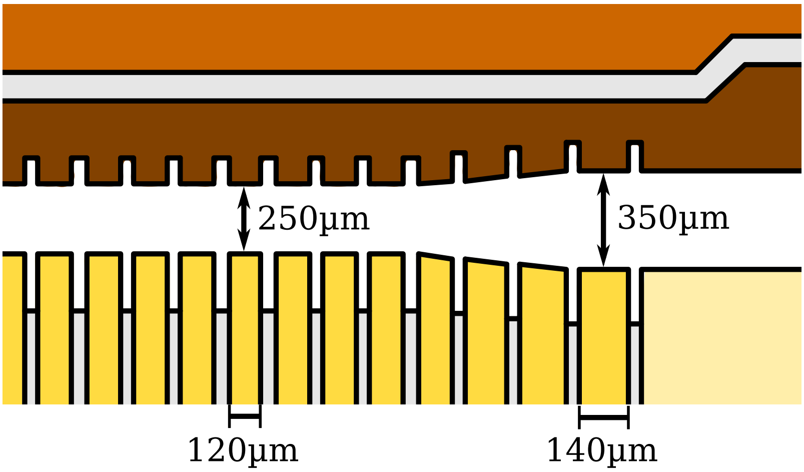

Figure 5.11: Zoomed trap slit of Fibertrap V3 with important dimensions added. The Fibertrap V3 features a very short loading zone of only one segment of 140 µm width, which is placed 350 µm from the opposing electrode. A variable taper of three segments, with electrode widths also tapering down to the electrode width of the processor zone, connects the loading zone with the processor zone. The trap slit is only 250 µm wide, as in the previous designs, and the electrodes are correspondingly reduced in width to 120 µm. Not shown, to the left of the processor zone, lies the cavity zone, which features the same electrode and trap slit dimensions as the processor zone.

The width of the segments is 120 µm in the cavity and computational zone, and the ratio of electrode width to ion distance is kept constant for each taper electrode when moving out to the loading zone, which has an electrode width of 140 µm. This ensures the feed through of each electrode on the potential is relatively constant.

Details of the Electroplating Procedure

A notable difference to the procedure of Kaufmann [Kau17b] is that in our case, we inserted the entire wafer of 4 chips instead of single chips. This was done for ease of use, as the step of sawing off chip ends after the plating isn't necessary with this technique. Thus, the base target on which we electroplate is the gold-coated wafer with cut-out trap chips, which are connected electrically and physically to the wafer by a perforated cut, which allows controlled break-

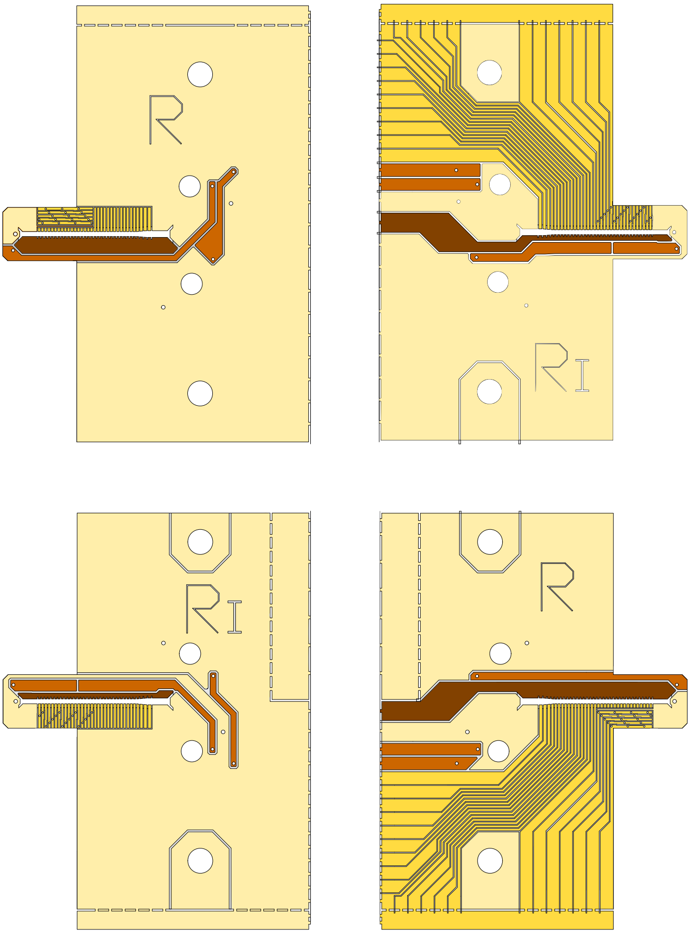

Figure 5.12: The pinnacle of fibertrap development, Fibertrap V3. DC electrodes are colored golden, RF in brown, the two compensation electrodes per chip are orange, and all ground planes are beige. Clockwise from the top left corner: Top layer, ion facing. Top layer, outward facing. Bottom layer, outward facing. Bottom layer, ion facing. The small open circles are VIAs (see subsection 5.2.2) that connect conductors across the layers of one chip. The two large, outer circles are screw holes, the two large inner ones alignment holes.

ing off of the individual chips after electroplating. The wafer must be cleaned thoroughly, with a succession of isopropanol, acetone and DI water. Before this final cleansing step, it has also proven beneficial to quickly dip the wafer into iodine solution (I/IK) to remove any remnants of gold flecks in the isolation trenches between conductors. This "debris" has been known to induce quick, short-inducing growth of gold during electroplating. Dipping the entire wafer into the solution for $15 - 30\,\mathrm{s}$ removed enough of this debris in previous trap designs within this group, and allowed electroplating with satisfactory results [Wol19]. Longer exposure to the iodine starts to expose the ceramic substrate (or more accurately, the titanium adhesive layer) at the corners of the electrode tips. For our design, we have to contend with the added difficulty of the VIAs. Since their connections are already tenuous, it was deemed too risky to expose them to the iodine solution, for fear of disconnecting the VIAs before electroplating.

The VIAs were protected by an epoxy resin[14]. The epoxy was applied as a gel, by combining acetone with crumbs of the epoxy, in a ratio of roughly 1:1, adapted to the viscosity of the gel. The applicator was an acupuncture needle, dipped into the gel, with which a drop could be applied carefully, under a microscope, without scratching the chip surface. An example of a wafer with applied epoxy can be seen in Figure 5.13. Later improvements in the application technique allowed us to apply the protective layer of Crystalbond-acetone gel onto single conducting paths, without blocking the isolation trenches.

After the deposition of the gel, protecting the VIAs and electrode edges from the iodine, the wafer was exposed to the iodine solution. Two different ways of application were used: Firstly, to remove the gold debris from the largest part of a chip's isolation trenches, the epoxy was applied as shown in Figure 5.13, and dipped into a beaker full of 0.8 % iodine in 3 molar KI solution. The exposure times were roughly 30 s, after which the wafer was taken out of the solution and dipped into a beaker of DI water with a small spoonful of Na_2SO_3 added, which neutralizes iodine instantly. The wafer is then dipped into a beaker of pure DI water and rinsed, and checked for further gold debris in the trenches. Secondly, for points in which this method failed to prevent gold outgrowths in the isolation trenches, as well as for the trenches blocked from cleansing iodine, near the VIAs, the epoxy was applied more carefully. As visible in Figure 5.14, the electrodes were treated with epoxy in the manner described above, leaving the isolation trenches free. Care was taken to never expose a dangerous amount of electrode, rather to repeat the application of epoxy and iodine multiple times. Then, a droplet of concentrated 10 % iodine solution in 3 M KI was dropped

---

[14] Crystalbond™ Type 509

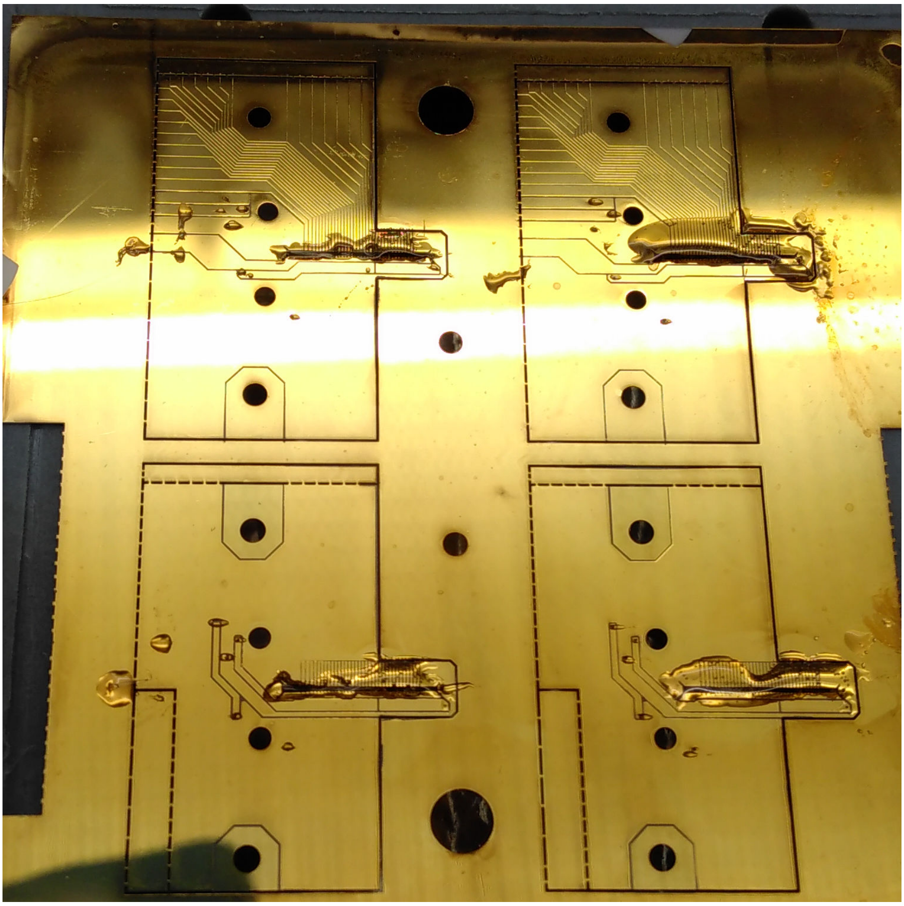

Figure 5.13: VIAs and electrode tips of a Fibertrap V3 wafer protected from ionide by crystalbond 504 epoxy. Due to the difficulty of covering only a single VIA, the isolation trenches of the surrounding conducting paths are also protected from iodine. This lead to difficulties when electroplating, which were constrained to the VIA region, and had to be dealt with afterwards.

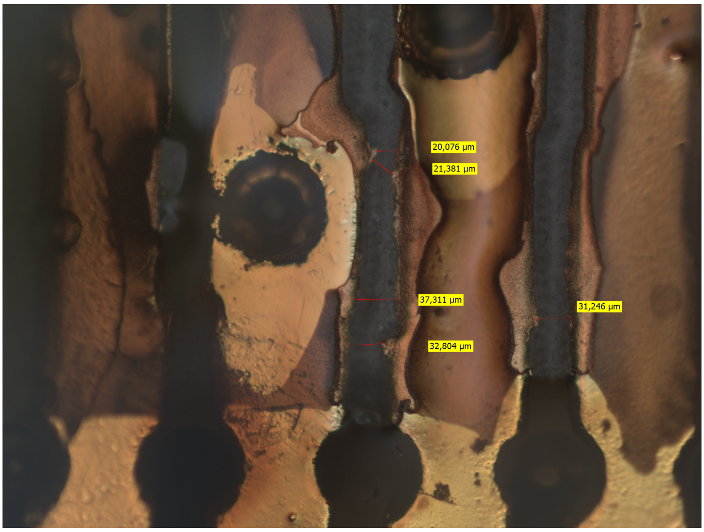

Figure 5.14: Epoxy applied to individual electrodes around VIAs, leaving the isolation trenches free to be cleansed with a drop of concentrated iodine solution to remove the gold. The middle and left trench are to be cleansed in this case. Note that the electrode teeth in the lower fourth of the picture, and the gaps between them, are also protected from iodine to avoid removing gold from sides of the extrusions.

onto the protected region, and kept there for 30 s up to 10 min, depending on the severity of the gold contamination. This droplet was then neutralized by a short rinse with the Na_2SO_3-water described above, applied through a 3 mL syringe. Finally, the entire wafer was thoroughly rinsed in DI water to remove any remnants of the salt.

At the end of this process, the two chips used had a thickness, measured under a microscope, of 7.2(10) µm and 7.5(10) µm, respectively, which corresponds to a gold use of 0.15(2) g on the trap. The errors are mainly due to the inaccuracy of the method of using the microscope's focus to evaluate the thickness of the gold layer.

Segment	top layer	bottom layer
base	1.9	0.4
1	0.6	0.4
2	0.7	0.6
3	1.0	0.9
4	1.1	0.8
5	2.1	0.8
6	1.1	0.8
7	1.7	0.9
8	1.7	0.9
9	2.1	0.9
10	1.9	0.9
11	1.6	1.0
12	1.6	0.9
13	1.6	1.2
14	2.1	0.9
15	1.6	0.9
16	0.6	0.5
17	0.6	0.6
18	1.6	0.6
19	1.4	0.8
20	1.0	0.8
21	0.9	0.8
22	1.0	0.9
23	1.1	0.7
24	1.4	0.9
25	1.6	1.1
26	1.1	1.0
27	1.0	0.9
28	1.4	0.8
29	1.4	1.0
30	0.9	0.9
31	1.0	1.0
32	1.1	1.1
33	0.8	0.9
34	1.5	1.4

Table 5.1: Resistances of the conducting paths of the ion trap top and bottom layers. The low resistances point to thicker layers of conducting gold, and a strongly reduced vulnerability to damage through radiofrequency pickup currents for the VIAs.

6 Trap Operation

6.1 Operational Parameters

The Fibertrap V3 was operated at the comparatively high pressure of $3 - 5 \times 10^{-9}$ mBar. As leak detection did not return any leaks at the flanges, the most probable culprit is our inability to bake out the fiber setup, as described in section 5.5. This did not lead to problems while doing experiments, the ion retention times were on the order of 20 minutes for the operating parameters used. Ion trapping can be achieved in a few seconds. To reduce stray light from the ionizing lasers, however, their power has been reduced in operation to achieve loading rates of roughly 30 s.

With the trap drive frequency $\Omega_{\mathrm{rf}} = 2\pi \times 33.331\,\mathrm{MHz}$, stable trapping was achieved from $U_{\mathrm{rf}} = 100\,\mathrm{V_{pp}}$ up to $U_{\mathrm{rf}} = 250\,\mathrm{V_{pp}}$, with V_{DC} for the trapping segment ranging from $-0.5\,\mathrm{V}$ to $-7\,\mathrm{V}$. Transport to the cavity region was done with $U_{\mathrm{rf}} = 225\,\mathrm{V_{pp}}$ and $V_{DC} = -2\,\mathrm{V}$. Using the simulations from subsection 2.2.2, we can analyze the curvature of the potentials along the trap axis and along the two radial axes, defined by the edges of the RF electrodes and of the DC electrodes, and obtain the parameters α_i and $\widetilde{\alpha}_i$ from Equation 2.6. These parameters, as well as the stability parameters a and q, and the trap frequencies following from them, are shown in Table 6.1. The Laplace equation, Equation 2.2, is fulfilled by these parameters to within 0.1‰, due to numerical errors in the simulation.

In Figure 6.1 and Figure 6.2, two 729 nm laser spectra with different resolution and pulse times are shown. It is possible to identify $\omega_{\mathrm{z}} = \omega_{\mathrm{ax}} = 0.73\,\mathrm{MHz}$ and $\omega_{\mathrm{x}} = 2.9\,\mathrm{MHz}$ in the figures.

6.2 Transporting Ions along the Trap

In order to ascertain working transport operations in the absence of ion interaction with the cavity, a number of procedures to be checked. The trap is too large to verify transport directly on the CCD camera for long distances without considerable difficulties, due to both image magnification and laser position. Thus, we use multiple smaller steps to confirm the correct function of

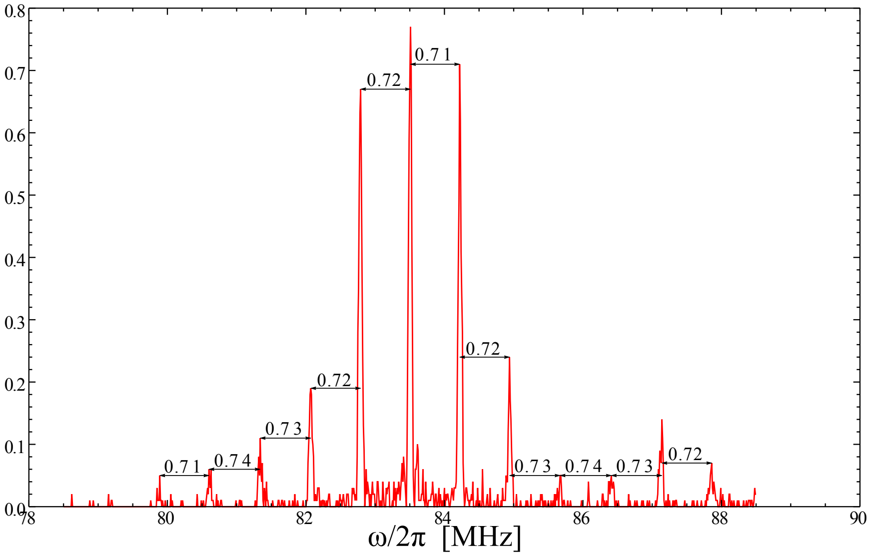

Figure 6.1: 729 nm spectroscopy of the ion. The sidebands correspond well to n-th axial sidebands of the carrier, which are calculated to be offset by 0.67 MHz according to Table 6.1 .

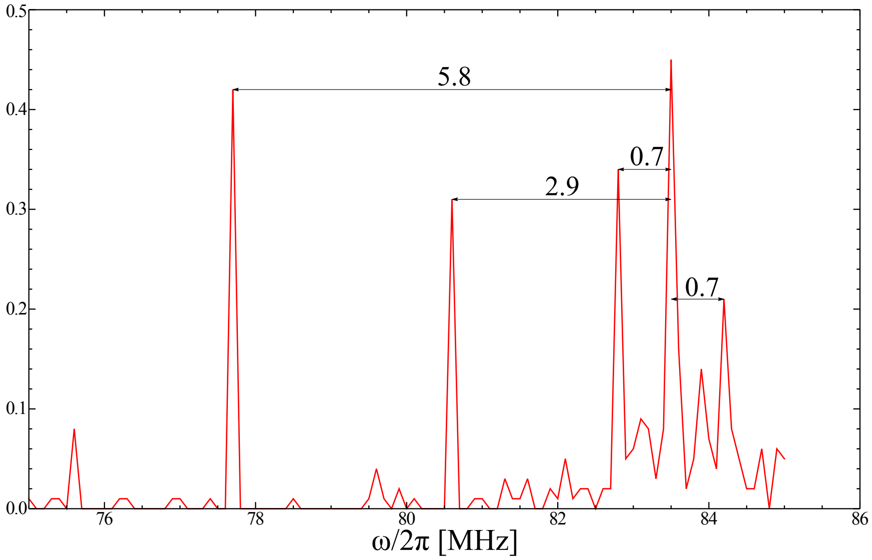

Figure 6.2: Same as Figure 6.1, but with a lower resolution and longer 729 nm laser pulse times. The two highlighted peaks at −2.9 MHz and −5.8 MHz correspond roughly to one of the radial frequencies calculated in Table 6.1, though the resolution is too low to depict both.

	$i = x$	$i = y$	$i = z$
α_i [m^{-2}]	-7.35×10^6	-1.47×10^7	-7.33×10^6
$\widetilde{\alpha}_i$ [m^{-2}]	1.63×10^7	-1.63×10^7	334
a_i	0.00162	−0.00323	0.00161
q_i	0.224	−0.224	-4.60×10^{-6}
β_i	0.163	0.148	0.0402
$\omega_i/2\pi$ [MHz]	2.72	2.46	0.670

Table 6.1: Table of important trap paramters. $\widehat{e}_x$ is a unit vector spanning the tips of opposing DC electrodes. $\widehat{e}_y$ is oriented in the direction of the tips of opposing RF electrodes, and $\widehat{e}_z$ lies along the trap axis. Voltages of $V_{\mathrm{DC}} = -1\,\mathrm{V}$ and $U_{\mathrm{rf}} = 225\,\mathrm{V_{pp}}$ were assumed, at $\Omega_{\mathrm{rf}} = 33.331\,\mathrm{MHz}$.

the elements of transport.

Preparatory Transports

1. Short-distance transports are performed, which leave the ion in the focus of the laser. This proves the correct functioning of the transport sequence on a basic level. This test works for a maximum distance of ≈ 100 µm.

2. Manual transport to a segment is performed. Manual transport implies that the usual transport sequence is performed, but the completion is controlled not by timed sequences (see subsection 2.2.3), but by scrolling through a parameter with the mouse wheel. This allows us to move the ion to the border of visibility in either edge of the camera image or of laser focus, and readjust the positions of all beams and the camera as required to continue. Using this technique, we have verified working transport from segment 1 to segment 6, over a distance of 850 µm. Additionally, we could verify with this procedure that smooth transport does not require extensive adjustment of compensation parameters and RF trapping voltages, even through the changing trapping parameters of the taper. The DC voltage is automatically adjusted by the transport sequence, which can also be seen in Figure 6.3 for the remote loading sequence of the next paragraph.

3. We have implemented remote loading of ions in the trap. Ions can be ionized at segment 1 and transported to segment 5, 750 µm away, where the usual cooling and initialization cycle starts. This is achieved by fo-

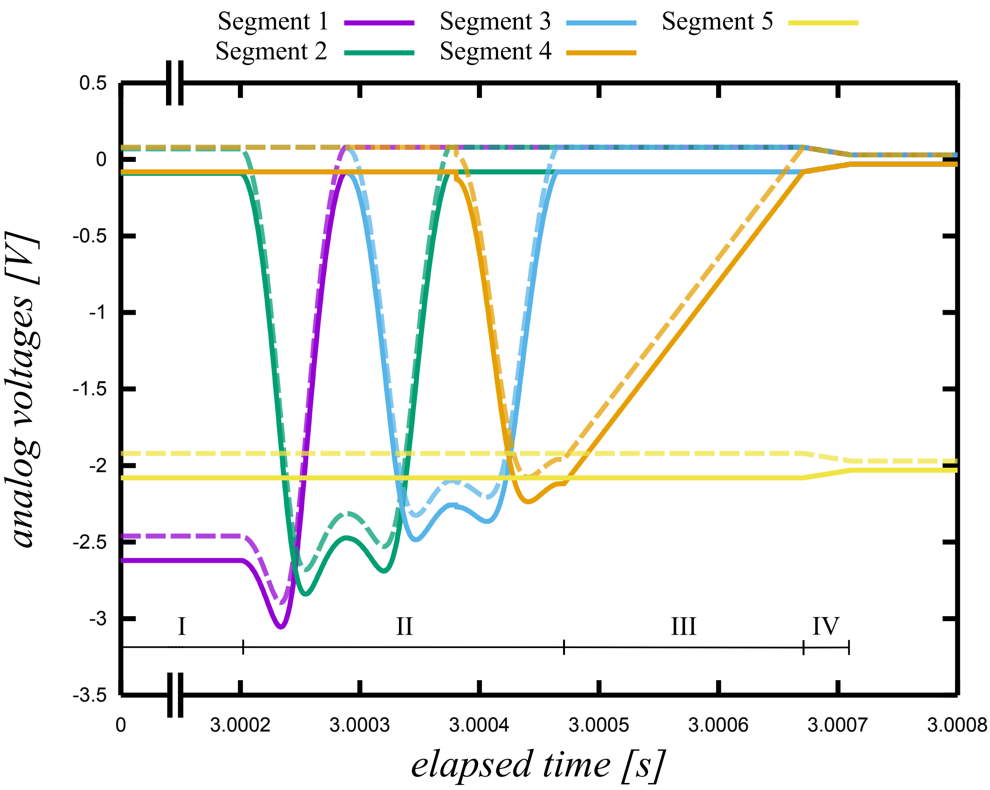

Figure 6.3: Analog voltages of the remote loading sequence from segment 1 to segment 5. Solid/dashed lines are the respective voltages of the two electrodes making up one segment, separated by the DC compensation voltage. In phase *I*, a trapping well at segment 1, and one at segment 5, coexist in the trap, and the photoioniziation lasers are set to trap ions at segment 1. After a set time, slightly more than 3 s in the graph, phase *II* is initialized, and a sequence transports any trapped ions from segment 1 to segment 4, creating a broad trapping well between segments 4 and 5. Finally, in phases *III* and *IV*, the trapping voltage of segment 4 as well as the compensation voltage are slowly scaled to their respective target values, so that any ions are now trapped at segment 5. If no ion has been trapped, the process starts over by creating a trapping well at segment 1.

cusing the photoion lasers, so that the usual trapping at segment 1 shows maximum rates. The analog voltages set during the remote load sequence

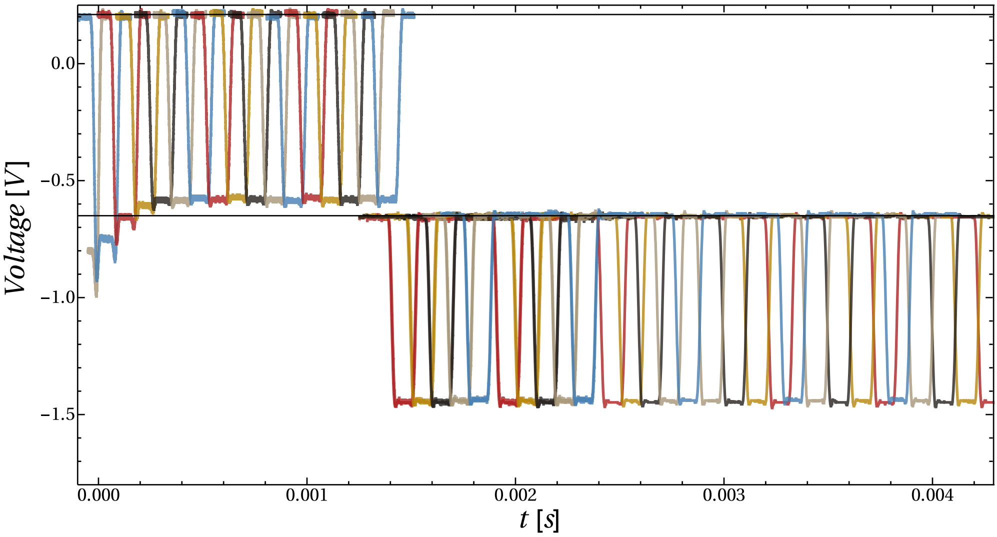

Figure 6.4: Measured voltages applied to the top electrodes during transport to segment 32 and back. Return trip is only partly shown. The gray ruler provides segment numbers reached at a certain point. Black grid lines mark the DC compensation voltages for the load and the cavity half of the trap, 0.21 V and −0.65 V, respectively. Both offset voltage and wait time at the target segment have been turned off for the purpose of this demonstration. Equal coloring in the cavity region electrodes denotes VIA connections, while in the loading region the coloring is merely a guide to the eyes.

can be seen in Figure 6.3. After a set time of trying to capture an ion at segment 1 (I), usually a few seconds, a transport is performed from that segment to segment 4, creating a broad potential well between the two segments (II). In phases (III) and (IV), the voltage of segment 4 and the DC compensation voltage are smoothly adjusted to create a trapping well only at segment 5, with the requested trapping voltage. The last step, (IV), is required since the optimal remote loading rate compensation differs from the optimally micromotion-compensated value at segment 5. If at least one ion can now be seen on camera, the remote loading sequence is stopped. Otherwise, segment 1 is set to the trapping voltage (in Figure 6.3 it is slightly below 2.5 V, for example), and the whole sequence begins anew.

4. To verify the correct operation of the MAWG (see section 2.5) for seg-

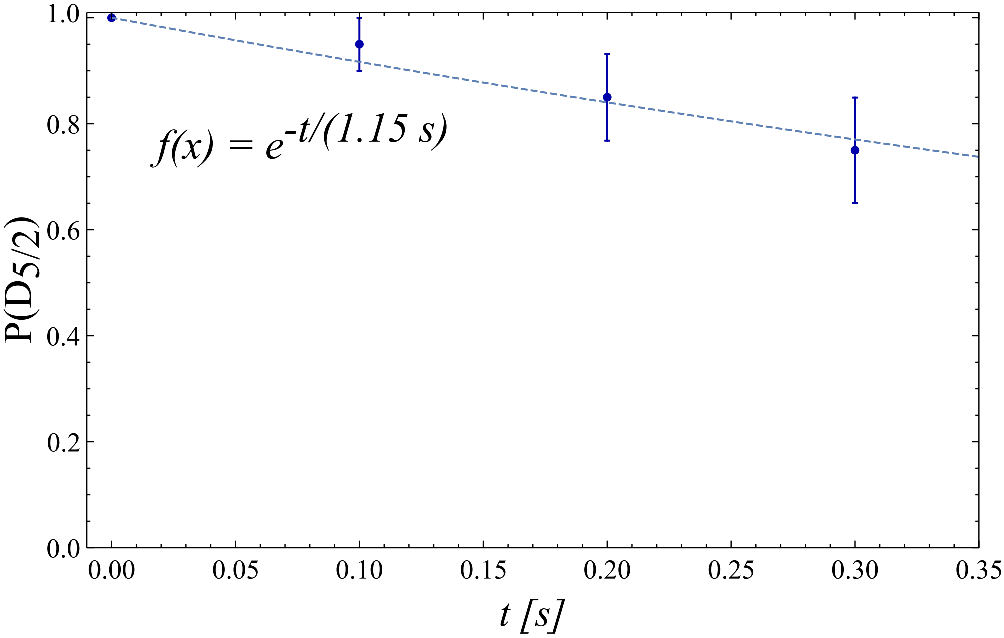

Figure 6.5: Fidelity of the $|D_{5/2}\rangle$ state for short transport operations. Shown is $P(D_{5/2})$ vs time waited at the target segment for a two-segment transport through the taper. The dashed line shows an exponential decay $f(x)$ fitted to the data, with a lifetime of $\tau = 1.15(11)\,\mathrm{s}$.

ments outside of the camera and laser interaction region, the output of the MAWG channels feeding the electrodes was checked with an oscilloscope. Measured voltages applied to segments during an example transport operation are shown in Figure 6.4. Pictured is the voltage applied to the top layer DC electrodes for a transport with voltage $V_{\mathrm{DC}}^{1} = -1\,\mathrm{V}$ starting at segment 1, with a loading zone compensation of $V_{\mathrm{comp}}^{\mathrm{load}} = 0.21\,\mathrm{V}$ and a cavity zone compensation of $V_{\mathrm{comp}}^{\mathrm{cav}} = -0.65\,\mathrm{V}$. The voltages are chosen so that the axial trap frequency is kept stable throughout the transport, at $\omega_{ax} = 670\,\mathrm{kHz}$ (For the measured values, see Figure 6.1). This measurement proved that all electrodes are driven by the MAWG outputs, and no electronics hardware failure occurred. To control for hardware failure during the next experiments, the same measurement was performed both before and after the cavity interaction runs had been done.

5. The fidelity of the $|D_{5/2}\rangle$ state was measured to be $F_{D_{5/2}} = 1.00(4)$. For short transport operations, the fidelity stays close to 1 for the time scales

of typical transports, and decays with $\tau = 1.15(11)\,\mathrm{s}$, in agreement with the natural lifetime of $\tau^{\mathrm{lit}} = 1.17\,\mathrm{s}$ (see Figure 6.5). The high fidelity of the $\left|D_{5/2}\right\rangle$ state agree with the results from Kaufmann et al. [Kau18].

Transports into the Cavity Region

Finally, an attempt was made to prove that the ion interacts with the cavity. The ion was pumped into $\left|D_{5/2}\right\rangle$ by using a beam of 393 nm light to excite the ground state to $\left|P_{3/2}\right\rangle$, with only the 866 nm repumper active. While this method is entirely unsuited for coherent dynamics, as the transition $\left|P_{3/2}\right\rangle \rightarrow \left|D_{5/2}\right\rangle$ happens by spontaneous decay, it has the benefit of comparative simplicity: The $|S\rangle \rightarrow |P\rangle$ transition is broad and easily found, the laser can excite both spin states, and the strength of the transition means that comparatively low laser intensities are required to drive it. Due to a defective fiber, the power of the 393 nm laser at the ion trap fluctuated strongly, so a very long interaction time of 100 µs was chosen to ensure good fidelity despite the error.

For the tests to search for an ion-cavity interaction, the cavity length was scanned over the resonance of the 854 nm laser coupled into it. The scan was performed by applying a saw tooth voltage (approximately 50 mV amplitude at 50 Hz) to the cavity piezo. The reflection signal on a photodiode shows a dip of roughly 2 % depth on resonance, with a FWHM of $\sigma_t = 42.5\,\mu\mathrm{s}$. A full period features two resonances, one per direction of the saw tooth. As we have chosen a dwell time of 100 ms for the ion in the cavity region, it is guaranteed to rest at that position long enough to experience the cavity field for at least nine resonances, if within the confines of the cavity mode. This results in an interaction time of

$$t_{\mathrm{I}} = 2 \times 50\,\mathrm{Hz} \times 100\,\mathrm{ms} \times 42.5\,\mu\mathrm{s} = 425\,\mu\mathrm{s}\ . \tag{6.1}$$

The experimental runs were susceptible to the application of correct compensation voltages. While the compensation applied to the DC electrodes, and that to the RF compensation electrodes, where comparatively constant, a general voltage offset applied to the DC electrodes proved important to adjust, and changed with continued experimental runs. The value fluctuated between $-1.5\,\mathrm{V}$ and a maximum of $-7\,\mathrm{V}$. Since this offset has the effect of shifting the ground reference voltage for the trap, it can adjust for divergences of the ground due to, e.g., patch charges. We will come back to this fact in subsection 6.3.2, where we try to find models explaining the lack of clear cavity interaction.

Software issues and the limited time the experiment could be run forced us to log the data manually. Because of this, each experimental run took a long

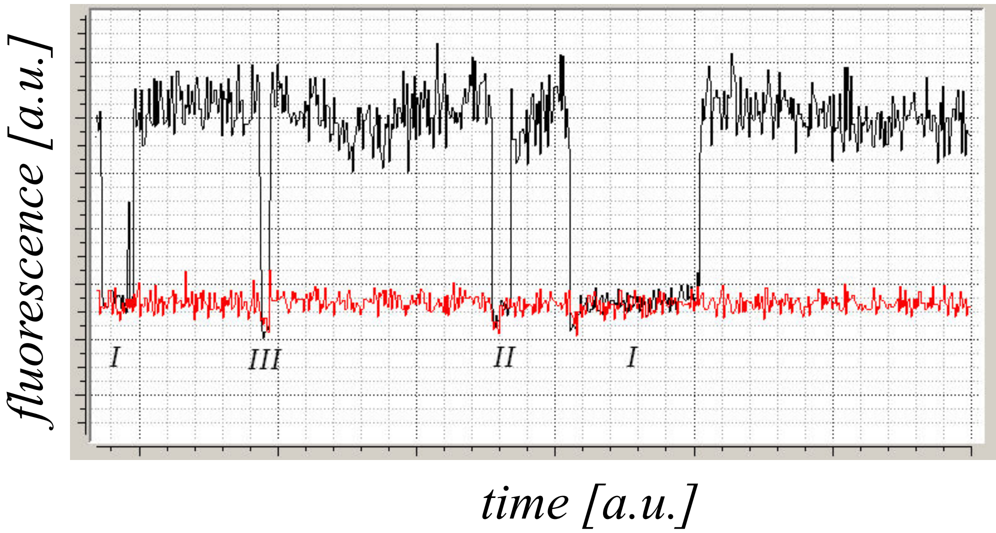

Figure 6.6: Fluorescence count vs time for four ion-cavity interaction experiment runs. Both axes have arbitrary units. In red, a background fluorescence is recorded, while black shows the fluorescence count of the transported ion. Each drop in fluorescence begins after a manually started sequence which pumps the ion into $\left|D_{5/2}\right\rangle$, transports it from the trapping segment towards a position near segment 31, and back for measurement. The different events are categorized according to the duration of the fluorescence drop. The marker *I* denotes an ion counted as dark, *II* an inconclusive result, and *III* was counted as bright ion, due to being of $\approx 400\,\mathrm{ms}$ duration, which corresponds roughly to the preparation and execution time required.

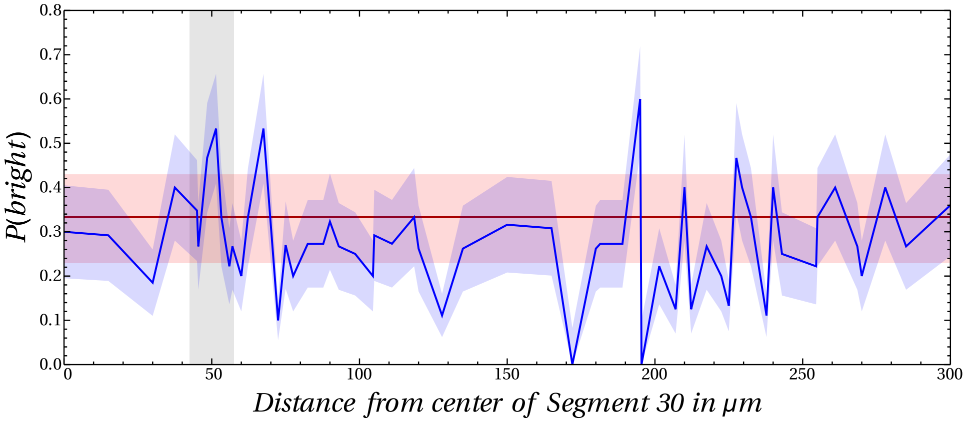

Figure 6.7: Probability of $|D_{5/2}\rangle$ decay into $|S_{1/2}\rangle$ for transport towards the approximate cavity region. On the x-axis, distance along axis past the position of segment 30 is plotted. The blue line depicts the probability for a bright ion. The red line is the average background from ion decay, when the transport is done but no 854 nm light is coupled into the cavity. The gray bar depicts the position of the cavity center ±7.5 µm zone described at the end of subsection 6.3.1. Error bars are shown as transparent underlay in the respective colors, and calculated via the binomial error probability. The high occurrence of very low probabilities of a bright ion are due to later runs of the experiment being stopped as soon as it was clear the background could not be overtaken with 15 experimental shots.

time to complete, and statistical errors are up to 10%. Figure 6.6 shows the raw fluorescence data of four experimental runs and their classification. The fluorescence dip of marker *III* corresponds to roughly 400 ms of dark time, and the inconclusive result of marker *II* to roughly 600 ms.

The results of this experiment are depicted in Figure 6.7. The background of $P(\text{bright}|\text{Cavity off}) = 0.33(11)$ fits well to the time resolution of $\delta t = 400\,\text{ms}$ described in Figure 6.6, as the expected fidelity of the dark state after 400 ms is $F(\text{dark}) = 0.71$. As can be seen, the results show no clear peak. Due to the extreme spatial sharpness of the cavity interaction zone, and the good fidelity of transport in the $|S_{1/2}\rangle$ state, we expect a distance corresponding to a cavity interaction to reach probabilities far closer to 1. For example, in the expected cavity zone around $50 \pm 7.5\,\mu\text{m}$, the average probability of an interaction is $P(\text{bright}) = 0.35(11)$, a negligible difference to the background of 0.33(11).

6.3 Models Explaining the Absence of Ion-Cavity Interaction

In this section, we present two models, which we studied theoretically in order to aid us in restricting the possible reasons for the absence of ion-cavity interaction. The calculations are used to outlay the challenges in integrating a fiber-based cavity in a Paul trap, and are helpful in understanding the improvements and parameter regimes required. It is important to note that these models are meant to be plausible explanations for the lack of cavity interaction, as the quantitative analysis must needs be relegated to the realm of additional research.

6.3.1 Is the Light Frequency in the Cavity Resonant to the Ionic Transition?

The transport operations into the cavity showed long Doppler recooling times on return of the ion, as shown in Figure 6.6. These imply a high excitation of the ion during transport, with possible candidates at fault for this being coherent excitation due to non-optimized transport parameters and heating induced by varying patch charges, or RF-induced dipole moments, on the cavity fibers. Doppler recool times have been used to estimate the excitation energy, e.g., in Wesenberg et al. [Wes07] or Huber et al. [Hub08], where it was also shown that the spectral spread of the wave function due to instantaneous Doppler shifts of a harmonic oscillator can severely reduce the interaction of a trapped ion with a light field. Thus, in this subsection, we proceed in two parts: initially, we use the resolution of the fluorescence count of 0.4 s as a worst-case scenario to estimate the ionic wave packet excitation whereupon we use this worst-case estimation to compare it with the spectral width of the power saturated cavity field for the minimal power used in section 6.2, $P_{\mathrm{cavity}} = 1.7\,\mu\mathrm{W}$.

The first value we require is the saturation intensity for the $|S_{1/2}\rangle \rightarrow |P_{3/2}\rangle$ transition. With a transition dipole moment $d_{397} = 1.76 \times 10^{-29}\,\mathrm{Cm}$, and the natural linewidth $\gamma_{397} = 2\pi \times 21.57\,\mathrm{MHz}$ [Jin93], the saturation intensity turns out to be

$$I_{\mathrm{S}}^{397} = \frac{c\epsilon_0}{2}\frac{\hbar^2\gamma_{397}^2}{d_{397}^2} = 904\,\frac{\mathrm{W}}{\mathrm{m}^2}\ . \tag{6.2}$$

For a beam waist of $w = 25\,\mu\mathrm{m}$ radius, this results in a laser power of

$$P_S = \pi w^2 I_{\mathrm{S}}^{397} = 1.8\,\mu\mathrm{W} \tag{6.3}$$

in front of the vacuum chamber for saturation. During the transport experiments, the Doppler power was $P_{397} = 35\,\mu\mathrm{W}$, leading to a saturation parameter

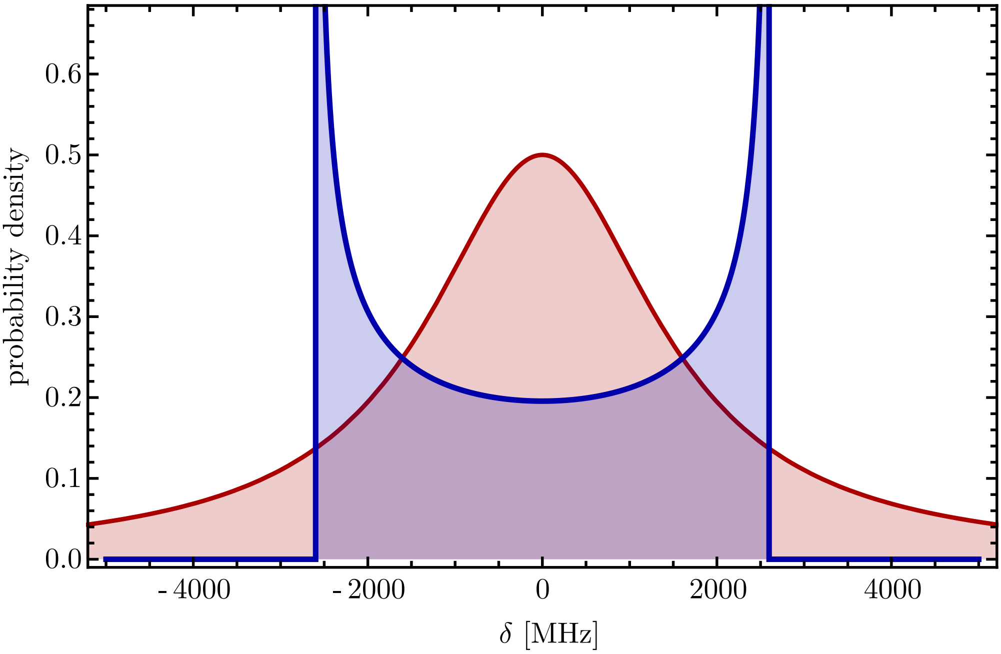

Figure 6.8: Spectral overlap of ion wave function and cavity field. The x-axis shows the detuning δ from resonance, in MHz, which is plotted versus the following probabilities: The blue curve is the spectral probability density of the ion due to Doppler shifts of a thermal harmonic oscillator. The temperature of 300 K was estimated from Doppler recooling times, as explained in the text. The red curve is the saturation-broadened excited state probability density for the cavity field at an input power of 1.7 µW.

$s = I/I_S \approx 20$. To continue the discussion, we will to take a moment to introduce the rescaled energies used in Equations 6a-d of Wesenberg et al.[Wes07], in order to facilitate the comparison with literature. These are

$$\begin{aligned} \epsilon &= E/E_0 \ , \\ E_0 &= \frac{\hbar\gamma}{2}\sqrt{1+s} \ , \\ \delta &= \hbar\Delta/E_0 \\ r &= \frac{(\hbar k)^2}{2m}/E_0 \ , \\ \tau &= t/t_0 \ , \\ t_0 &= \left(\gamma\frac{s/2}{1+s}\right)^{-1} \ , \end{aligned} \tag{6.4}$$

where the energy ϵ, the detuning shift δ, and the recoil energy r have been rescaled by E_0, half the power-broadened linewidth. The time scale t_0 for the rescaled time τ is the power-broadened resonant scattering rate. For a Fock state, i.e., a simple harmonic oscillator, the rescaled, instantaneous Doppler shift $\delta_D = \hbar\Delta_D/E_0$ has a maximum value of $\delta_M = 2\sqrt{\epsilon r}$, and is distributed according to

$$P_D(\delta_M;\delta_D) = \begin{cases} \frac{1}{\pi}\frac{1}{\sqrt{\delta_M^2-\delta_D^2}} & \text{if } |\delta_D| < \delta_M \\ 0 & \text{otherwise} \end{cases} \ . \tag{6.5}$$

If, as is true in this case, the energy is large, $\epsilon \gg (1+\delta^2)/r$, the resulting rescaled energy as a function of the time is well approximated by

$$\epsilon(t) = \left(\epsilon_0^{3/2} + \frac{3}{4}\frac{\delta\, t}{t_0\sqrt{r}}\right)^{2/3} \ . \tag{6.6}$$

The initial energy can then be recuperated by solving $\epsilon(0.4\,\mathrm{s}) = 0$ for ϵ_0. Removing the scale from this result is a trivial matter. The energy returned by this model for these parameters is $E(t=0) = 0.11\,\mathrm{eV}$, corresponding to a thermal wavepacket with temperature $T = 1250\,\mathrm{K}$. Given the symmetry of the experiment with regards to the transport to and from the cavity, we thus estimate the ion wavepacket to be similar to a thermal wavepacket of temperature $T_c = T/2 = 300\,\mathrm{K}$[1].

---

[1] At these high excitations, the difference between thermal and coherent wavepackets is irrelevant to the conclusions drawn from this model. In contrast to Wesenberg et al.[Wes07], we can even ignore the thermal (or coherent) averaging of the wave function, but instead

The same model is applied to the interaction of the ion, pumped into the dark $\left|D_{5/2}\right\rangle$ state before transport, with the cavity at segment 31. Here, we can reuse Equation 6.5 by replacing all occurrences of γ_{397} with $\gamma_{854} = 2\pi \times 1.34\,\mathrm{MHz}$ [Jin93], and replacing the saturation parameter of the Doppler beam with that of the cavity. The experimentally measured result is the power of the reflected light returning from the cavity, which shows a power of $P_{\mathrm{ref}} = 34\,\mathrm{nW}$ being coupled into the cavity on resonance. This allows us to recover the intensity present at the center of the cavity, which we will assume for now to be the ion's position, as a best-case scenario. The power inside the cavity, on the other side of the incoupling mirror, is then

$$P_{\mathrm{cav}} = \frac{1}{T + \mathcal{L}/2} P_{\mathrm{ref}} = 179\,\mathrm{\mu W} \tag{6.7}$$

for transmission $T = 50\,\mathrm{ppm}$ and round-trip loss $\mathcal{L} = 280\,\mathrm{ppm}$, as introduced in section 5.1. We require this power P_{cav} to be the integral over the intensity profile of the cavity for each plane of the cavity along its axis. This results in a field distribution function $f(x,y)$, normalized so that the integral of f^2 over the plane $z = 0$ is one,

$$\begin{aligned} f(x,y) &= \pi^{-1/4}\, w^{-1/2}\, e^{-\frac{x^2}{2w^2} - \frac{y^2}{2w^2}} \ , \\ \int_{-\infty}^{\infty}\int_{-\infty}^{\infty} dx\, dy\, f^2(x,y) &\overset{!}{=} 1 \ , \\ I_{\mathrm{cav}} = f^2(0,0)\, P_{\mathrm{cav}} &= 807\,\mathrm{kW/m^2} \ , \\ I_{\mathrm{S}}^{854} &= 5.6\,\mathrm{W/m^2} \ , \\ s = \frac{I_{\mathrm{cav}}}{I_{\mathrm{S}}^{854}} &\approx 144\,000 \ , \end{aligned} \tag{6.8}$$

for a cavity mode waist of w.

The scattering rate is given by

$$\frac{dN}{dt} = \frac{1}{t_0}\frac{dN}{d\tau} = \frac{1}{t_0}\int P_D(\delta_M;\delta_D)\frac{1}{1 + (\delta + \delta_D)^2} d\delta_D = 2.2\,\mathrm{MHz} \ . \tag{6.9}$$

For the interaction time of Equation 6.1, $t_{\mathrm{I}} = 425\,\mathrm{\mu s}$, this results in a probability very close to one of an interaction having taken place. Clearly, for an ion that reaches the center of the cavity, the spectral spread due to thermal excitation is no limit to the interaction. Since the ionic wavefunction at $T = 300K$ has

---

continue with a Fock state of similar energy.

a considerable spread, an accurate model would have to include the effect of the spatial averaging of the cavity field. The $\sin^2$-structure of the intensity provides us with an additional factor of 1/2 for the scattering rate. This does not change the probability of interaction appreciably.

What, then, about an ion that does not reach the center of the cavity? Clearly, there will be a distance at which a cool ion will have a high probability of interaction, but a hot one will be severely impeded to interact. The inverse of the spatially averaged interaction rate, $(1/2 \times dN/dt)^{-1} = 454\,\mathrm{ns}$, is roughly a factor of 425 lower than the interaction time. In order to reach a cavity field with an intensity no higher than 1/425 times the intensity in the center of the cavity, the ion may not get closer than 2.0 µm to the center. The maximum step of Figure 6.7 is 15 µm, so the highest possible distance to a cavity center is 7.5 µm. The spatial resolution of the transport into cavity experiment is larger than the resolution required to ensure high interaction probability. At a distance of 7.5 µm, the averaged intensity drops to half the value at 2 µm. Taking the background of 0.33 into account, we thus expect a bright count probability of $P(\text{bright}) \geq 0.57$ for at least two data points of Figure 6.7. The data points at 30.23 and 30.43 between segments 30 and 31 in Figure 6.7 lie withing one standard deviation for this value. The gray "cavity center ±7.5 µm" zone around these data points, however, includes more data that is clearly far from the expected value. It follows that reduced interaction of the ion with the cavity field due to Doppler shifts of highly excited thermal or coherent wavefunctions does not suffice to explain the absence of a cavity signal in Figure 6.7.

From the above arguments, we can be sure that if an ion arrives in the cavity region, the D state would be pumped into S. However, the measurement displayed in Figure 6.7 shows not the slightest sign of optical pumping. The only possible reason could be that the ion does not arrive in the cavity region, even though the transport voltages are applied to the segmented electrodes. In the following subsection, we will evaluate another model, so as to help us appraise possible necessary steps to achieve cavity interaction.

6.3.2 Patch Charges on Cavity Fibers

For this model, we suppose that the fiber has some slight surface charges, despite our best efforts to avoid them. As has been measured in Harlander et al. [Har10], patch charges created on dielectrically coated glass surfaces can noticeably influence ion positions in a Paul trap. Starting from the conjecture that this effect is at fault for keeping the ion entirely outside the cavity interaction region, we have analyzed the required charges to achieve this. Two general cases need to be differentiated: A positively charged patch of fiber repulsing the ion, and a negatively charged fiber attracting it. As the effect depends strongly on the exact details of the patch, like position and symmetry between the fibers (though only comparatively weakly on the size of the patch, due to 125 µm being close to the far field for any charge distribution noticeably smaller than 125 µm in diameter), we need to restrict our analysis to a couple of plausible cases. In both attractive and repulsive cases, we will restrict ourselves to symmetric disturbance potentials, that is, the patches appear in equal strength on both fibers, and the ion is not appreciably moved out of the trap center by the disturbance.

In all cases, the disturbing potential is modeled by a Cauchy-Lorenz distribution with a scale parameter of $\sigma = 127\,\mu\mathrm{m}$. This value was obtained by simulating the feedthrough of a hypothetical small conductor at constant potential in the BEMSolver model of the trap, positioned at the center of segment 31. As the full trap model was used, the disturbance potential includes the effects of mirror charges created on all electrodes. The model calculates the effects of the patch charges by searching for a local minimum in a superposition of the axial transport potential, and the disturbing potential created by the patch charges. The potential is changed each simulation step by moving the ion adiabatically along the trap axis in small steps, with each iteration starting the search for a minimum from the previous equilibrium point. Any effects of wavepacket extent, or inertia of the moving ion, can be safely neglected.

Repulsive Potential

Positively charged patches on the fiber mirrors will push the ion away from the cavity center. Unlike the negatively charged case, the repulsion makes the exclusion less susceptible to the exact location on the fibers' tips. To examine this case, we can thus restrict ourselves to a patch on the center of the mirror, as results will not qualitatively differ for different positions. Positively charged patches can appear when laser light, especially the wavelengths 375 nm, 393 nm, 397 nm and 423 nm, create speckles that directly hit the fiber or mirror surface.

The different phases of the repulsive disturbing potential are exemplified by the three figures of Figure 6.10. For $V_d < 80\,\mathrm{mV}$, the disturbance will create a small bump in the ion's potential that leads to accelerated movement through the interaction region, after being held back slightly, right before the region. This is shown for $V_d = 60\,\mathrm{mV}$ in Figure 6.10 a), where a small jump can be seen around the center of the cavity. From $V_d \leq 80\,\mathrm{mV}$ onward (see Figure 6.10 b), the jump is large enough to move the ion completely across the cavity in one step. In this case, movement to segment 32 and back would have the ion cross

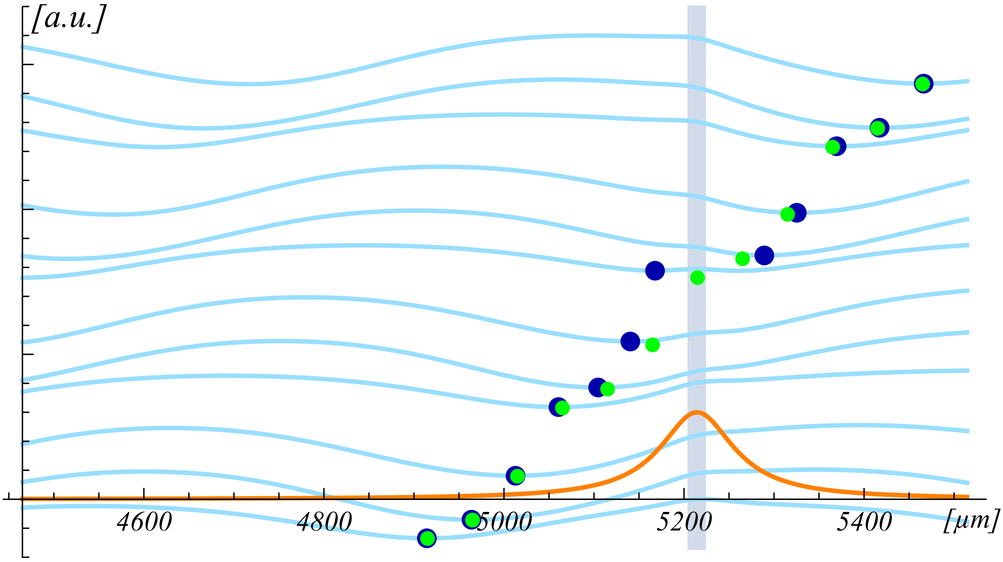

Figure 6.9: Example of the cavity disturbance model with repulsive potential. Plotted are a succession of potentials in arbitrary units (light blue lines) versus the position along the trap axis in µm. For easier visibility, nonphysical parameters have been used. The disturbance potential (orange) has a width of only 50 µm, and is magnified by a factor of 10 for better visibility. Also shown are the intended position of the ion along the trap axis (green dots), i.e., the potential minima without the disturbance, and actual minima including the disturbance (dark blue dots), as well as an estimate for the $1/e$-region of the cavity mode at trap axis (gray underlay). The ion is pushed away from the disturbance while being transported towards the cavity, until the gradient of the transport potential is strong enough to overcome it and the minimum jumps to the other side of the cavity.

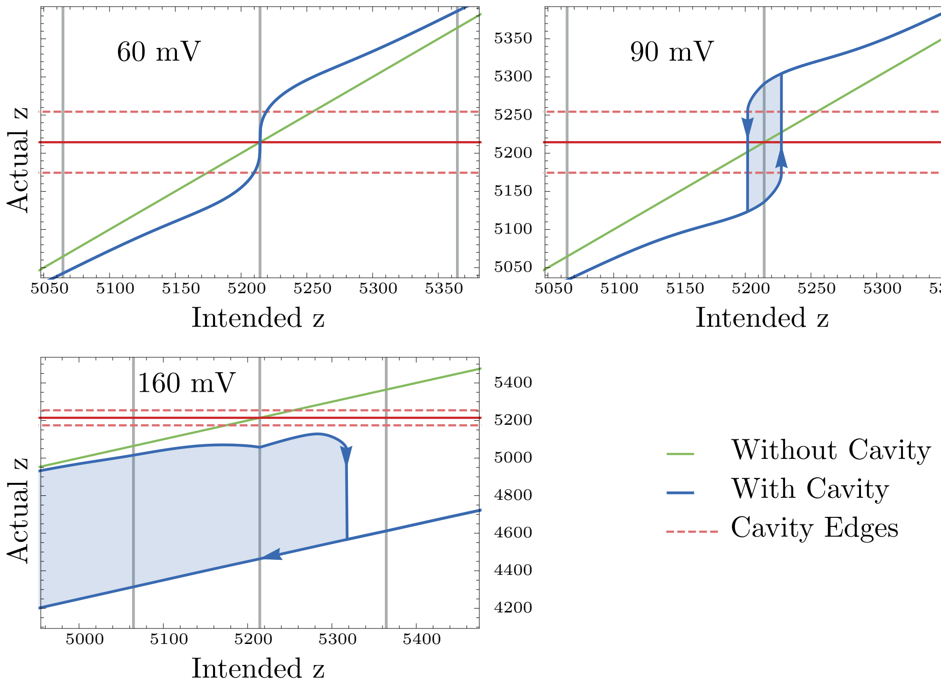

Figure 6.10: Simulated ion positions with vs without a fiber cavity with positive patch charges, located at the center of each fiber, at the position along the trap axis $z = z_{\text{cav}}$. The blue lines describe the ion's actual position in dependence to the intended one. In the case of hysteresis, the two different paths are denoted by arrows, and the avoided area is denoted by the pale blue background. The green line represents the intended path, $y = x$. The red, dashed lines enclose the cavity interaction zone. The black grid line is the position of the cavity on the x-axis, while the gray grid lines mark off shifts of one segment width. The respective strengths for the disturbance potential V_d in a), b) and c) are 60 mV, 90 mV and 160 mV, respectively, at the maximum along the trap axis.

the interaction zone immediately, i.e., so quickly that interaction is improbable. Finally, figure d) shows that once V_d has reached 160 mV, the ion cannot pass the potential, and is simply caught in front of the cavity and pushed back into the previous trapping well, once it is close enough.

Attractive Potential

If the disturbing potential is attractive, it will create an additional potential well along the x-axis which may trap the ion despite the transport function trying to move it further along, or indeed not quite as far, as the disturbance. In order to be an impediment to cavity interaction, this potential well needs to be located outside of the cavity mode along the trap axis, in contrast to the repulsive case. This excludes large patch charge areas, which would automatically tend to keep the ion around the cavity mode center. A small charged area located at the edge of the fiber, however, can lead to the ion being trapped in front of the cavity, or sucked behind the cavity quicker than interaction is possible. The creation of a negatively charged patch is a somewhat more circuitous process than that of a positive one. Since the frequencies used in the experiment, of which the near-UV wavelengths are the most effective, create positively charged patches when shone directly on glass, the speckle must have hit a nearby electrode instead. The resulting free electrons can then conceivably be pushed towards the fibers and settle there, trapped on the isolating surface. This method was deliberately used in Innsbruck to neutralize a positively charged fiber in an ion trap.

An attractive patch on the front edges of the mirror fibers, as seen from the ion approaching from the loading zone, will trap the ion in front of the cavity interaction zone if strong enough. In Figure 6.11, ion path deviations for two different strengths of the disturbance are shown. In figure a), the patch charges create a maximum potential of $V_d = -80\,\mathrm{mV}$ on the trap axis. While the ion's path is distorted, it still travels through the cavity region, albeit slightly delayed. At this disturbance strength, an intended transport to the cavity center would not actually enter the interaction zone. However, transport to one segment past the cavity center (to the first gray line to the right of the black cavity center marker) would still move the ion through the cavity in a slow enough manner, so that the experimental transport distances are guaranteed to keep the ion in the cavity for long enough to interact. With increasing potential, the actual interaction time becomes more and more difficult to achieve, until at a potential of $V_d = -240\,\mathrm{mV}$, pictured in figure b), the ion doesn't enter the interaction zone even if transported to segment 32, or indeed at all.

For a negative patch charge at the far side of the cavity, at $z = z_{cav} + 62.5\,\mathrm{\mu m}$, the distorted ion movement is depicted in Figure 6.12. Figure a) shows a

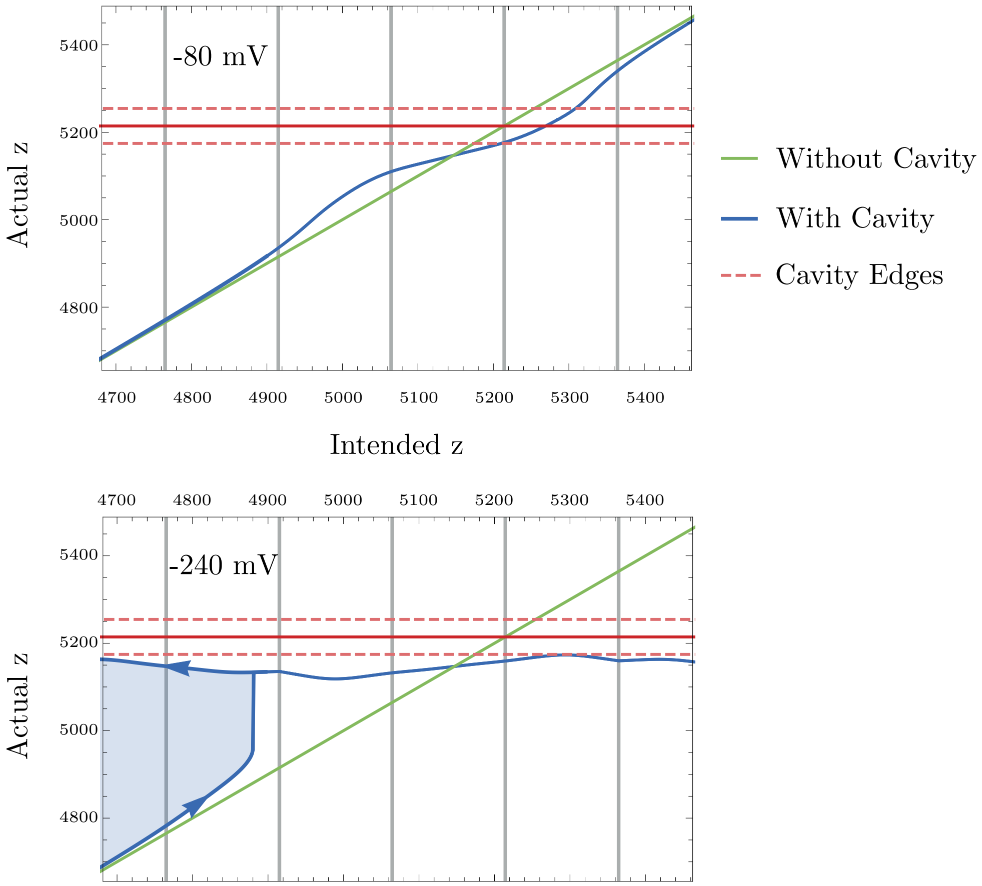

Figure 6.11: Simulated ion positions with vs. without a fiber cavity with negative patch charges, located at the fiber edge towards the loading zone, at the position along the trap axis $z = z_{cav} - 62.5\,\mu\text{m}$. In the case of hysteresis, the two different paths are denoted by arrows, and the avoided area is denoted by the pale blue background. The green line represents the intended path, $y = x$. The red, dashed lines enclose the cavity interaction zone. The black grid line is the position of the cavity on the x-axis, while the gray grid lines mark off shifts of one segment width. The upper figure shows a small patch charge that creates a potential of $V_d = -80\,\text{mV}$ in the trap center. In the lower figure, the potential has been increased to $V_d = -240\,\text{mV}$, and the ion is trapped by the patch charge and neither enters the interaction zone, nor leaves the cavity region again.

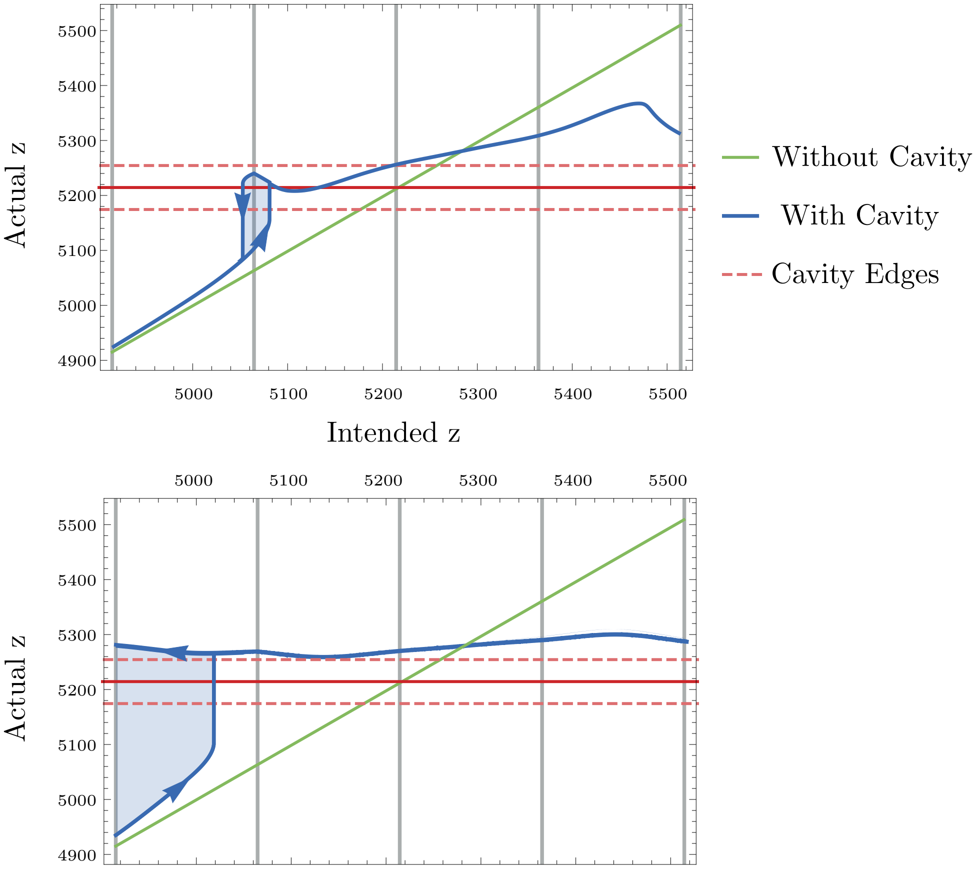

Figure 6.12: Simulated ion positions with vs without a fiber cavity with negative patch charges, located at the fiber edge away from the loading zone, at the position along the trap axis $z = z_{cav} + 62.5\,\mu\mathrm{m}$. The blue lines describe the ion's actual position in dependence to the intended one, while the green line represents the intended path, $y = x$. The red lines enclose the cavity interaction zone. The black grid line is the position of the cavity on the x-axis, while the gray grid lines mark off shifts of one segment width. Figure a) shows a small patch charge that creates a potential of $V_d = -110\,\mathrm{mV}$ in the trap center. In figure b), the potential has been increased to $V_d = -240\,\mathrm{mV}$, and the ion never enters the interaction zone.

disturbance potential of $V_d = -110\,\mathrm{mV}$, the weakest potential that creates a jump in ion position. As can be seen, the ion is pulled towards the cavity about a segment too early, but travels through the interaction region on its way to the point of attraction. In figure b), the weakest potential able to keep the ion completely outside the interaction zone, $V_d = -240\,\mathrm{mV}$, is shown. Here, the jump grows so large that the cavity is simply passed over and never entered.

In both attractive patch charge cases, the ion only keeps out of the interaction zone for the entirety of the transport when the potential has become quite strong, and clearly manages to trap the ion at its potential minimum once it has been brought (comparatively) close. This suggests an explanation for the shifting offset required for successful return of transported ions (described in section 6.2): The fibers are negatively charged, presumably with comparatively equal strength, and the offset is required to reduce the relative voltage created by patch charges towards the trap GND, in order to keep the attractive disturbance low enough so that the ion is not trapped in the disturbing field, or even entirely removed from the trap by instabilities. Comparing the large range of required offset voltages with the small range of stable transports into the cavity calculated in this section underlines that the achievement of cavity interaction in the presence of patch charges is a challenging problem. It may be mitigated by finding transport parameters with stronger DC voltages, thus reducing the relative shift due to patch charges. The trap behavior under tight confinement is promising for attempting this mitigation, as stable trapping up to $-7\,\mathrm{V}$ was achieved.

To summarize, I find that even a small electric charge on the fiber ends, larger than $+80\,\mathrm{mV}$ or less than $-240\,\mathrm{mV}$, blocks the ion from entering the cavity region. These patch charges can be caused by spurious light and photoelectron emission, and it is a highly probable the reason for an absence of optical pumping in Figure 6.7. It follows that integrating a fiber cavity into a Paul trap requires even more careful shielding of the surfaces of the fiber cavity. Examples of possible shielding technologies can be found, e.g., in Takahashi et al. [Tak18], where the fibers are inserted into hollow tubing making up one of the electrodes. Another possibility currently discussed is similar to our setup but with more extensive shielding: In the group of J. Home at ETH Zürich, fiber cavities are shielded from laser light by the trap structure, which has small holes to permit the cavity mode to pass through [2]. This shielding typically results is a slightly larger cavity length, which has to be compensated by higher

---

[2] Cavity Quantum Electrodynamics experiment of Jonathan Home, `https://tiqi.ethz.ch/research/cavity-quantum-electrodynamics.html`, Otto-Stern-Weg 1, HPF E10, 8093 Zürich, Switzerland

reflectivity and a larger radius of curvature of the fiber ends. Since this would reduce the mode matching between the fiber mode and the cavity mode (see section 2.4), it would be beneficial to switch to photonic crystal fibers, which allow customizing the radius of the fiber mode to better fit the cavity mode. That this can be successfully done today is shown in Ott et al. [Ott16], where new CO_2 fiber tip machining techniques have been used on photonic crystal fibers to overcome previous limits regarding maximum resonator length. Another option for improved mode matching is the splicing together of custom fiber ends from different single mode and multi mode fibers, as demonstrated in Gulati et al. [Gul17].

7 Conclusions

The final discussion of this thesis is divided into two parts. The first is concerned with the steps required to get the fiber trap to a fully functioning status. The second is concerned with the protocols analyzed and what changes of the setup are required to make them feasible.

At the beginning of this thesis, no functional integration of Paul trap and microcavity had been achieved. One important road block was the lack of high-quality fiber shaping techniques for building resonators with a length of more than 100 µm. This lack was addressed by us with the creation of our FIB-machined fibers, which allowed us to reach a finesse of 16000 while using an intra-mirror distance of 250 µm, more than double the previously achieved value. Our fibers are a good basis to work on, and allow useful tests of functionality, even though the analysis of the entanglement distribution protocols shows that we need even further improvements in fiber technology in the future. The difficulty of constructing a microfabricated Paul trap with small enough dimensions for a microresonator were also addressed in this thesis. With Fibertrap V3, we have developed a Paul trap capable of admitting a resonator of 250 µm length, which nonetheless can withstand the amount of current required for good trap operation, despite the high capacitative coupling putting strain on the VIAs. The direct figure of merit for this is the drop in resistance for the entire length of the electrodes, from $\overline{R} = 20(10)\,\Omega$ in Fibertrap V2 before repairing the trap by electroplating, down to $\overline{R} = 1.1(4)\,\Omega$ in Fibertrap V3 after electroplating, which was part of the design process for this trap version. The VIAs and the high number of electrodes that come with them also promise to be useful to combat any possible patch charges, as described in subsection 6.3.2.

For a long-term outlook, the most promising change to combat the effect of patch charges is the development of fiber shaping methods that allow very high finesses even at large distances of a few millimeters. Such techniques have been pioneered by Takahashi et al. [Tak14] and Ott et al. [Ott16]. Using these techniques, a fiber cavity with an intermediate length of about $300 - 400$ µm could be realized, offering a trade off between small mode volume and lower influence of patch charges, as well as even better shielding from stray, patch charge creating light. Failing that, the fibers would need to be encased in conducting shielding. This is a difficult proposition, however, due to two reasons: The fibers are in a very constrained space, and a conducting layer increases the danger of shorting the fiber with an electrode. Furthermore, a bad conductor in close proximity to the high RF fields of the Paul trap would heat up, and create a bright source of thermal light, destroying any possibility of coherent operations, and perhaps even of keeping the ion trapped, due to extreme heating rates. Ensuring that the conducting layer has a low enough resistance to avoid this problem may come into conflict with the space requirements.

It has also become clear, in the course of this thesis, that our monolithic fiber cavity holder, without capability of correcting deviations in the plane orthogonal to the cavity's axis, will not suffice in the current state for entanglement distribution. While its simplicity and stability is beneficial for prototype testing, and the proofs of principle that were attempted in this thesis, a high quality cavity requires the potential for minute corrections of the alignment even in vacuum. In order to avoid the difficulties a large, non-monolithic setup generates, especially the abundance of disruptive oscillation modes, it seems more promising to adapt the current construction using stiff arms slightly movable by piezo crystals.

In this thesis, we also discussed the implementations of three quantum repeater protocols, namely the distributed EPR protocol, the DLCZ protocol and the hybrid protocol, and various protocol extensions, within an ion trap setup. When comparing the protocols, we found that the DLCZ and the hybrid protocol outperform the EPR protocol. The most important limitations are of technical nature. We discovered that by improving the mode matching from the experimentally determined value of 0.44 to 0.54, which can be achieved through an improved cavity alignment, entanglement generation rates of $30\,\mathrm{s}^{-1}$ at fidelities of 0.9 with the DLCZ protocol are within reach. Furthermore, the impedance matching of the fiber optical cavity may be improved by coating the mirror of the I/O fiber with a material with different transmission coefficient as compared to the high reflection end mirror on the multimode fiber, which would allow a rate of up to $60\,\mathrm{s}^{-1}$.

The hybrid protocol appears interesting for future investigations, even though we would need to change the fiber cavity: The quick entanglement generation rate at medium-high fidelity makes it an ideal candidate to be used in combination with entanglement distillation schemes [Ben96; Dua00; Pan01]. That requires a rate of entanglement generation exceeding the decay rate of the stationary quantum memory. The qubit's coherence time is, in our case, limited by magnetic field fluctuations to 10 ms, which means that for an optimized hybrid rate of up to $750\,\mathrm{s}^{-1}$ at $F = 0.95$, already more entanglement per time would be created than lost. Encoding the stationary qubit in a decoherence-free substate [Häf05], and executing the mapping between qubus and logical qubit comprised of a two-ion Bell state [Cas15] with a coherence time on the order of 10 s, would improve the ratio of entanglement distribution time to coherence time to ≈ 7500.

Yet another option is the use of error correction codes in entanglement distribution. The basic code in Calderbank et al. [Cal96] and Schindler et al. [Sch11] requires two ancilla qubits per qubit, a low enough number to be realistically achieved in our setup, without the need to build multiple traps per QR node.

For a QR node, our platform will be combined with a single photon wavelength converter to provide compatibility with telecom fibers, in order to evolve our system from a lab based proof-of-principle experiment to a prototype, which may increase the maximally achievable distance for quantum communication.

Bibliography

[Aha16] I. Aharonovich, D. Englund, and M. Toth. “Solid-state single-photon emitters”. In: *Nature Photonics* 10.10 (Oct. 2016), pp. 631–641. DOI: `10.1038/nphoton.2016.186` (cit. on p. 11).

[Azu15] K. Azuma, K. Tamaki, and H.-K. Lo. “All-photonic quantum repeaters”. In: *Nature Communications* 6.1 (Apr. 2015). DOI: `10.1038/ncomms7787` (cit. on p. 13).

[Bal16] C. Ballance, T. Harty, N. Linke, M. Sepiol, and D. Lucas. “High-Fidelity Quantum Logic Gates Using Trapped-Ion Hyperfine Qubits”. In: *Physical Review Letters* 117.6 (Aug. 2016). DOI: `10.1103/physrevlett.117.060504` (cit. on p. 49).

[Bar09] H. G. Barros, A Stute, T. E. Northup, C Russo, P. O. Schmidt, and R Blatt. “Deterministic single-photon source from a single ion”. In: *New J. Phys.* 11.10 (2009), p. 103004 (cit. on p. 73).

[Ben84] C. H. Bennett and G. Brassard. “Quantum cryptography”. In: *Proceedings of IEEE International Conference on Computers, Systems and Signal Processing* 175 (1984), p. 8. DOI: `10.1016/Fj.tcs.2014.05.025` (cit. on p. 10).

[Ben92a] C. H. Bennett. “Quantum cryptography using any two nonorthogonal states”. In: *Physical Review Letters* 68.21 (1992), pp. 3121–3124. DOI: `10.1103/physrevlett.68.3121` (cit. on p. 10).

[Ben92b] C. H. Bennett, G. Brassard, and N. D. Mermin. “Quantum cryptography without Bell’s theorem”. In: *Physical Review Letters* 68.5 (1992), pp. 557–559. DOI: `10.1103/physrevlett.68.557` (cit. on p. 10).

[Ben93] C. H. Bennett, G. Brassard, C. Crépeau, R. Jozsa, A. Peres, and W. K. Wootters. “Teleporting an unknown quantum state via dual classical and Einstein-Podolsky-Rosen channels”. In: *Phys. Rev. Lett.* 70.13 (Mar. 1993), pp. 1895–1899. DOI: `10.1103/physrevlett.70.1895` (cit. on pp. 52, 62).

[Ben96] C. H. Bennett, G. Brassard, S. Popescu, B. Schumacher, J. A. Smolin, and W. K. Wootters. “Purification of Noisy Entanglement and Faithful Teleportation via Noisy Channels”. In: *Phys. Rev. Lett.* 76 (5 Jan. 1996), pp. 722–725. DOI: `10.1103/PhysRevLett.76.722` (cit. on pp. 11, 14, 136).

[Ber12] H. Bernien, L. Childress, L. Robledo, M. Markham, D. Twitchen, and R. Hanson. “Two-Photon Quantum Interference from Separate Nitrogen Vacancy Centers in Diamond”. In: *Physical Review Letters* 108.4 (Jan. 2012). DOI: `10.1103/physrevlett.108.043604` (cit. on p. 13).

[Bla10] R. B. Blakestad. “Transport of Trapped-Ion Qubits within a Scalable Quantum Processor”. PhD thesis. University of Colorado, 2010 (cit. on pp. 89, 97).

[Bow12] R. Bowler, J. Gaebler, Y. Lin, T. R. Tan, D. Hanneke, J. D. Jost, J. P. Home, D. Leibfried, and D. J. Wineland. “Coherent Diabatic Ion Transport and Separation in a Multizone Trap Array”. In: *Phys. Rev. Lett.* 109 (8 Aug. 2012), p. 080502. DOI: `10.1103/PhysRevLett.109.080502` (cit. on p. 85).

[Bra13] B. Brandstätter, A. McClung, K. Schüppert, B. Casabone, K. Friebe, A. Stute, P. O. Schmidt, C. Deutsch, J. Reichel, R. Blatt, and T. E. Northup. “Integrated fiber-mirror ion trap for strong ion-cavity coupling”. In: *Rev. Sci. Instrum.* 84, 123104 (2013), p. 123104. DOI: `10.1063/1.4838696` (cit. on pp. 35, 94).

[Bri98] H.-J. Briegel, W. Dür, J. I. Cirac, and P. Zoller. “Quantum Repeaters: The Role of Imperfect Local Operations in Quantum Communication”. In: *Phys. Rev. Lett.* 81 (26 Dec. 1998), pp. 5932–5935. DOI: `10.1103/PhysRevLett.81.5932` (cit. on pp. 11, 14).

[Bro14] M. Brownnutt, M. Kumph, P. Rabl, and R. Blatt. “Ion-trap measurements of electric-field noise near surface”. In: *ArXiv e-prints* arXiv:1409.6572 (Sept. 2014). DOI: `arXiv:1409.6572` (cit. on p. 35).

[Bud08] D. Budker, D. F. Kimball, and D. P. DeMille. *Atomic Physics: an exploration through problems and solutions.* Oxford Univ. Press, 2008 (cit. on p. 38).

[Cab99] C. Cabrillo, J. I. Cirac, P. Garcia-Fernandez, and P. Zoller. “Creation of entangled states of distant atoms by interference”. In: *Phys. Rev. A* 59 (2 Feb. 1999), pp. 1025–1033. DOI: `10.1103/PhysRevA.59.1025` (cit. on pp. 55, 59, 79).

[Cal96] A. R. Calderbank and P. W. Shor. “Good quantum error-correcting codes exist”. In: *Phys. Rev. A* 54.2 (Aug. 1996), pp. 1098–1105. DOI: `10.1103/physreva.54.1098` (cit. on pp. 14, 137).

[Cas15] B. Casabone, K. Friebe, B. Brandstätter, K. Schüppert, R. Blatt, and T. Northup. “Enhanced Quantum Interface with Collective Ion-Cavity Coupling”. In: *Phys. Rev. Lett.* 114 (2 2015), p. 023602. DOI: `10.1103/PhysRevLett.114.023602` (cit. on pp. 15, 137).

[Cir95] J. I. Cirac and P. Zoller. “Quantum Computations with Cold Trapped Ions”. In: *Phys. Rev. Lett.* 74 (20 May 1995), pp. 4091–4094. DOI: `10.1103/PhysRevLett.74.4091` (cit. on p. 15).

[Col07] Y. Colombe, T. Steinmetz, G. Dubois, F. Linke, D. Hunger, and J. Reichel. “Strong atom-field coupling for Bose-Einstein condensates in an optical cavity on a chip”. In: *Nature* 450.7167 (Nov. 2007), pp. 272–276. DOI: `10.1038/nature06331` (cit. on p. 35).

[Deu96] D. Deutsch, A. Ekert, R. Jozsa, C. Macchiavello, S. Popescu, and A. Sanpera. “Quantum Privacy Amplification and the Security of Quantum Cryptography over Noisy Channels”. In: *Phys. Rev. Lett.* 77 (13 Sept. 1996), pp. 2818–2821. DOI: `10.1103/PhysRevLett.77.2818` (cit. on pp. 11, 14).

[Dua00] L.-M. Duan, G. Giedke, J. I. Cirac, and P. Zoller. “Entanglement Purification of Gaussian Continuous Variable Quantum States”. In: *Phys. Rev. Lett.* 84 (17 Apr. 2000), pp. 4002–4005. DOI: `10.1103/PhysRevLett.84.4002` (cit. on p. 136).

[Dua01] L.-M. Duan, M. D. Lukin, J. I. Cirac, and P. Zoller. “Long-distance quantum communication and with atomic ensembles and linear optics”. In: *Nature* 414 (Nov. 2001), pp. 413–418. DOI: `10.1038/35106500` (cit. on p. 55).

[Dua10] L.-M. Duan and C. Monroe. “Colloquium: Quantum networks with trapped ions”. In: *Rev. Mod. Phys.* 82.2 (Apr. 2010), pp. 1209–1224. DOI: `10.1103/revmodphys.82.1209` (cit. on p. 11).

[Dür03] W. Dür and H.-J. Briegel. “Entanglement Purification for Quantum Computation”. In: *Physical Review Letters* 90.6 (Feb. 2003). DOI: `10.1103/physrevlett.90.067901` (cit. on p. 11).

[Dür07] W. Dür and H. J. Briegel. “Entanglement purification and quantum error correction”. In: *Rep. Prog. Phys.* 70.8 (July 2007), pp. 1381–1424. DOI: `10.1088/0034-4885/70/8/r03` (cit. on p. 11).

[Dür99] W. Dür, H.-J. Briegel, J. I. Cirac, and P. Zoller. “Quantum repeaters based on entanglement purification”. In: *Physical Review A* 59.1 (Jan. 1999), pp. 169–181. DOI: `10.1103/physreva.59.169` (cit. on p. 14).

[Dus00] M. Dusek, M. Jahma, and N. Lütkenhaus. “Unambiguous state discrimination in quantum cryptography with weak coherent states”. In: *Phys. Rev. A* 62 (2 July 2000), p. 022306. DOI: `10.1103/PhysRevA.62.022306` (cit. on p. 62).

[Ear42] S. Earnshaw. “On the nature of the molecular forces which regulate the constitution of the luminferous ether”. In: *Trans. Camb. Phil. Soc.* 7 (1842), pp. 97–112 (cit. on p. 18).

[Ein35] A. Einstein, B. Podolsky, and N. Rosen. “Can Quantum-Mechanical Description of Physical Reality Be Considered Complete?” In: *Physical Review* 47.10 (May 1935), pp. 777–780. DOI: `10.1103/physrev.47.777` (cit. on p. 9).

[Eke91] A. K. Ekert. “Quantum cryptography based on Bell’s theorem”. In: *Phys. Rev. Lett.* 67 (6 Aug. 1991), pp. 661–663. DOI: `10.1103/PhysRevLett.67.661` (cit. on pp. 10, 12).

[Fis59] E. Fischer. “Die dreidimensionale Stabilisierung von Ladungsträgern in einem Vierpolfeld”. In: *Zeitschrift für Physik* 156.1 (Mar. 1959), pp. 1–26. DOI: `10.1007/bf01332512` (cit. on p. 18).

[Fow10] A. G. Fowler, D. S. Wang, C. D. Hill, T. D. Ladd, R. V. Meter, and L. C. L. Hollenberg. “Surface Code Quantum Communication”. In: *Physical Review Letters* 104.18 (2010). DOI: `10.1103/physrevlett.104.180503` (cit. on p. 14).

[Gae16] J. Gaebler, T. Tan, Y. Lin, Y. Wan, R. Bowler, A. Keith, S. Glancy, K. Coakley, E. Knill, D. Leibfried, and D. Wineland. “High-Fidelity Universal Gate Set for Be9+ Ion Qubits”. In: *Physical Review Letters* 117.6 (2016). DOI: `10.1103/physrevlett.117.060505` (cit. on p. 49).

[Gal16] J. Gallego, S. Ghosh, S. K. Alavi, W. Alt, M. Martinez-Dorantes, D. Meschede, and L. Ratschbacher. “High-finesse fiber Fabry–Perot cavities: stabilization and mode matching analysis”. In: *Applied Physics B* 122.3 (2016). DOI: `10.1007/s00340-015-6281-z` (cit. on p. 84).

[Gio06] V. Giovannetti, S. Lloyd, and L. Maccone. “Quantum Metrology”. In: *Physical Review Letters* 96.1 (Jan. 2006). DOI: `10.1103/physrevlett.96.010401` (cit. on p. 9).

[Gla63] R. J. Glauber. “Coherent and Incoherent States of the Radiation Field”. In: *Physical Review* 131.6 (Sept. 1963), pp. 2766–2788. DOI: `10.1103/physrev.131.2766` (cit. on p. 53).

[Gsc15] M. Gschrey, A. Thoma, P. Schnauber, M. Seifried, R. Schmidt, B. Wohlfeil, L. Kruger, J.-H. Schulze, T. Heindel, S. Burger, F. Schmidt, A. Strittmatter, S. Rodt, and S. Reitzenstein. “Highly indistinguishable photons from deterministic quantum-dot microlenses utilizing three-dimensional in situ electron-beam lithography”. In: *Nat. Commun.* 6 (July 2015). DOI: `10.1038/ncomms8662` (cit. on p. 11).

[Gul03] S. Gulde, H. Haffner, M. Riebe, G. Lancaster, C. Becher, J. Eschner, F. Schmidt-Kaler, I. L. Chuang, and R. Blatt. “Quantum information processing with trapped Ca+ ions”. In: *Philosophical Transactions of the Royal Society A: Mathematical, Physical and Engineering Sciences* 361.1808 (July 2003), pp. 1363–1374. DOI: `10.1098/rsta.2003.1206` (cit. on p. 50).

[Gul17] G. K. Gulati, H. Takahashi, N. Podoliak, P. Horak, and M. Keller. “Fiber cavities with integrated mode matching optics”. In: *Scientific Reports* 7.1 (2017). DOI: `10.1038/s41598-017-05729-8` (cit. on p. 134).

[Had09] R. H. Hadfield. “Single-photon detectors for optical quantum information applications”. In: *Nature Photonics* 3.12 (Dec. 2009), pp. 696–705. DOI: `10.1038/nphoton.2009.230` (cit. on p. 75).

[Häf05] H. Häffner, F. Schmidt-Kaler, W. Hänsel, C. Roos, T. Körber, M. Chwalla, M. Riebe, J. Benhelm, U. Rapol, C. Becher, and R. Blatt. “Robust entanglement”. English. In: *Appl. Phys. B* 81.2-3 (2005), pp. 151–153. DOI: `10.1007/s00340-005-1917-z` (cit. on p. 137).

[Har06] S. Haroche and J. M. Raimond. *Exploring the quantum.* Oxford Univ. Press, 2006 (cit. on p. 38).

[Har10] M. Harlander, M. Brownnutt, W. Hänsel, and R. Blatt. “Trapped-ion probing of light-induced charging effects on dielectrics”. In: *New J. Phys.* 12.9 (2010), p. 093035 (cit. on pp. 35, 86, 126).

[Har92] S Haroche. *Fundamental Systems in Quantum Optics (Les Houches Session LIII), editors J. Dalibard, J.M. Raimond and J. Zinn-Justin.* 1992 (cit. on p. 44).

[Hei11] D. Heinrich. “Betrieb einer kryogenen Mikroionenfalle mit Licht-Ion-Schnittstelle für einen zukünftigen Quantenrepeater”. MA thesis. Universität Mainz, 2011 (cit. on p. 94).

[Her09] P. F. Herskind, A. Dantan, M. Albert, J. P. Marler, and M. Drewsen. “Positioning of the rf potential minimum line of a linear Paul trap with micrometer precision”. In: *J. Phys. B: At., Mol. Opt. Phys.* 42.15 (July 2009), p. 154008. DOI: `10.1088/0953-4075/42/15/154008` (cit. on p. 87).

[Her11] P. F. Herskind, S. X. Wang, M. Shi, Y. Ge, M. Cetina, and I. L. Chuang. “Microfabricated surface ion trap on a high-finesse optical mirror”. In: *Opt. Lett.* 36.16 (2011), p. 3045. DOI: `10.1364/ol.36.003045` (cit. on p. 35).

[Het16] M. Hettrich. “Measurement of Reduced Dipole Matrix Elements in $^{40}Ca^{+}$ and Construction of a Scalable Light-Ion Interface”. PhD thesis. Universität Ulm, 2016 (cit. on pp. 95, 96).

[Hom09] J. P. Home, D. Hanneke, J. D. Jost, J. M. Amini, D. Leibfried, and D. J. Wineland. “Complete Methods Set for Scalable Ion Trap Quantum Information Processing”. In: *Science* 325.5945 (2009), pp. 1227–1230. DOI: `10.1126/science.1177077` (cit. on p. 15).

[Hoo01] C. J. Hood, H. J. Kimble, and J. Ye. “Characterization of high-finesse mirrors: Loss, phase shifts, and mode structure in an optical cavity”. In: *Phys. Rev. A* 64 (3 Aug. 2001), p. 033804. DOI: `10.1103/PhysRevA.64.033804` (cit. on p. 84).

[Hub08] G Huber, T Deuschle, W Schnitzler, R Reichle, K Singer, and F Schmidt-Kaler. “Transport of ions in a segmented linear Paul trap in printed-circuit-board technology”. In: *New Journal of Physics* 10.1 (Jan. 2008), p. 013004. DOI: `10.1088/1367-2630/10/1/013004` (cit. on p. 122).

[Huc14] D. Hucul, I. V. Inlek, G. Vittorini, C. Crocker, S. Debnath, S. M. Clark, and C. Monroe. “Modular entanglement of atomic qubits using photons and phonons”. In: *Nature Physics* 11.1 (2014), pp. 37–42. DOI: `10.1038/nphys3150` (cit. on pp. 9, 11, 82).

[Huw13] J. Huwer, J. Ghosh, N. Piro, M. Schug, F. Dubin, and J. Eschner. “Photon entanglement detection by a single atom”. In: *New J. Phys.* 15.2 (2013), p. 025033 (cit. on p. 67).

[Iku11] R. Ikuta, Y. Kusaka, T. Kitano, H. Kato, T. Yamamoto, M. Koashi, and N. Imoto. "Wide-band quantum interface for visible-to-telecommunicatio wavelength conversion". In: *Nat Comms* 2 (Nov. 2011), p. 1544. DOI: `10.1038/ncomms1544` (cit. on p. 15).

[Jia08] H. Jiang, F. Kéfélian, S. Crane, O. Lopez, M. Lours, J. Millo, D. Holleville, P. Lemonde, C. Chardonnet, A. Amy-Klein, and G. Santarelli. "Long-distance frequency transfer over an urban fiber link using optical phase stabilization". In: *Journal of the Optical Society of America B* 25.12 (2008), p. 2029. DOI: `10.1364/josab.25.002029` (cit. on pp. 72, 81).

[Jia09] L. Jiang, J. M. Taylor, K. Nemoto, W. J. Munro, R. Van Meter, and M. D. Lukin. "Quantum repeater with encoding". In: *Phys. Rev. A* 79 (3 Mar. 2009), p. 032325. DOI: `10.1103/PhysRevA.79.032325` (cit. on p. 14).

[Jin93] J. Jin and D. A. Church. "Precision lifetimes for the Ca+$4p^2P$levels: Experiment challenges theory at the 1% level". In: *Physical Review Letters* 70.21 (May 1993), pp. 3213–3216. DOI: `10.1103/physrevlett.70.3213` (cit. on pp. 122, 125).

[Kal17] N. Kalb, A. A. Reiserer, P. C. Humphreys, J. J. W. Bakermans, S. J. Kamerling, N. H. Nickerson, S. C. Benjamin, D. J. Twitchen, M. Markham, and R. Hanson. "Entanglement distillation between solid-state quantum network nodes". In: *Science* 356.6341 (June 2017), pp. 928–932. DOI: `10.1126/science.aan0070` (cit. on p. 14).

[Kau14] H. Kaufmann, T. Ruster, C. T. Schmiegelow, F. Schmidt-Kaler, and U. G. Poschinger. "Dynamics and control of fast ion crystal splitting in segmented Paul traps". In: *New J. Phys.* 16.7 (2014), p. 073012 (cit. on p. 85).

[Kau17a] H. Kaufmann, T. Ruster, C. T. Schmiegelow, M. A. Luda, V. Kaushal, J. Schulz, D. von Lindenfels, F. Schmidt-Kaler, and U. G. Poschinger. "Fast ion swapping for quantum-information processing". In: *Physical Review A* 95.5 (May 2017). DOI: `10.1103/physreva.95.052319` (cit. on pp. 15, 50, 51, 85).

[Kau17b] H. Kaufmann. "A Scalable Quantum Processor". PhD thesis. Johannes Gutenberg Universität Mainz, 2017 (cit. on pp. 49, 87, 89, 92, 97, 98, 107).

[Kau18] P. Kaufmann, T. F. Gloger, D. Kaufmann, M. Johanning, and C. Wunderlich. “High-Fidelity Preservation of Quantum Information During Trapped-Ion Transport”. In: *Physical Review Letters* 120.1 (2018). DOI: `10.1103/physrevlett.120.010501` (cit. on p. 119).

[Kie02] D. Kielpinski, C. Monroe, and D. J. Wineland. “Architecture for a large-scale ion-trap quantum computer”. In: *Nature* 417.6890 (2002), p. 709. DOI: `10.1038/nature00784` (cit. on pp. 15, 16).

[Kur14] C. Kurz, M. Schug, P. Eich, J. Huwer, P. Müller, and J. Eschner. “Experimental protocol for high-fidelity heralded photon-to-atom quantum state transfer”. In: *Nat. Commun.* 5 (Nov. 2014), p. 5527. DOI: `10.1038/ncomms6527` (cit. on pp. 56, 79).

[Kur15] C. Kurz. “Quantum networking with single ions and single photons interfaced in free space”. PhD thesis. Saarbrücken: Universität des Saarlandes, 2015 (cit. on p. 69).

[Kuz03] A. Kuzmich, W. P. Bowen, A. D. Boozer, A. Boca, C. W. Chou, L.-M. Duan, and H. J. Kimble. “Generation of nonclassical photon pairs for scalable quantum communication with atomic ensembles”. In: *Nature* 423.6941 (2003), pp. 731–734. DOI: `10.1038/nature01714` (cit. on p. 11).

[Lad06] T. D. Ladd, P van Loock, K Nemoto, W. J. Munro, and Y Yamamoto. “Hybrid quantum repeater based on dispersive CQED interactions between matter qubits and bright coherent light”. In: *New J. Phys.* 8.9 (2006), p. 184 (cit. on pp. 60, 62, 77).

[Lei03a] D. Leibfried, R. Blatt, C. Monroe, and D. Wineland. “Quantum dynamics of single trapped ions”. In: *Rev. Mod. Phys.* 75 (1 Mar. 2003), pp. 281–324. DOI: `10.1103/RevModPhys.75.281` (cit. on pp. 21, 42).

[Lei03b] D. Leibfried, B. DeMarco, V. Meyer, D. Lucas, M. Barrett, J. Britton, W. M. Itano, B. Jelenkovic, C. Langer, T. Rosenband, and D. J. Wineland. “Experimental demonstration of a robust, high-fidelity geometric two ion-qubit phase gate”. In: *Nature* 422.6930 (Mar. 2003), pp. 412–415. DOI: `10.1038/nature01492` (cit. on pp. 20, 47).

[Lia18] S.-K. Liao et al. “Satellite-Relayed Intercontinental Quantum Network”. In: *Physical Review Letters* 120.3 (Jan. 2018). DOI: `10.1103/physrevlett.120.030501` (cit. on p. 11).

[Llo01] S. Lloyd, M. S. Shahriar, J. H. Shapiro, and P. R. Hemmer. "Long Distance, Unconditional Teleportation of Atomic States via Complete Bell State Measurements". In: *Phys. Rev. Lett.* 87 (16 Sept. 2001), p. 167903. DOI: `10.1103/PhysRevLett.87.167903` (cit. on pp. 55, 56).

[Loo06] P. van Loock, T. D. Ladd, K. Sanaka, F. Yamaguchi, K. Nemoto, W. J. Munro, and Y. Yamamoto. "Hybrid Quantum Repeater Using Bright Coherent Light". In: *Phys. Rev. Lett.* 96 (24 June 2006), p. 240501. DOI: `10.1103/PhysRevLett.96.240501` (cit. on pp. 55, 58, 60, 61).

[Loo08] P. van Loock, N. Lütkenhaus, W. J. Munro, and K. Nemoto. "Quantum repeaters using coherent-state communication". In: *Phys. Rev. A* 78 (6 Dec. 2008), p. 062319. DOI: `10.1103/PhysRevA.78.062319` (cit. on pp. 60–62).

[Ma12] X.-S. Ma, T. Herbst, T. Scheidl, D. Wang, S. Kropatschek, W. Naylor, B. Wittmann, A. Mech, J. Kofler, E. Anisimova, V. Makarov, T. Jennewein, R. Ursin, and A. Zeilinger. "Quantum teleportation over 143 kilometres using active feed-forward". In: *Nature* 489.7415 (Sept. 2012), pp. 269–273. DOI: `10.1038/nature11472` (cit. on p. 11).

[Ma94] L.-S. Ma, P. Jungner, J. Ye, and J. L. Hall. "Delivering the same optical frequency at two places: accurate cancellation of phase noise introduced by an optical fiber or other time-varying path". In: *Opt. Lett.* 19.21 (1994), p. 1777. DOI: `10.1364/ol.19.001777` (cit. on p. 81).

[Mac59] W. Macalpine and R. Schildknecht. "Coaxial Resonators with Helical Inner Conductor". In: *Proceedings of the IRE* 47.12 (Dec. 1959), pp. 2099–2105. DOI: `10.1109/jrproc.1959.287128` (cit. on p. 36).

[Mes05] D. Meschede. *Optik, Licht und Laser.* Lehrbuch Physik. Teubner, 2005 (cit. on pp. 77, 84).

[Min08] J. Minář, H. de Riedmatten, C. Simon, H. Zbinden, and N. Gisin. "Phase-noise measurements in long-fiber interferometers for quantum-repeater applications". In: *Physical Review A* 77.5 (May 2008), p. 052325. DOI: `10.1103/physreva.77.052325` (cit. on pp. 72, 81).

[Moe07] D. L. Moehring, P. Maunz, S. Olmschenk, K. C. Younge, D. N. Matsukevich, L.-M. Duan, and C. Monroe. “Entanglement of single-atom quantum bits at a distance”. In: *Nature* 449.7158 (Sept. 2007), pp. 68–71. DOI: `10.1038/nature06118` (cit. on p. 14).

[Mon11] T. Monz, P. Schindler, J. T. Barreiro, M. Chwalla, D. Nigg, W. A. Coish, M. Harlander, W. Hänsel, M. Hennrich, and R. Blatt. “14-qubit entanglement: Creation and coherence”. In: *Physical Review Letters* 106.13 (2011), p. 130506. DOI: `10.1103/physrevlett.106.130506` (cit. on p. 15).

[Mon14] C. Monroe, R. Raussendorf, A. Ruthven, K. R. Brown, P. Maunz, L.-M. Duan, and J. Kim. “Large-scale modular quantum-computer architecture with atomic memory and photonic interconnects”. In: *Phys. Rev. A* 89.2 (Feb. 2014). DOI: `10.1103/physreva.89.022317` (cit. on p. 9).

[Mon95] C. Monroe, D. M. Meekhof, B. E. King, S. R. Jefferts, W. M. Itano, D. J. Wineland, and P. Gould. “Resolved-Sideband Raman Cooling of a Bound Atom to the 3D Zero-Point Energy”. In: *Physical Review Letters* 75.22 (Nov. 1995), pp. 4011–4014. DOI: `10.1103/physrevlett.75.4011` (cit. on p. 32).

[Mun02] A. B. Mundt, A. Kreuter, C. Becher, D. Leibfried, J. Eschner, F. Schmidt-Kaler, and R. Blatt. “Coupling a Single Atomic Quantum Bit to a High Finesse Optical Cavity”. In: *Phys. Rev. Lett.* 89 (10 Aug. 2002), p. 103001. DOI: `10.1103/PhysRevLett.89.103001` (cit. on p. 15).

[Mun12] W. J. Munro, A. M. Stephens, S. J. Devitt, K. A. Harrison, and K. Nemoto. “Quantum communication without the necessity of quantum memories”. In: *Nat. Photonics* 6.11 (Oct. 2012), pp. 777–781. DOI: `10.1038/nphoton.2012.243` (cit. on p. 14).

[Mur16] S. Muralidharan, L. Li, J. Kim, N. Lütkenhaus, M. D. Lukin, and L. Jiang. “Optimal architectures for long distance quantum communication”. In: *Scientific Reports* 6.1 (Feb. 2016). DOI: `10.1038/srep20463` (cit. on p. 13).

[Mus08] M. Musha, F.-L. Hong, K. Nakagawa, and K.-i. Ueda. “Coherent optical frequency transfer over 50-km physical distance using a 120-km-long installed telecom fiber network”. In: *Opt. Express* 16.21 (2008), p. 16459. DOI: `10.1364/oe.16.016459` (cit. on p. 72).

[Nic14] N. H. Nickerson, J. F. Fitzsimons, and S. C. Benjamin. “Freely Scalable Quantum Technologies Using Cells of 5-to-50 Qubits with Very Lossy and Noisy Photonic Links”. In: *Physical Review X* 4.4 (Dec. 2014). DOI: `10.1103/physrevx.4.041041` (cit. on p. 11).

[Nie00] M. A. Nielsen and I. L. Chuang. *Quantum computation and information.* Cambridge university press Cambridge, 2000 (cit. on p. 9).

[Nig14] D. Nigg, M. Müller, E. A. Martinez, P. Schindler, M. Hennrich, T. Monz, M. A. Martin-Delgado, and R. Blatt. “Quantum computations on a topologically encoded qubit”. In: *Science* 345.6194 (2014), pp. 302–305. DOI: `10.1126/science.1253742` (cit. on pp. 14, 15).

[Ott16] K. Ott, S. Garcia, R. Kohlhaas, K. Schüppert, P. Rosenbusch, R. Long, and J. Reichel. “Millimeter-long fiber Fabry-Perot cavities”. In: *Optics Express* 24.9 (Apr. 2016), p. 9839. DOI: `10.1364/oe.24.009839` (cit. on pp. 134, 135).

[Pan01] J.-W. Pan, C. Simon, C. Brukner, and A. Zeilinger. “Entanglement purification for quantum communication”. In: *Nature* 410.6832 (Apr. 2001), pp. 1067–1070. DOI: `10.1038/35074041` (cit. on p. 136).

[Pau53] W. Paul and H. Steinwedel. “Notizen: Ein neues Massenspektrometer ohne Magnetfeld”. In: *Zeitschrift für Naturforschung A* 8.7 (Jan. 1953), pp. 448–450. DOI: `10.1515/zna-1953-0710` (cit. on p. 18).

[Pfi16] A. D. Pfister, M. Salz, M. Hettrich, U. G. Poschinger, and F. Schmidt-Kaler. “A quantum repeater node with trapped ions: a realistic case example”. In: *Applied Physics B* 122.4 (Apr. 2016). DOI: `10.1007/s00340-016-6362-7` (cit. on p. 55).

[Pos09] U. G. Poschinger, G. Huber, F. Ziesel, M. Deiss, M. Hettrich, S. A. Schulz, G. Poulsen, M. Drewsen, R. J. Hendricks, K. Singer, and F. Schmidt-Kaler. “Coherent Manipulation of a $^{40}\mathrm{Ca}^{+}$ Spin Qubit in a Micro Ion Trap”. In: *J. Phys. B* 42 (2009), p. 154013 (cit. on pp. 29, 82).

[Pos10] U. G. Poschinger. “Quantum Optics Experiments in a Microstructured Ion Trap”. PhD thesis. Universität Ulm, 2010 (cit. on pp. 21, 32).

[Pre08] D. Press, T. D. Ladd, B. Zhang, and Y. Yamamoto. “Complete quantum control of a single quantum dot spin using ultrafast optical pulses”. In: *Nature* 456.7219 (Nov. 2008), pp. 218–221. DOI: `10.1038/nature07530` (cit. on p. 11).

[Rau01] R. Raussendorf and H. J. Briegel. “A One-Way Quantum Computer”. In: *Physical Review Letters* 86.22 (May 2001), pp. 5188–5191. DOI: `10.1103/physrevlett.86.5188` (cit. on p. 13).

[Rei06a] R. Reichle, D. Leibfried, R. Blakestad, J. Britton, J. Jost, E. Knill, C. Langer, R. Ozeri, S. Seidelin, and D. Wineland. “Transport dynamics of single ions in segmented microstructured Paul trap arrays”. In: *Fortschritte der Physik* 54.8-10 (Aug. 2006), pp. 666–685. DOI: `10.1002/prop.200610326` (cit. on pp. 15, 28).

[Rei06b] R. Reichle, D. Leibfried, E. Knill, J. Britton, R. B. Blakestad, J. D. Jost, C. Langer, R. Ozeri, S. Seidelin, and D. J. Wineland. “Experimental purification of two-atom entanglement”. In: *Nature* 443.7113 (Oct. 2006), pp. 838–841. DOI: `10.1038/nature05146` (cit. on pp. 14, 15).

[Rie08] M. Riebe, T. Monz, K. Kim, A. S. Villar, P. Schindler, M. Chwalla, M. Hennrich, and R. Blatt. “Deterministic entanglement swapping with an ion-trap quantum computer”. In: *Nat. Phys.* 4 (Nov. 2008), pp. 839–842. DOI: `10.1038/nphys1107` (cit. on pp. 15, 52, 62).

[Rit12] S. Ritter, C. Nolleke, C. Hahn, A. Reiserer, A. Neuzner, M. Uphoff, M. Mucke, E. Figueroa, J. Bochmann, and G. Rempe. “An elementary quantum network of single atoms in optical cavities”. In: *Nature* 484.7393 (Apr. 2012), pp. 195–200. DOI: `10.1038/nature11023` (cit. on p. 11).

[Roo00] C. F. Roos. “Controlling the quantum state of trapped ions”. PhD thesis. Leopold-Franzens-Universität Innsbruck, 2000 (cit. on p. 32).

[Roo99] C. Roos, T. Zeiger, H Rohde, H. Nägerl, J Eschner, D Leibfried, F Schmidt-Kaler, and R Blatt. “Quantum state engineering on an optical transition and decoherence in a Paul trap”. In: *Physical Review Letters* 83.23 (1999), p. 4713. DOI: `10.1103/PhysRevLett.83.4713` (cit. on p. 29).

[Rot03] D. Rotter. “Photoionization von Kalzium”. MA thesis. Leopold-Franzens-Universität Innsbruck, 2003 (cit. on p. 29).

[Rus14] T. Ruster, C. Warschburger, H. Kaufmann, C. T. Schmiegelow, A. Walther, M. Hettrich, A. Pfister, V. Kaushal, F. Schmidt-Kaler, and U. G. Poschinger. “Experimental realization of fast ion separation in segmented Paul traps”. In: *Phys. Rev. A* 90 (2014), p. 033410. DOI: `10.1103/PhysRevA.90.033410` (cit. on pp. 36, 85).

[Sal13] M. Salz. "Optimierung einer segmentierten Paulfalle mit optischer Schnittstelle". MA thesis. Universität Mainz, 2013 (cit. on p. 83).

[San11] N. Sangouard, C. Simon, H. de Riedmatten, and N. Gisin. "Quantum repeaters based on atomic ensembles and linear optics". In: *Rev. Mod. Phys.* 83 (1 Mar. 2011), pp. 33–80. DOI: `10.1103/RevModPhys.83.33` (cit. on pp. 14, 81).

[Sch06] S. Schulz, U. Poschinger, K. Singer, and F. Schmidt-Kaler. "Optimization of segmented linear Paul traps and transport of stored particles". In: *Fortschr. Phys.* 54.8-10 (2006), pp. 648–665. DOI: `10.1002/prop.200610324` (cit. on p. 15).

[Sch08] S. A. Schulz, U. Poschinger, F. Ziesel, and F. Schmidt-Kaler. "Sideband cooling and coherent dynamics in a microchip multi-segmented ion trap". In: *New Journal of Physics* 10.4 (2008), p. 045007. DOI: `10.1088/1367-2630/10/4/045007` (cit. on pp. 85, 86).

[Sch09] S. Schulz. "Scalable Microchip Ion Traps for Quantum Computation". PhD thesis. Universität Ulm, 2009 (cit. on pp. 18, 85, 87, 94).

[Sch10] C. Schuck, F. Rohde, N. Piro, M. Almendros, J. Huwer, M. W. Mitchell, M. Hennrich, A. Haase, F. Dubin, and J. Eschner. "Resonant interaction of a single atom with single photons from a down-conversion source". In: *Phys. Rev. A* 81 (1 Jan. 2010), p. 011802. DOI: `10.1103/PhysRevA.81.011802` (cit. on p. 67).

[Sch11] P. Schindler, J. T. Barreiro, T. Monz, V. Nebendahl, D. Nigg, M. Chwalla, M. Hennrich, and R. Blatt. "Experimental Repetitive Quantum Error Correction". In: *Science* 332.6033 (May 2011), pp. 1059–1061. DOI: `10.1126/science.1203329` (cit. on p. 137).

[Sch13] P. Schindler, D. Nigg, T. Monz, J. T. Barreiro, E. Martinez, S. X. Wang, S. Quint, M. F. Brandl, V. Nebendahl, C. F. Roos, M. Chwalla, M. Hennrich, and R. Blatt. "A quantum information processor with trapped ions". In: *New J. Phys.* 15.12 (2013), p. 123012 (cit. on pp. 29, 55).

[Sch14] M. Schug, C. Kurz, P. Eich, J. Huwer, P. Müller, and J. Eschner. "Quantum interference in the absorption and emission of single photons by a single ion". In: *Phys. Rev. A* 90 (2 Aug. 2014), p. 023829. DOI: `10.1103/PhysRevA.90.023829` (cit. on pp. 56, 79).

[Sho95] P. W. Shor. "Scheme for reducing decoherence in quantum computer memory". In: *Phys. Rev. A* 52.4 (Oct. 1995), R2493–R2496. DOI: `10.1103/physreva.52.r2493` (cit. on p. 11).

[Sim03] C. Simon and W. T. M. Irvine. "Robust Long-Distance Entanglement and a Loophole-Free Bell Test with Ions and Photons". In: *Phys. Rev. Lett.* 91 (11 Sept. 2003), p. 110405. DOI: `10.1103/PhysRevLett.91.110405` (cit. on pp. 55, 73).

[Sin10] K. Singer, U. Poschinger, M. Murphy, P. Ivanov, F. Ziesel, T. Calarco, and F. Schmidt-Kaler. "Colloquium : Trapped ions as quantum bits: Essential numerical tools". In: *Reviews of Modern Physics* 82.3 (Sept. 2010), pp. 2609–2632. DOI: `10.1103/revmodphys.82.2609` (cit. on p. 23).

[Sip12] A. Sipahigil, M. L. Goldman, E. Togan, Y. Chu, M. Markham, D. J. Twitchen, A. S. Zibrov, A. Kubanek, and M. D. Lukin. "Quantum Interference of Single Photons from Remote Nitrogen-Vacancy Centers in Diamond". In: *Physical Review Letters* 108.14 (Apr. 2012). DOI: `10.1103/physrevlett.108.143601` (cit. on p. 13).

[Sip14] A. Sipahigil, K. Jahnke, L. Rogers, T. Teraji, J. Isoya, A. Zibrov, F. Jelezko, and M. Lukin. "Indistinguishable Photons from Separated Silicon-Vacancy Centers in Diamond". In: *Physical Review Letters* 113.11 (Sept. 2014). DOI: `10.1103/physrevlett.113.113602` (cit. on p. 13).

[Ste14] M. Steiner, H. M. Meyer, J. Reichel, and M. Köhl. "Photon Emission and Absorption of a Single Ion Coupled to an Optical-Fiber Cavity". In: *Phys. Rev. Lett.* 113.263003 (Dec. 2014). DOI: `10.1103/physrevlett.113.263003` (cit. on pp. 15, 35, 82).

[Ste96] A. M. Steane. "Error Correcting Codes in Quantum Theory". In: *Phys. Rev. Lett.* 77.5 (July 1996), pp. 793–797. DOI: `10.1103/physrevlett.77.793` (cit. on p. 11).

[Stu12] A. Stute, B. Casabone, P. Schindler, T. Monz, P. O. Schmidt, B. Brandstätter, T. E. Northup, and R. Blatt. "Tunable ion-photon entanglement in an optical cavity". In: *Nature* 485.7399 (May 2012), pp. 482–485. DOI: `10.1038/nature11120` (cit. on pp. 59, 73).

[Tak14] H. Takahashi, J. Morphew, F. Oručević, A. Noguchi, E. Kassa, and M. Keller. "Novel laser machining of optical fibers for long cavities with low birefringence". In: *Opt. Express* 22.25 (Dec. 2014), pp. 31317–31328. DOI: `10.1364/OE.22.031317` (cit. on p. 135).

[Tak18] H. Takahashi, E. Kassa, C. Christoforou, and M. Keller. “Strong coupling of a single ion to an optical cavity”. In: (Aug. 13, 2018) (cit. on p. 133).

[Ter15] B. M. Terhal. “Quantum error correction for quantum memories”. In: *Rev. Mod. Phys.* 87.2 (Apr. 2015), pp. 307–346. DOI: `10.1103/revmodphys.87.307` (cit. on pp. 11, 14, 15).

[Val15] G. Vallone, D. Bacco, D. Dequal, S. Gaiarin, V. Luceri, G. Bianco, and P. Villoresi. “Experimental Satellite Quantum Communications”. In: *Phys. Rev. Lett.* 115 (4 July 2015), p. 040502. DOI: `10.1103/PhysRevLett.115.040502` (cit. on p. 11).

[Vit01] N. V. Vitanov, T. Halfmann, B. W. Shore, and K. Bergmann. “Laser-induced population transfer by adiabatic passage techniques”. In: *Annual review of physical chemistry* 52.1 (2001), pp. 763–809. DOI: `10.1146/annurev.physchem.52.1.763` (cit. on p. 34).

[Wal12] A. Walther, F. Ziesel, T. Ruster, S. T. Dawkins, K. Ott, M. Hettrich, K. Singer, F. Schmidt-Kaler, and U. Poschinger. “Controlling Fast Transport of Cold Trapped Ions”. In: *Phys. Rev. Lett.* 109 (8 Aug. 2012), p. 080501. DOI: `10.1103/PhysRevLett.109.080501` (cit. on pp. 28, 36, 85).

[Wes07] J. H. Wesenberg, R. J. Epstein, D. Leibfried, R. B. Blakestad, J. Britton, J. P. Home, W. M. Itano, J. D. Jost, E. Knill, C. Langer, R. Ozeri, S. Seidelin, and D. J. Wineland. “Fluorescence during Doppler cooling of a single trapped atom”. In: *Physical Review A* 76.5 (Nov. 2007). DOI: `10.1103/physreva.76.053416` (cit. on pp. 122, 124).

[Win78] D. J. Wineland, R. E. Drullinger, and F. L. Walls. “Radiation-Pressure Cooling of Bound Resonant Absorbers”. In: *Physical Review Letters* 40.25 (June 1978), pp. 1639–1642. DOI: `10.1103/physrevlett.40.1639` (cit. on p. 32).

[Wol19] S. Wolf. “Ion Crystals for Fundamental Research on Matter-Antimatter Symmetry and on Photon Statistics”. PhD thesis. Johannes Gutenberg Universität Mainz, 2019 (cit. on p. 109).

[Woo82] W. K. Wooters and W. H. Zurek. “A single quantum cannot be cloned”. In: *Nature* 229 (Oct. 1982), pp. 802–803 (cit. on p. 10).

[Yin16] H.-L. Yin, T.-Y. Chen, Z.-W. Yu, H. Liu, L.-X. You, Y.-H. Zhou, S.-J. Chen, Y. Mao, M.-Q. Huang, W.-J. Zhang, H. Chen, M. J. Li, D. Nolan, F. Zhou, X. Jiang, Z. Wang, Q. Zhang, X.-B. Wang, and J.-W. Pan. "Measurement-Device-Independent Quantum Key Distribution Over a 404 km Optical Fiber". In: *Physical Review Letters* 117.19 (Nov. 2016). DOI: `10.1103/physrevlett.117.190501` (cit. on p. 10).

[Zas12] S. Zaske, A. Lenhard, C. A. Keßler, J. Kettler, C. Hepp, C. Arend, R. Albrecht, W.-M. Schulz, M. Jetter, P. Michler, and C. Becher. "Visible-to-Telecom Quantum Frequency Conversion of Light from a Single Quantum Emitter". In: *Phys. Rev. Lett.* 109 (14 Oct. 2012), p. 147404. DOI: `10.1103/PhysRevLett.109.147404` (cit. on p. 15).

[Zie12] F. Ziesel. "Quantum State Manipulation and Dynamics in Micro Ion Traps". PhD thesis. Universität Ulm, 2012 (cit. on p. 94).

[Zip08] S. Zippilli, G. A. Olivares-Rentería, G. Morigi, C. Schuck, F. Rohde, and J. Eschner. "Entanglement of distant atoms by projective measurement: the role of detection efficiency". In: *New Journal of Physics* 10.10 (2008), p. 103003. DOI: `10.1088/1367-2630/10/10/103003` (cit. on pp. 59, 75).

[Zwe14] M. Zwerger, H. J. Briegel, and W. Dür. "Hybrid architecture for encoded measurement-based quantum computation". In: *Scientific Reports* 4.1 (June 2014). DOI: `10.1038/srep05364` (cit. on p. 14).

List of Publications

Referred to in this Thesis

- *A Quantum Repeater Node with Trapped Ions: A Realistic Case Example*,
  Appl. Phys. B 122:89 (2016)
  A. Pfister, M. Salz, M. Hettrich, U. G. Poschinger, F. Schmidt-Kaler
- *Experimental realization of fast ion separation in segmented Paul traps*,
  Phys. Rev. A 90, 033410 (2014)
  T. Ruster, C. Warschburger, H. Kaufmann, C. T. Schmiegelow, A. Walther, M. Hettrich, A. Pfister, V. Kaushal, F. Schmidt-Kaler, U. G. Poschinger

Previous Work

- *Dynamical mean-field theory versus second-order perturbation theory for the trapped two-dimensional Hubbard antiferromagnet*,
  Phys. Rev. B 84, 155129 (2011)
  A. Pfister, E. Jakobi, T. Gottwald, P. van Dongen

Acknowledgements

A work such as this would be impossible if not for a whole host of people sharing, in some way or another, in the work. My thanks go out to my colleagues, over the years, in the quantum information group, with whom it was a joy to work, to the staff of the group and of the entire Institute for their technical as well as administrative help, and to the collaborators from other scientific groups, both from the Institute of Physics of the University as well as from the Max Planck Institute for Polymer Science next door.

Finally, support and help from friends and family cannot be overrated - thanks to you all!